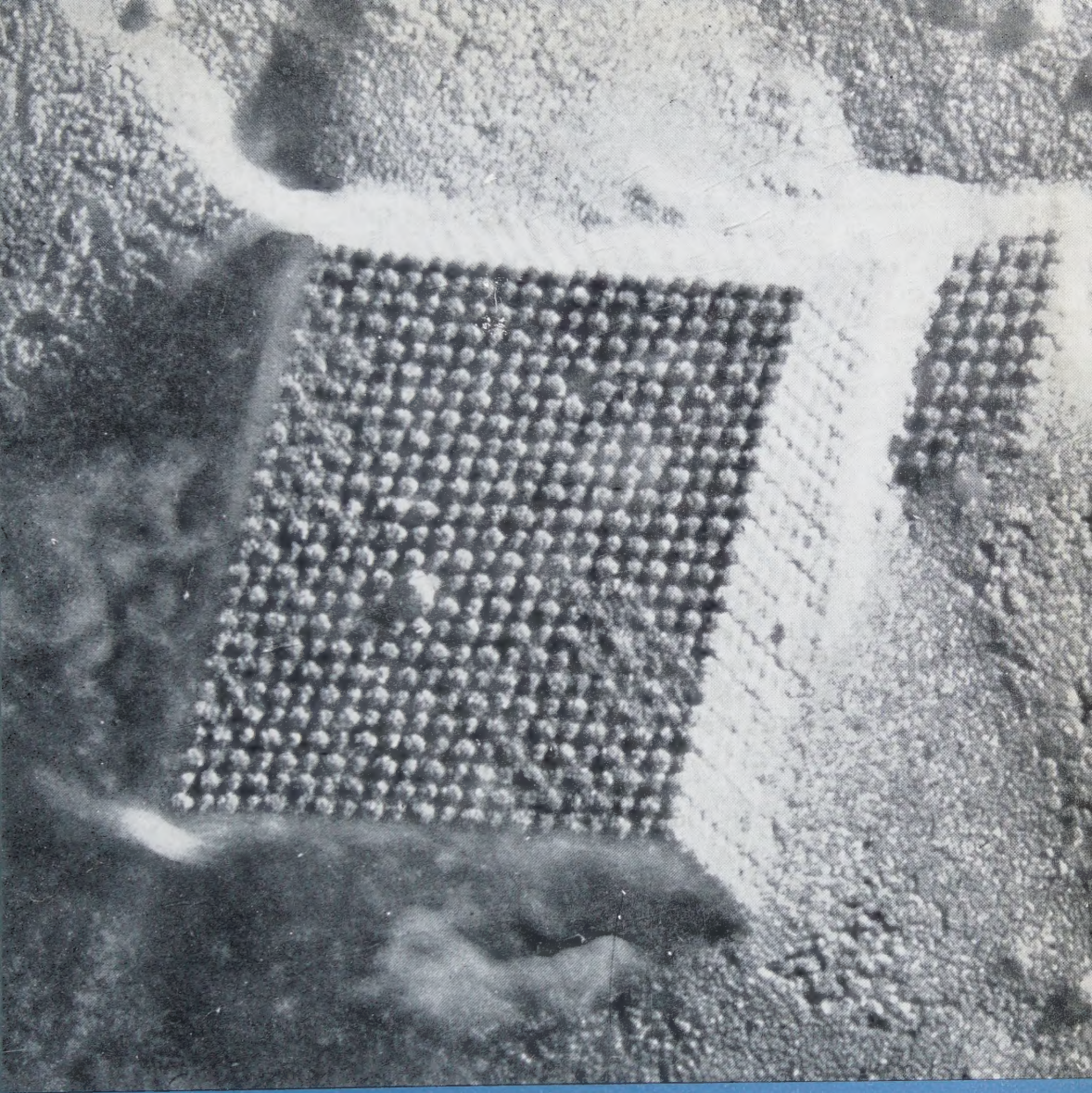

Journal of Ultrastructure Research

Volume 2, Number 2

December 1958

Academic Press Inc., Publishers, New York and London

JOURNAL OF ULTRASTRUCTURE RESEARCH

PUBLISHED BY

Academic Press Inc., 111 Fifth Avenue, New York 3, N.Y., U.S.A.

Volume 1, 4 issues, $15.00

Subscription orders should be sent to the office of the publishers

---

Front cover: Electron micrograph showing a crystal of the rhombic type of tobacco necrosis virus. LABAW, L. W. and WYCKOFF, R. W. G., *J. Ultrastructure Research 2*, 2 (1958).

The Fine Structure of Schwann Cells, Nodes of Ranvier and Schmidt-Lanterman Incisures in the Central Nervous System of the Crab, *Cancer irroratus*

J. H. McAlear[1], N. S. Milburn[2] and G. B. Chapman

The Biological Laboratories, Harvard University, Cambridge, Massachusetts

Received July 29, 1958

Electron microscopy of ultrathin sections of crab brain reveals the location of the Schwann cell nucleus outside of the myelin of the nerve fibers, as it is in vertebrate nerves. Comparison of the fine structure of the crustacean and vertebrate nodes of Ranvier reveals an essential similarity. Schmidt-Lanterman incisures, comparable to those of vertebrates, also occur in crustacea.

These observations are interpreted as indicating that the myelinated nerves of *Cancer irroratus*, a crustacean, are quite similar in structure to those of vertebrates.

The evolutionary implications of these observations are discussed.

Arthropod nervous systems have long been favored subjects for neurophysiological research. The structure of the crustacean nervous system, for example, is relatively simple and the animals tolerate experimental conditions well. In spite of the great activity in this field, the details of the anatomy of arthropod nervous systems are little known, as has been pointed out by Richards (*17*) and Welsh and Schallek (*22*). It is felt that the following study of the myelinated fibers in the central nervous system of the crab, *Cancer irroratus*, supplies some of the lacking information.

MATERIAL AND METHODS

Brains of *Cancer irroratus* were rapidly dissected out at room temperature and cut in half to facilitate penetration of Dalton's (*2*) chrome-osmium fixative, which was used at pH 7.5. Following fixation at 18°C for 2 hours, the washed, ethanol-dehydrated and methacrylate-embedded tissue (70°C for 24 hrs) was sectioned with the experimental model, thermal expansion ultramicrotome described by Hillier and Chapman (*8*). The sections were picked

[1] Present address: New York State Public Health Research Laboratories, Albany, New York.
[2] Present address: Department of Biology, Tufts University, Medford, Massachusetts.

up on collodion-covered copper grids and examined with an RCA EMU–2D electron microscope, which had been equipped with an 0.015 inch platinum, externally centerable (Canalco) condenser aperture and a 50 μ copper aperture in the standard objective pole piece.

RESULTS AND DISCUSSION

The work of Bear and Schmitt (*1*), using polarized light, did much to clarify the nature of the types of crustacean myelin. It was concluded that many crustacean axons were myelinated in the same manner as vertebrate nerves. However, the leg nerve of the lobster examined in the electron microscope (*6*, *20*), although possessing a heavy, loose, lamellar and fibrous sheath, was not truly myelinated. It is clear from Fig. 1 that *Cancer irroratus* does have nerves with a myelin structure, apparently similar to the myelin of vertebrates. This observation is confirmed by that of Knowles (*10*) (in the prawn *Leander serratus*).

Osmiophilia and the presence of nodes of Ranvier had been the major criteria for the identification of myelinated nerves, although with the light microscope very small or thinly myelinated nerves are difficult to identify. Unmyelinated fibers in the crab are commonly covered by sheath cell cytoplasm, the membranes of which may form up to ten lamellae, although the looseness and manner of formation distinguish this clearly from true myelin (*14*). It seems reasonable, therefore, that the identification of crustacean myelin has occasionally been questioned in the past (*23*).

Many of the light microscopists described crustacean myelinated nerves in remarkable detail (*4*, *9*, *15*, *16*). On comparing their pictures and diagrams it seems probable that, in most cases, what they called myelin was correctly named. Retzius (*16*), in particular, shows a detailed diagram of a node, including the spiny bracelet of Nageotte, which corresponds very closely to Fig. 2 of this text.

Early workers had also described the Schwann cell nucleus as being located inside of the myelin sheath instead of outside as it was known to be in vertebrate nerves (*21*). Holmes (*9*) pointed out this difference as well as others between arthropods and vertebrates, although he also recognized many similarities. In Fig. 1 the nucleus of the Schwann cell is seen outside of the myelin. This observation is supported by those of Knowles (*10*) in *Leander*. It seems clear, therefore, that the location of

---

FIG. 1. The nucleus is seen outside of the myelin (*M*) of the axon. Longitudinally disposed neurofilaments are seen in the axon. A mitochondrion (*MIT.*) is located near the axolemma which is pulled away from the myelin at the site indicated by the arrow. × 12,500.

FIG. 2. A longitudinal section through a node of Ranvier. Note the fibrosity at the node, the two rodlets and the mitochondrion on the right, the Schwann cell cytoplasm outside of the myelin and the spiny bracelet of Nageotte or insertions of the myelin terminae on the axolemma. × 16,000.

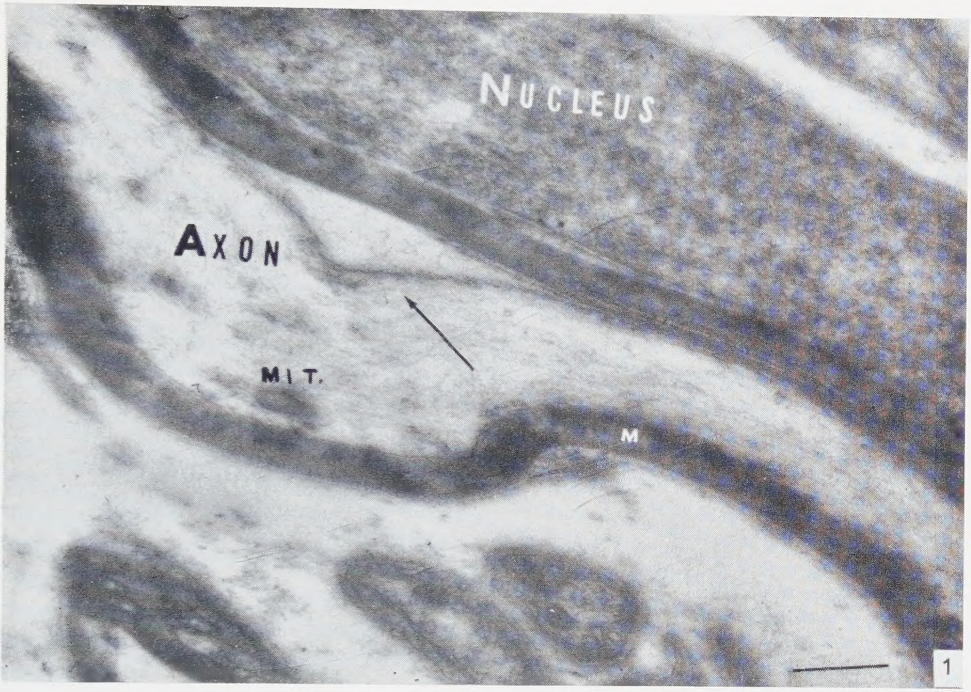
NUCLEUS
AXON
MIT.
M
1

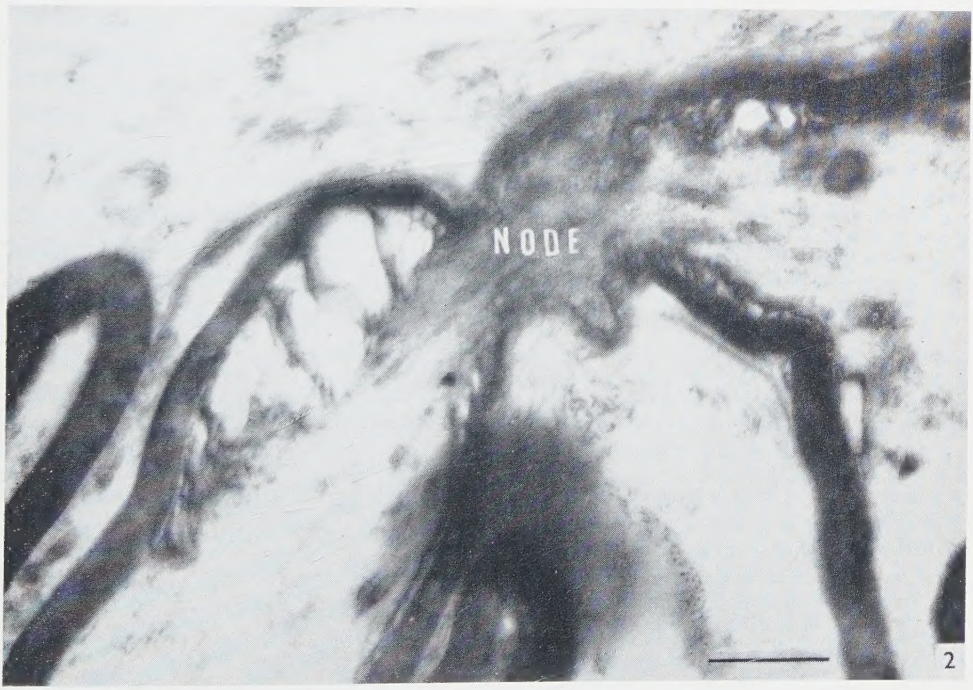
NODE
2

the nucleus inside of the myelin is not a consistent feature of arthropod myelinated axons.

Friedländer (*4*), Retzius (*16*), Nageotte (*15*) and Holmes (*9*) also described nodes of Ranvier in crustacean nerves. At the level of resolution of light optics, however, it is impossible to detect the fine detail necessary to compare these nodes intimately with those of the vertebrates. In Figs. 2 and 3 it is seen that the nodes are quite similar to those described in vertebrates (*5*, *7*, *12*, *13*) in general construction, but with some variations in detail.

The spiny bracelet of Nageotte, including the terminae of the double lamellae on the axolemma is very similar. The rod-like bodies described by Luxoro (*12*) may also be represented in Figs. 2 and 3. The fibrosity of the crustacean nodes resembles that of vertebrate nodes. The terminations of adjacent Schwann cells are not seen in Fig. 3. The cytoplasm of the Schwann cell does seem to cover the node thinly, however. The profiles in Fig. 3, which we believe represent tubules, are of considerable interest. Whether these represent holes in the Schwann cell, or projections of the axolemma through the Schwann cell could not be determined. The node seems a bit short compared to vertebrate nodes which the authors have seen.

The configurations known as incisures, which were originally described in vertebrates by Schmidt (*19*) and Lanterman (*11*), have recently been restudied with the electron microscope by Robertson (*18*). Their presence in *Cancer* (Fig. 4) further strengthens the impression of a similarity in nerve structure between vertebrates and this invertebrate. These structures in vertebrates are shown by Robertson (*18*) to be separations of the elements of a membrane pair. The resolution of the micrograph shown here is insufficient to confirm this, although, from a grosser aspect, a similar over-all impression is made.

It is interesting to compare these electron micrographs of crab nerve with some recent pictures of insect peripheral nerve (*3*). The myelin of the crab appears in compact lamellae while the insect peripheral nerve is "tunicated" by a loose spiral of meandering mesaxon. Considering that degrees of myelination are to be found within the nervous structures of a single animal, one could regard this tunicated nerve as being a precursor of the myelinated nerve. However, this question, as well as that of homologous versus parallel evolutionary development of the myelinated nerve in arthropods and vertebrates, must remain open until really extensive surveys of the nervous systems of invertebrates have been made.

FIG. 3. Note the tubules in the Schwann cell cytoplasm at the node (*T* arrow), the rodlet (*R*) and the insertions of the myelin lamellae (arrow). × 23,500.

FIG. 4. A Schmidt-Lanterman incisure in a myelinated axon (*A*). Note the region indicated by the arrow. × 21,500.

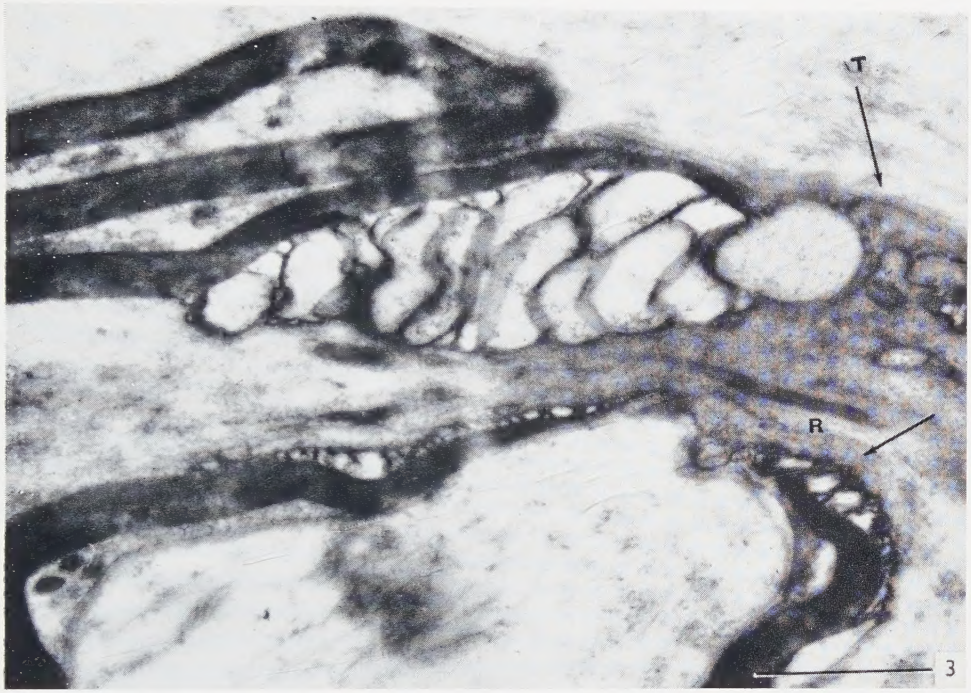
T
R
3

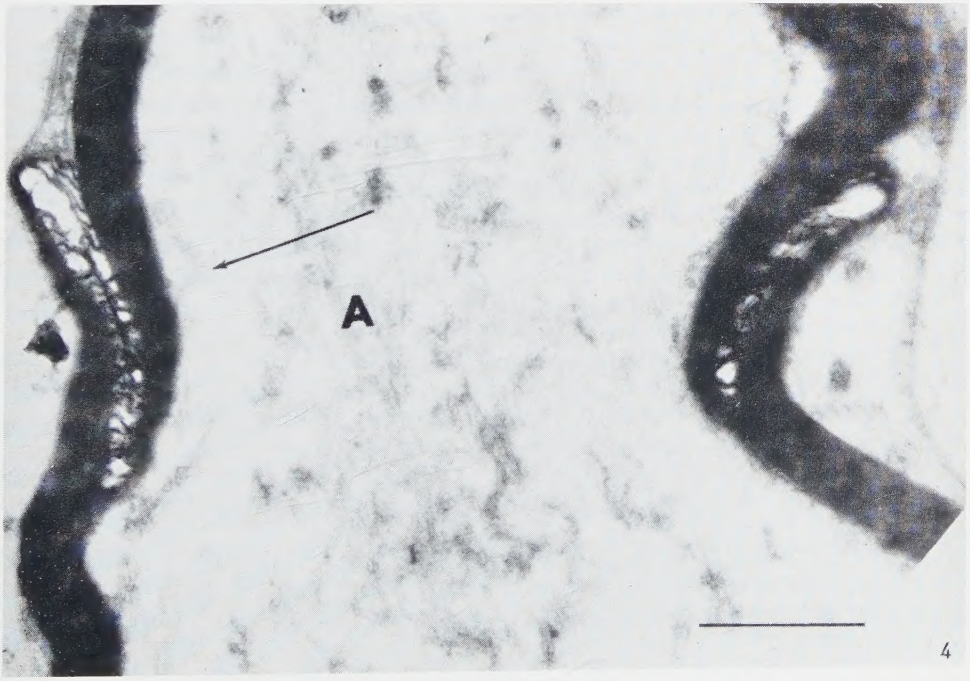
A
4

Some important differences do exist between crustacean and vertebrate nerves, as Holmes (*9*) points out. The internodal distance is variable and not related to the diameter of the axon, as it is in vertebrate nerves. Furthermore, some of the structures which do not resemble nodes, which were described by Retzius (*16*) in the myelinated fibers of the crayfish, have no known vertebrate counterpart. The node which is shown in this paper, however, does correspond very closely to the diagram of the node in the crayfish which Retzius described in remarkable detail with light optics.

It is concluded that the structure of myelinated nerves in the crustacean studied here and in vertebrates is much more similar than a survey of the literature would lead one to expect.

ACKNOWLEDGEMENTS

We gratefully acknowledge the criticisms of Professor J. H. Welsh of Harvard University and Professor F. O. Schmitt of the Massachusetts Institute of Technology concerning the essentials of this paper.

REFERENCES

1. Bear, R. S. and Schmitt, F. O., *J. Cellular Comp. Physiol.* **9**, 275 (1937).
2. Dalton, A. J., *Anat. Record* **121**, 281 (1955).
3. Edwards, G. A., Ruska, H. and Harven, E. J. de, *J. Biophys. Biochem. Cytol.* **4**, 107 (1958).
4. Friedländer, B., *Mitt. Zool. Sta. Neapel* **9**, 205 (1889).
5. Gasser, H. S., *Cold Spring Harbor Symposia Quant. Biol.* **17**, 27 (1952).
6. Geren, B. B. and Schmitt, F. O., *Proc. Natl. Acad. Sci. U.S.* **40**, 863 (1954).
7. Goldstein, A. and Chapman, G. B., unpublished observations.
8. Hillier, J. and Chapman, G. B., *Anal. Chem.* **26**, 437 (1954).
9. Holmes, W., *Phil. Trans. Roy. Soc. London Ser. B* **231**, 293 (1942).
10. Knowles, Sir Francis G. W., personal communication.
11. Lanterman, A. J., *Arch. mikroskop. Anat. u. Entwicklungsmech.* **13**, 1 (1877).
12. Luxoro, M., Ph.D. thesis. Mass. Inst. Technol., Cambridge, Mass., 1956.
13. Maturana, H. R. M., Ph.D. thesis. Harvard University, Cambridge, Mass., 1958.
14. McAlear, J. H. and Chapman, G. B., in preparation.
15. Nageotte, J., *Compt. rend. soc. biol.* **79**, 259 (1916).
16. Retzius, G., *Biol. Untersuch., Neue Folge* **1**, 1 (1890).
17. Richards, A. G., *in* Elliott, K. A. C., Page, I. H. and Quastel, T. H. (Eds.), Neurochemistry, Chapter XXXI. C. C. Thomas, Springfield, Ill., 1955.
18. Robertson, J. D., *J. Biophys. Biochem. Cytol.* **4**, 39 (1958).
19. Schmidt, H. D., *Monthly Microscop. J.* **11**, 200 (1874).
20. Schmitt, F. O., *in* Richter, D. (Ed.), Metabolism of Nervous System, p. 35. Pergamon Press, London, 1957.
21. Schmitt, F. O. and Bear, R. S., *Biol. Revs. Cambridge Phil. Soc.* **14**, 27 (1939).
22. Welsh, J. H. and Schallek, W., *Physiol. Revs.* **26**, 447 (1946).
23. Young, J. Z., *J. Physiol. London* **85**, 2P (1935).

An Electron Microscopic Determination of a Tobacco Necrosis Virus Crystal Structure

L. W. LABAW

National Institute of Arthritis and Metabolic Diseases,
National Institutes of Health, Public Health Service,
Department of Health, Education and Welfare, Bethesda 14, Maryland

Received August 8, 1958

The structure of the rhombic type of tobacco necrosis virus crystals has been found, from a study of electron micrographs depicting shadowed carbon replicas of the crystals, to be orthorhombic with the tetramolecular unit having $a_0 = 310$ Å, $b_0 = 384$ Å and $c_0 = 391$ Å. The diameter of the virus particle in these crystals was found to be 250 Å. In this structure the average volume occupied by a molecule is the largest possible in going from the cubic close-packed to the hexagonal close-packed arrangement of spherical molecules. These tobacco necrosis virus crystals have nearly the same crystal structure in the wet and dry state as evidenced by the same angles of the rhomboids on wet and dry crystals.

Electron micrographs depicting the molecular order on crystals of a tobacco necrosis virus protein published several years ago (*6*, *8*) and more recently (*3*, *5*) have shown the crystals to have less than cubic symmetry. The evidence for this is: (1) the dominant face of these crystals is rhombic in outline rather than rectangular, (2) the molecules on this principal face appear to be nonplanar, that is, alternate rows stand out above the others when viewed in the direction of either diagonal, and (3) the molecules on the side faces also appear to be nonplanar by having alternate rows stand out from the others. It is the subject of this paper to determine from the electron microscopic evidence the crystal structure of the tobacco necrosis virus, which crystallizes in these rhombic type crystals, instead of the cubic close-packed structure. This latter structure is characteristic of the southern bean mosaic virus protein (*4*), one of the other tobacco necrosis virus proteins (*5*) and one of the polio-viruses (*7*), all having particles nearly the same size.

The shadowed carbon replicas used for the analysis, some of which are shown together with crystal models in Figs. 1, 3 and 4, were of crystals grown from a purified virus preparation supplied for the earlier work (*6*) by Dr. Kenneth M. Smith, Director of the Virus Research Unit of the Agricultural Research Council in Cam-

bridge, England. Optical photographs of this type of rhombic tobacco necrosis virus crystal have been published by Bawden and Pirie (see *1*, Figs. 22 and 33).

Examination of over 700 electron micrographs of the rhombic type of tobacco necrosis virus crystals and careful measurements on many of these has revealed, in addition to the three observations mentioned in the opening paragraph, that (1) the raised rows of molecules along the two rhombic diagonals are always very nearly at right angles and (2) the average molecular separations along these two orthogonal directions are 384 ± 9 Å and 310 ± 9 Å. These raised rows of molecules are particularly well revealed on the crystal in the lower right of Fig. 3*a* because of the angle of shadowing with respect to the principal face. From the separations in the two orthogonal directions, the obtuse angle of the principal face, 2θ, may be calculated as $\tan \theta = 384/310 = 1.239$ or $\theta = 51°6'$ and $2\theta = 102°12'$. The acute angle of the principal face, therefore, is, on the average, $77°48'$.

Any further characterization of the crystal structure must make use of the other information revealed in the micrographs. This is the particular nonplanar nature of the principal and side faces. A careful examination of the many micrographs seemed to indicate that the crystal structure could be considered as one in which every other plane of molecules perpendicular to the longer of the rhombic diagonals of the principal face were at one level, in a direction perpendicular to the principal face, while the intervening layers were at a different level. The distribution of molecules in these planes could be inferred to be rhombic rather than square from the relative close-packing on the principal and side faces.

The crystal structure thus deduced is orthorhombic and is diagramed in Fig. 2. A model of this structure was built and photographed with different directions of illumination. These photographs have been placed on the micrographs in Figs. 1, 3 and 4 for comparison. The correctness of the proposed structure rests on the correspondence of the micrographs with the crystal model photographs. For the remainder of the paper it will be assumed that the crystal structure found by this somewhat unorthodox method is correct and the structure will be used to compute the unknown crystallographic constants.

The unit cell containing four molecules has $a_o = 310$ Å (corresponding to AB in Fig. 2), $b_o = 384$ Å (CD of Fig. 2), with c_o and the particle diameter, D, to be determined. Referring to Fig. 2, from the XZ projection, $a_o = 2D \cos \phi$ and $c_o = EF = 2D \sin \phi$. Using the pythagorean theorem in the YZ projection, $(b_o/2)^2 + (EO)^2 = D^2$. Now EO may be evaluated using similar triangles from the XZ projection as $EO = D/2 \sin \phi$, and hence $b_o = 2D/(1 - 1/4 \sin^2 \phi)$. The angle ϕ, the value of

FIG. 1. A crystal of the rhombic type of tobacco necrosis virus in which the principal (001) face and four (111) faces can be seen, together with an orthorhombic crystal model for comparison. × 168,000.

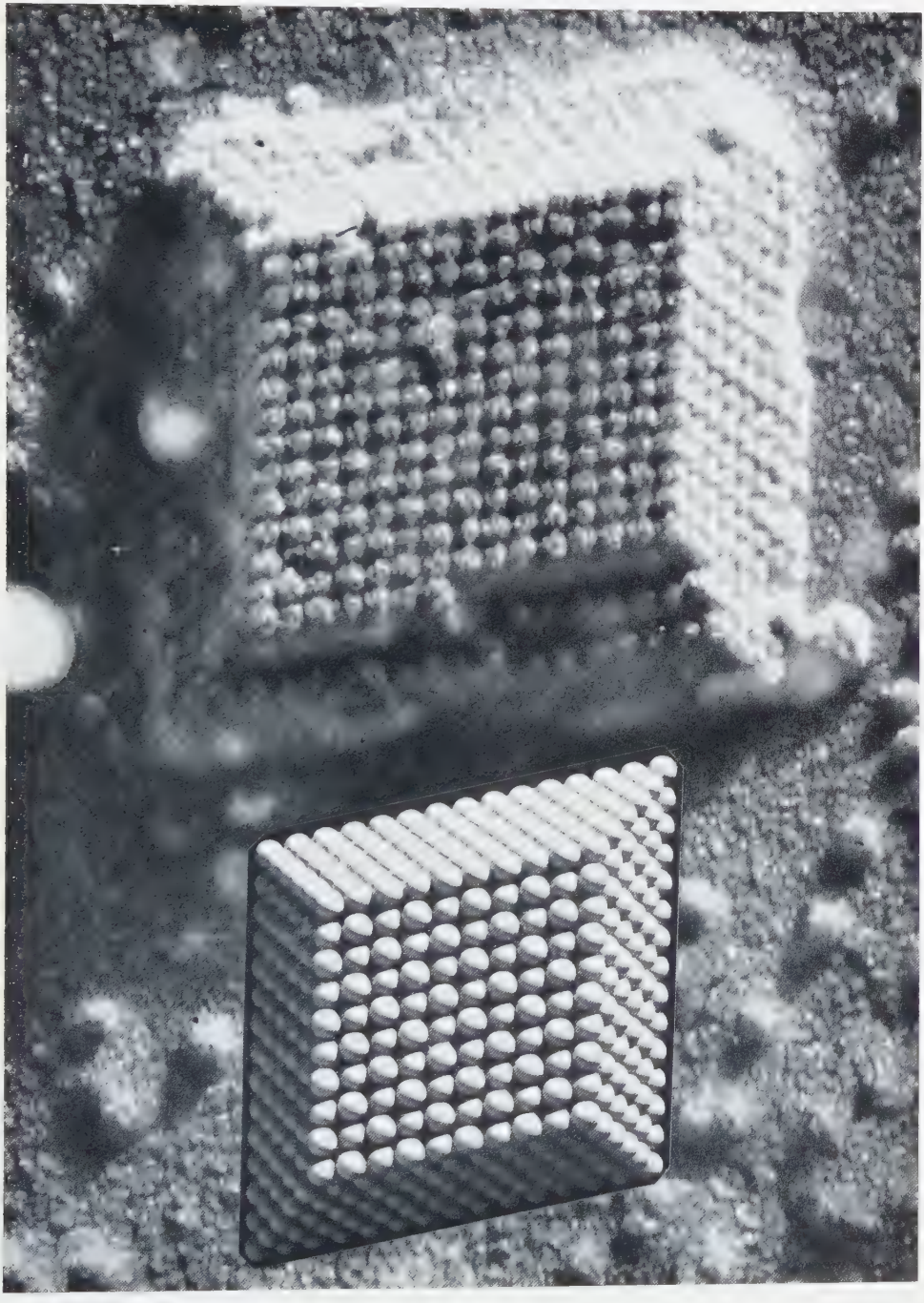

which is necessary to find c_o, may be computed from the relation $\tan \theta = b_o/a_o = 1/((1 - 1/4 \sin^2 \phi)/\cos \phi) = 1.239$. This can be solved easily by substituting values for ϕ in the left side of the equation and finding graphically what value of ϕ makes this equal to 1.239. This is $\phi = 51°36'$, and hence $c_o = 391$ Å and $D = a_o/2 \cos \phi = 250$ Å. It is interesting to note that the particle center separation in the XY plane projection is equal to 247 Å and hence very nearly equal to D, and that b_o and c_o are also nearly the same.

The similarity between the models and the micrographs in Figs. 1, 3 and 4 shows that the less than cubic symmetry of the crystals of this tobacco necrosis virus does not reflect a lack of sphericity of the molecules in the crystal. The crystals can be considered to be made up of spheres which have as close a packing as is possible with the angle ϕ in the XZ plane being 51 36′. It is instructive to examine the different types of crystal structures that are built up when spheres are close-packed for different possible values of the angle ϕ. The angle ϕ can vary only from 30 to 60 and still have the coplanar molecules in the XZ plane in contact. The structure as ϕ changes from 30 to 45 is equivalent to that as ϕ changes from 60 to 45 so only the variation of ϕ from 45 to 60 will be considered. When ϕ 45 , the structure is cubic close-packed (or face centered cubic) with the molecules in the (100), (010), and (001) planes coplanar and in contact. In general, when ϕ is greater than 45 , referring to Fig. 2, the particles whose center is at D can assume either of two positions. It can be in contact with the three particles whose centers are at A, E and B or in contact with the three spheres whose centers are at A, F and B. The projection of its center can, therefore, be either at O or at O'. If alternate planes of molecules perpendicular to the Y axis are built up so that the projections of their molecular centers on the planes immediately below them are at the generalized position O and the intermediate layers have the projections of their molecular centers on the planes below them at the generalized position O', the crystal axes remain orthogonal. In this case, the molecules in the (010) planes are coplanar and in contact, the ones in the (100) planes are coplanar and not all in contact (the YZ projection of Fig. 2), and the molecules in the (001) are in contact but not coplanar. In the particular case when ϕ is 60 , the structure is hexagonal close-packed with additional symmetry because the molecules whose centers are represented by A and B are in contact, which means, also, that the zigzag rows of molecules in contact in the YZ projection are far enough apart to permit the spheres in the adjacent planes to be tangent to this YZ plane. If when ϕ 45 all the planes of molecules perpendicular to the Y axis are built up so that the projections of their molecular centers are at the generalized position O with respect to the planes immediately below them, the structure is monoclinic, using these axes, rather than orthorhombic and the molecules in the (100), (010) and (001) planes are all coplanar.

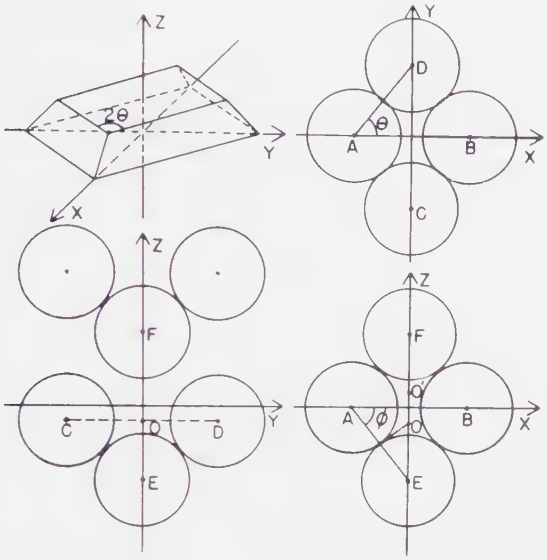

FIG. 2. A diagram of the orthorhombic crystal structure deduced from the micrographs of the virus crystals. This is the structure of the model used for comparison in Figs. 1, 3 and 4.

The question of why one tobacco necrosis virus crystallizes in an orthorhombic structure and another in a cubic close-packed structure affords interesting speculation. Since it is not apparently associated with any physical asymmetry of the molecules, it may be assumed to be caused by some chemical property of the virus particles. One approach that could give a little understanding of this is a consideration of the average volumes occupied per molecule in the crystals. A plot of the unit cell volume divided by the number of molecules in the unit cell, $(a_o \cdot b_o \cdot c_o)/4 = 2D^3 (\cos \phi)(\sin \phi)\sqrt{(1 - 1/4 \sin^2 \phi)}$, against ϕ, for $45° \leq \phi \leq 60°$, shows the expected same and minimum value of $\frac{1}{2}\sqrt{2}D^3$ or 0.7071 D^3 for ϕ equal to 45° and 60°. The curve has a somewhat parabolic shape between these two angles with a broad maximum centering around ϕ 52.2 giving a maximum value of the average volume per molecule of 0.7500 D^3. The value of ϕ for the orthorhombic crystal structure of the virus was found to be 51.6 which results in an average volume per molecule of 0.7496 D^3. Thus, this orthorhombic crystal structure has the maximum volume possible for the close-packed arrangements considered here and one is tempted to believe that the crystal structure is caused by or is the result of some unknown property of the molecules of this type of tobacco necrosis virus which requires them to be as far apart as possible while still forming a self-supporting, compact crystal structure. This would explain why the

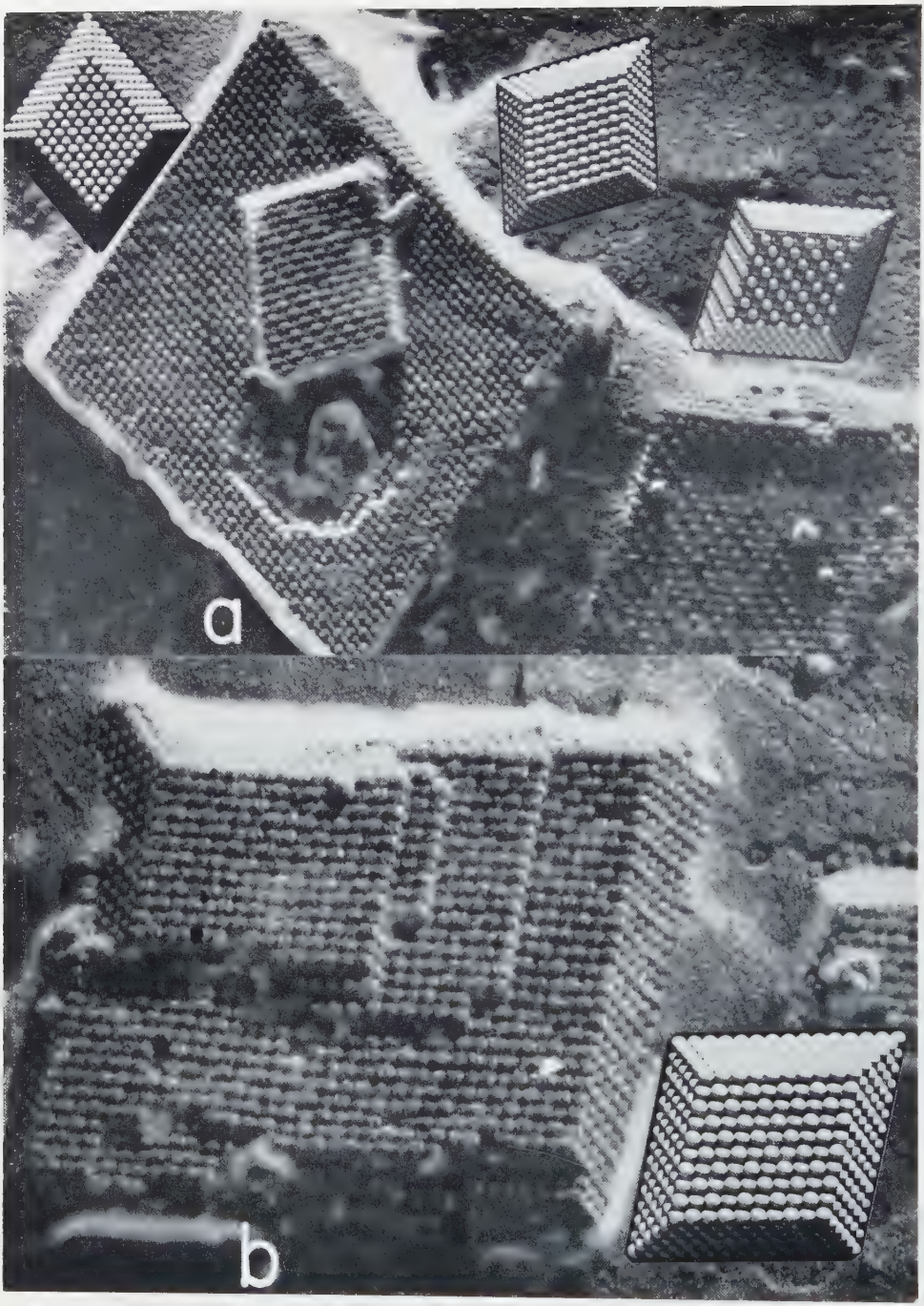

Fig. 3. *a*: Three differently oriented crystals with their corresponding models illustrating the changed appearance of the principal face for different shadowing directions relative to this face. × 59,700. *b*: A crystal so oriented that the direction of shadowing is nearly parallel to two opposite (111) faces, with the orthorhombic crystal model which is illuminated correspondingly. × 94,400.

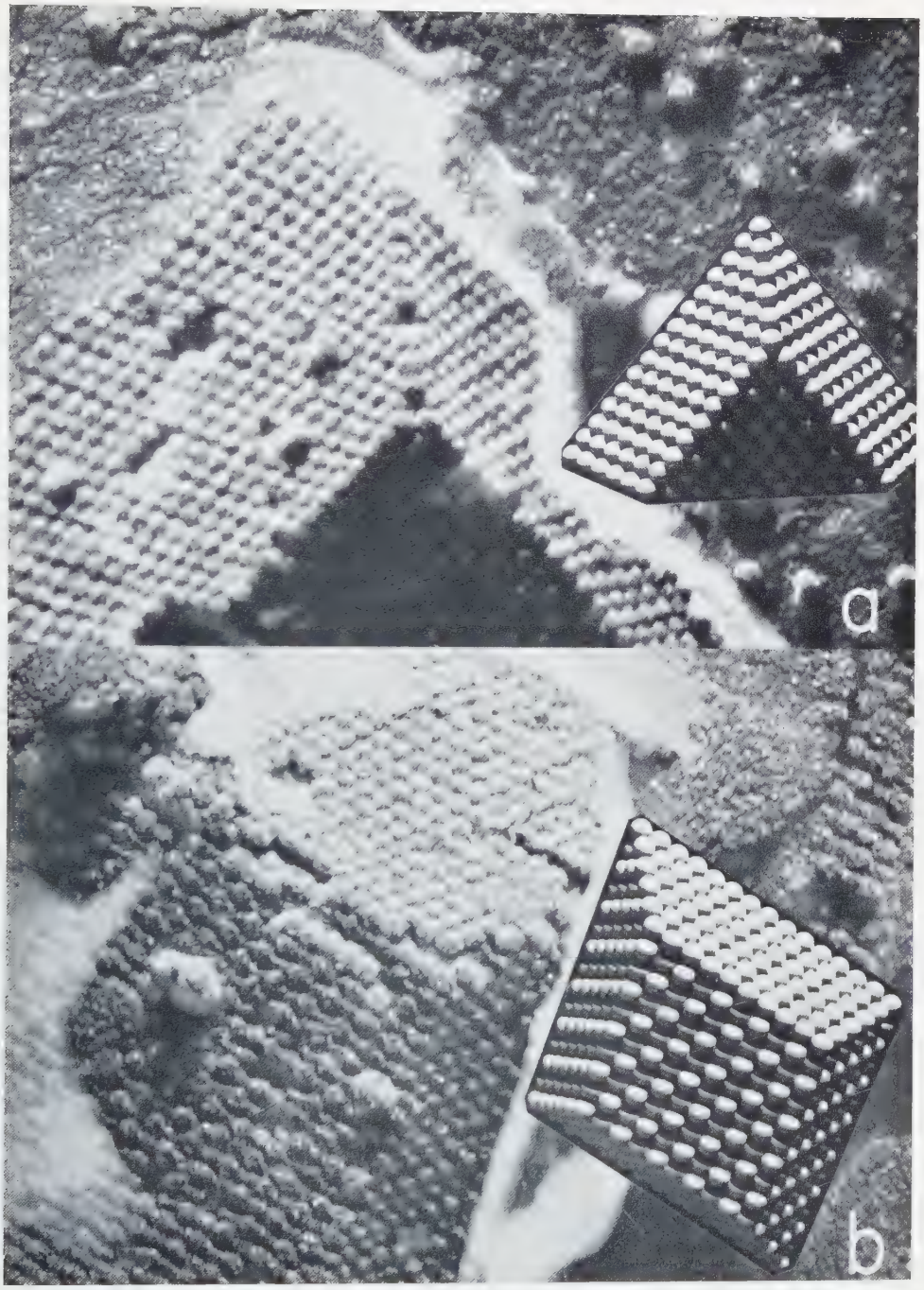

FIG. 4. *a*: Part of a virus crystal showing the junction of the two (111) faces at an acute angle of the principal face with the similarly photographed crystal model. *b*: The same at an obtuse angle of the principal face with the corresponding model. × 129,000.

angle ϕ determined experimentally is quite uniform ($\theta = 51.1 \pm 0.67°$) and does not vary from 45° to 60°. Why the structure is always orthorhombic and not monoclinic with the same maximum volume is more difficult to understand. (The body centered cubic structure of spheres, while self supporting, is not close-packed since it has an average volume per molecule of 0.7698 D^3.)

The question of the crystal form changing between the dry and wet state may be examined by comparing the angles of the rhomboids of the principal faces in the electron micrographs with those in optical photographs of the crystals in the wet state. The angles in photographs of crystals in the wet state taken from the same crystallization as used for the electron microscope preparations, as well as those in the published photomicrographs of Bawden and Pirie (see *1*, Figs. 22 and 33; *2*), give an average value of $\theta = 50.5°$ compared with the average from the electron micrographs of $\theta = 51.1°$. Apparently there is little if any change in the crystal form, though the unit cell found here is for the dry state and indeed is probably a little smaller than the actual dry state unit cell, since the replicas of the crystal surfaces on which the measurements were made were not always normal to the electron beam.

The author is pleased to acknowledge his indebtedness to Dr. Ralph W. G. Wyckoff in whose laboratory this work was undertaken.

REFERENCES

1. Bawden, F. C., Plant Viruses and Virus Diseases. Chronica Botanica Company, 1950.
2. Bawden, F. C. and Pirie, N. W., *Brit. J. Exptl. Pathol.* **23**, 314 (1942).
3. Labaw, L. W. and Wyckoff, R. W. G., *Proc. Koninkl. Ned. Akad. Wetenschap Ser. B* **59**, 171 (1956).
4. —— *Arch. Biochem. Biophys.* **67**, 225 (1957).
5. —— *J. Ultrastructure Research* **2**, 8 (1958).
6. Markham, R., Smith, K. M. and Wyckoff, R. W. G., *Nature* **159**, 574 (1947).
7. Steere, R. I. and Schaffer, F. L., *Biochim. et Biophys. Acta* **28**, 241 (1958).
8. Wyckoff, R. W. G., *Acta Cryst.* **1**, 292 (1948).

Ultrastructure of Mouse Uterine Surface Epithelium under Different Estrogenic Influences

3. Late Effect of Estrogen Administered to Spayed Animals

O. NILSSON

Department of Histology and Laboratory for Biological Ultrastructure Research, Department of Anatomy, Karolinska Institutet, Stockholm

Received October 31, 1958

Spayed mice of the C3H strain were given a single intraperitoneal injection of 1 μg estradiol-17β in 0.05 ml propylene glycol. The appearances of the uterine epithelial cells were investigated 2, 4, and 6 days after the administration of hormone.

The vaginal smears were cornified 2 days after injection, but the folding of the lateral cell membranes, the intercellular vacuoles, the intramitochondrial bodies, and the vesicles, present in estrous mice, were not observed.

After the 2-day stage the epithelial cells gradually returned to the castrate condition. The cell height changed from about 16 μ to 9 μ. The microvilli decreased in number and length, and the lumenal substance, which was observed in animals 2 days after hormone injection, was not present at the later periods. The distances between the two dense layers of the lumenal cell surface and between the lateral, adjacent cell surfaces, which decreased during the day after estrogen administration, returned to the castrate level 2 days after injection. The mitochondria of the 4-day animals were longer than those of spayed animals, but 6 days after estrogen injection they were small and had a rounded or rod-shaped form. No differences in ultrastructure of the uterine epithelia from treated animals and spayed animals remained 6 days after estrogen injection.

The change in number of lipid granules was accompanied by the appearance of areas with granules, membranes, and spaces. Many cytoplasmic bodies of different shapes and sizes were observed in the neighbourhood of these areas.

The late effect of a single injection of estrogen into spayed animals is taken in this paper as beginning when the castrate type of vaginal smear turns into the cornified type. This occurred 2 days after the hormone injection in the strain of mice used in this series of experiments (*19*).

The uterus of ovariectomized mice and rats became thick and edematous and its surface epithelium higher after estrogen administration; when the administration

ceased, the uterus returned to its castrate condition (*1*, *4*, *6*, *14*, *24*). Cytological studies have shown the growth of the uterine epithelium to be associated with an increase in the ribonucleic acid (*9*, *13*) and alkaline phosphatase (*2*, *3*, *13*, *15*, *25*, *29*) contents of the cells. The estrogen also caused a decrease in the number of lipid granules of the epithelial membrane (*5*, *16*).

The present paper is concerned with the ultrastructural changes that are associated with the late effect of an injection of estrogen. The paper demonstrates the appearances of the uterine epithelium from spayed animals 2, 4, and 6 days after the single injection of estradiol.

MATERIAL AND METHODS

Three groups of animals, each comprising 5 three-month old, spayed mice of the C3H strain were used. The animals were given an intraperitoneal injection of 1 μg estradiol-17β in 0.05 ml propylene glycol two weeks after the ovariectomy. The animals of each group were then sacrified for fixation of the uterus 2, 4, and 6 days respectively after the injections. The fixative was a buffered, 1% osmium tetroxide solution (*22*, *26*), and the preparations were embedded in butyl methacrylate (*17*). The details of this procedure were reported earlier (*18*). The sections were cut on an ultramicrotome designed by Sjöstrand (*28*) and examined in an RCA EMU–2C electron microscope.

RESULTS

2 days after estrogen administration

The epithelial cells were 14–17 μ in height and 3–5 μ in width; the oval nuclei lay basally in the cells.

The lumenal cell membrane bulged slightly into the lumen and showed many microvilli with a maximum length of about 0.4 μ. At the cell surface, a lumenal substance of thin, dense strands was noticed (Figs. 1 and 2). The lumenal membrane was triple-layered with a distance of about 80 Å between the central parts of the two dense layers (Fig. 2). The lateral, adjacent cell surfaces ran parallel at a distance of about 220 Å. They were occasionally folded.

The mitochondria had, in the sections, a rounded or elongated form, and they contained dark granules (Fig. 4).

The system of α-cytomembranes was observed in the cells as small, membrane-bounded spaces of varying shapes and sizes.

FIG. 1. Survey picture of uterine epithelium 2 days after injection of estrogen. The lumenal surfaces are slightly bulging into the lumen, the microvilli are rather numerous, and the lumenal substance is visible. Small vacuoles are shown in the apical part of the cytoplasm. Some lipid granules are seen as dark granules with an irregular outline. × 21,000.

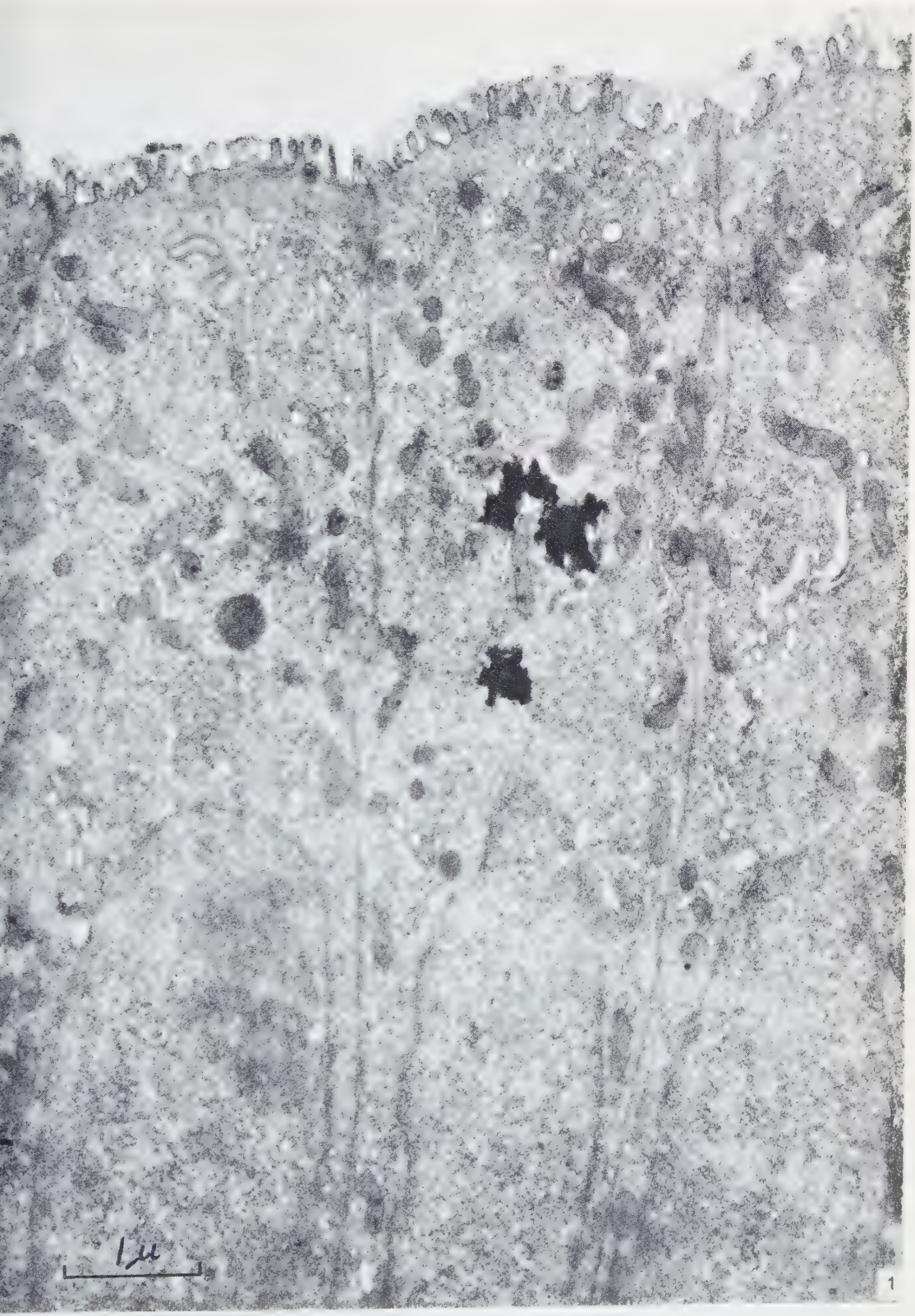
1μ
1

The Golgi apparatus was composed of γ-cytomembranes, Golgi granules, and small vacuoles (Figs. 3 and 4). The Golgi granules were of a frequent occurrence in the zone.

Lipid granules were noticed in all parts of the cytoplasm as dark granules with an irregular outline (Figs. 1, 3 and 4). Dark granules with a smooth outline were also observed (Fig. 5). They were homogeneous and bounded by a thin, darker zone. The largest of these granules were about 1 μ. They were often connected to membrane systems. Dense granules with a smooth outline and a maximum size of about 1.5 μ were occasionally observed (Fig. 5). Some of these had a darker centre.

Areas, a few microns large, with a complex and varying composition of dark granules, membranes, and empty spaces were present (Figs. 3 and 5).

Cytoplasmic bodies with coarse granules, and bodies with irregularly distributed membranes were often observed (Figs. 3 and 4). Bodies with a size of up to 0.6 μ were seen.

Vesicles containing small, ring-shaped profiles were seen in the cytoplasm.

Small vacuoles, with a size of up to about 800 Å, were noticed in the apical part of most of the cells (Figs. 1 and 2). The vacuoles were bounded by a membrane.

4 days after estrogen administration

The epithelial cells were 10–12 μ in height and 4–5 μ in width; the oval nuclei lay basally in the cells (Fig. 6).

The lumenal cell membrane showed microvilli (Figs. 6, 7 and 9), the longest being about 0.3 μ. They were not so numerous in this epithelium as in the epithelium investigated 2 days after the hormone injection. Neither was any lumenal substance visible. The lumenal membrane was triple-layered with a distance of about 80 Å between the central parts of the two dense layers. The lateral, adjacent cell surfaces ran parallel at a distance of about 220 Å. Some were markedly folded in the basal part of the epithelium.

The mitochondria had a structure similar to that observed in the mitochondria of the previous group (Figs. 8 and 9). Some of the mitochondria profiles had a length of about 3.5 μ.

The Golgi apparatus was composed of γ-cytomembranes, Golgi granules, and small vacuoles (Figs. 7 and 9).

The other cytoplasmic constituents were in general like those observed in the cells of animals studied 2 days after estrogen administration.

6 days after estrogen administration

The structure of these uterine epithelial cells was similar to that of the cells from spayed animals (*18*).

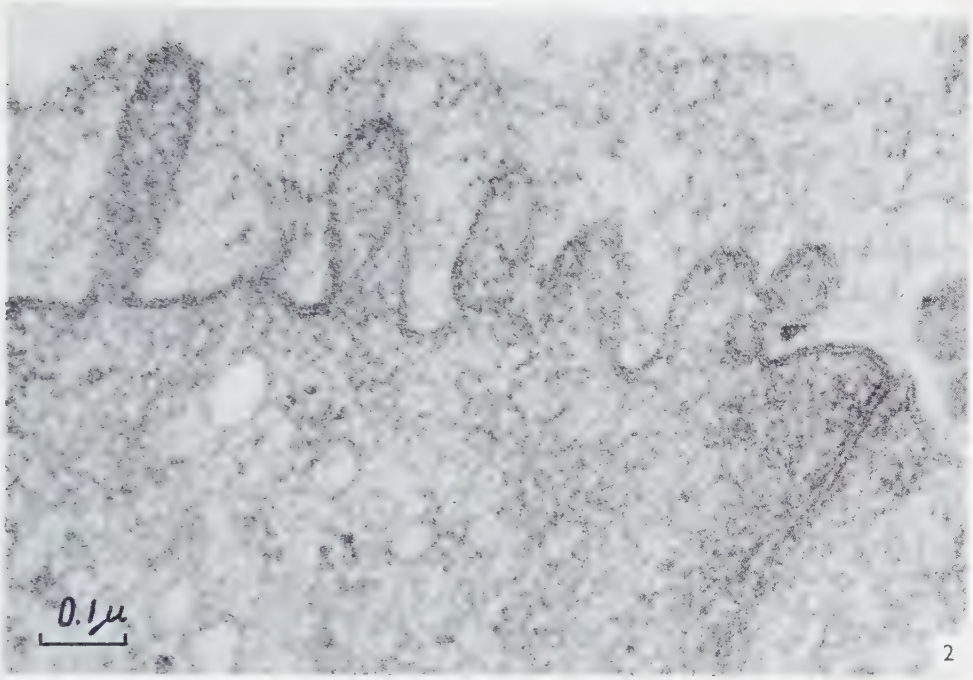

FIG. 2. Lumenal part of uterine epithelium 2 days after injection of estrogen. The triple-layering of the cell membrane is discernible. The lumenal substance is seen, and in the cytoplasm, some vacuoles are shown. × 108,000.

DISCUSSION

Four hours and 20 hours after the injection of estrogen into spayed animals, changes were noted in the cell membranes of the uterine epithelium. There was a diminution in the distances between the two dense layers of the lumenal cell surface and between the lateral, adjacent cell surfaces from 70 Å to 40 Å and from 260 Å to 160 Å respectively (*19*). Two days after the injection of hormone, however, these distances were nearly the same as those observed in spayed animals. This might imply that after 2 days the estrogen no longer exerted the same influence as earlier on the cell membrane.

Two days after the injection of estrogen into spayed animals, the vaginal reaction was similar to that appearing during estrus of normal animals. But the ultrastructure of the uterine epithelium from injected mice did not quite attain the appearance of that of estrous mice (*18*). The similarities in ultrastructure between cells of these two groups of animals consisted in the occurrence of, *inter alia*, rather long microvilli,

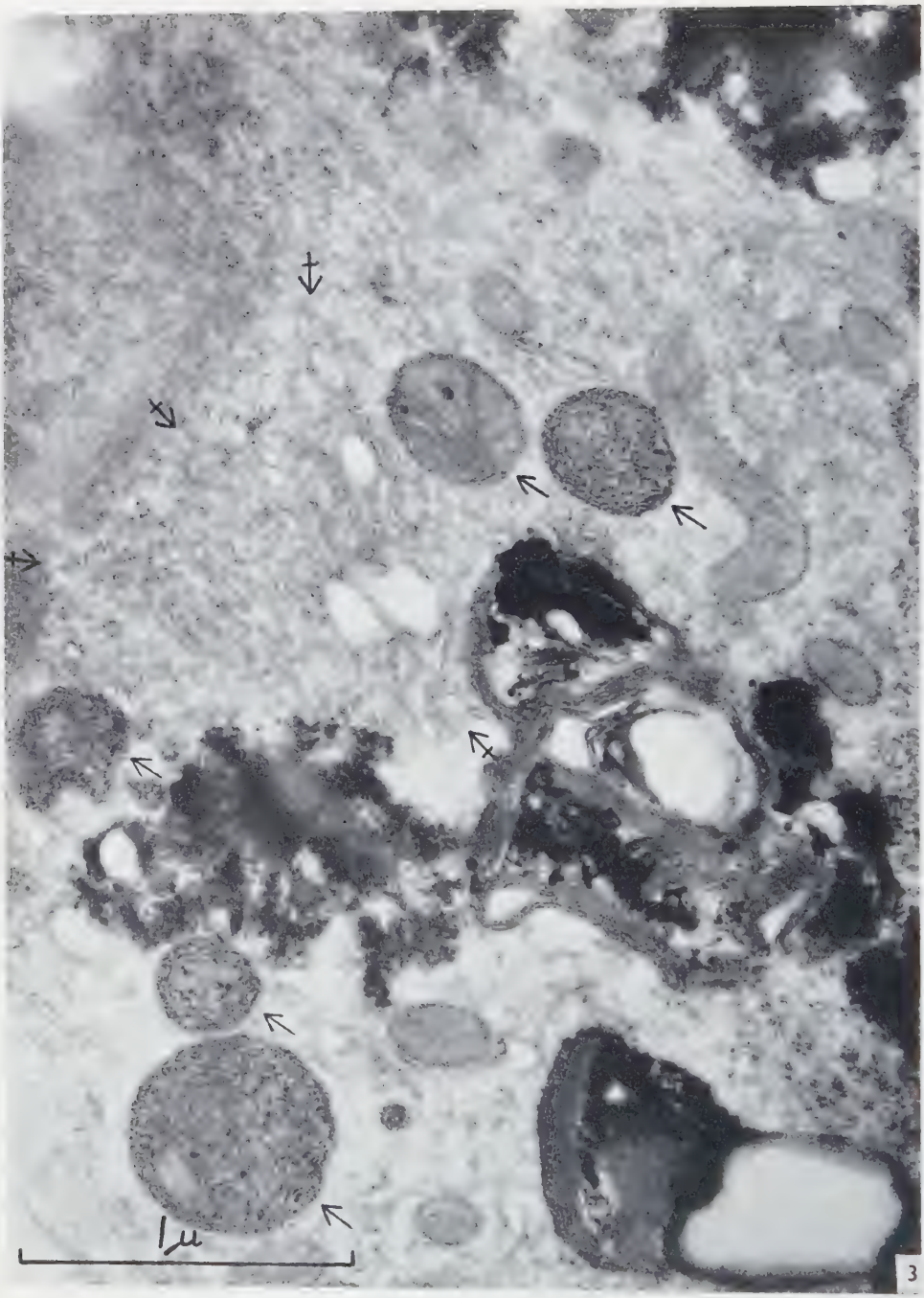

FIG. 3. Part of uterine epithelial cell 2 days after injection of estrogen. Some areas with granules, membranes, and spaces are shown to the right; lipid granules are visible to the left and in the upper, right-hand corner. Mitochondria, a Golgi apparatus (↔) with several Golgi granules, and cytoplasmic bodies (→) of different sizes and structures are also seen. ×46,000.

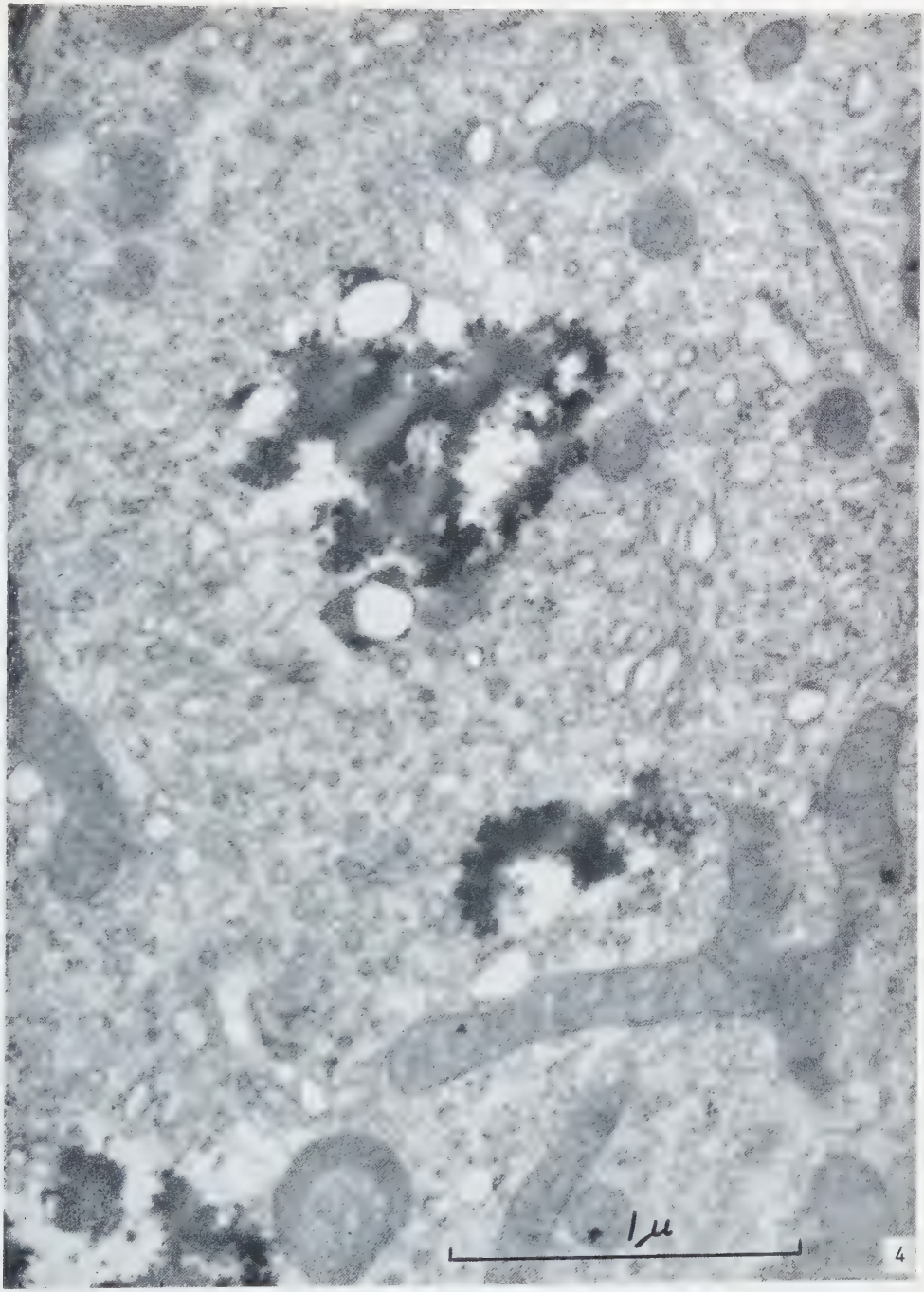

FIG. 4. Part of uterine epithelium 2 days after injection of estrogen. An area with lipid granules and small, membrane-bounded spaces is seen in the upper half of the figure. A Golgi apparatus with many Golgi granules partly encircles this area. The Golgi zone is surrounded by α-cytomembranes, small particles of the cytoplasm, and mitochondria. A cytoplasmic body is seen at the bottom. A cell border is visible in the upper, right-hand corner. × 48,000.

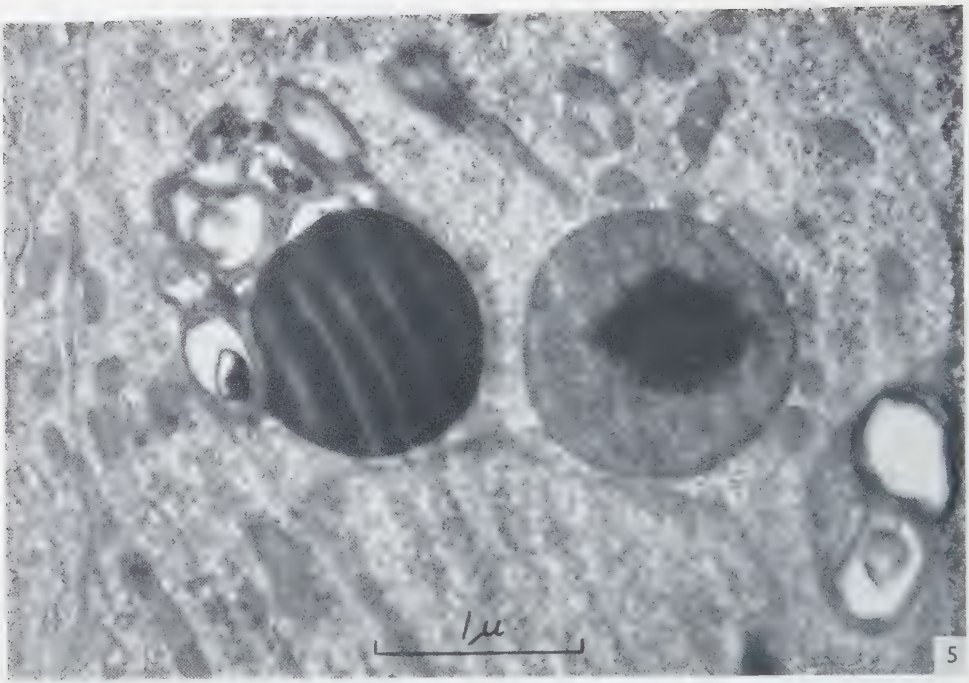

FIG. 5. Part of uterine epithelium 2 days after injection of estrogen. To the right and left, areas composed of granules, membranes, and empty spaces are seen. A dark granule with a smooth outline is connected to the left area. A dense granule with a dark central part is shown at the right-hand side. × 27,000.

a lumenal substance, many α-cytomembranes, and small, apical vacuoles. However, the pronounced folding of the lateral cell membranes, the intercellular vacuoles, the intramitochondrial bodies, and the vesicles, noticed in the epithelium of estrous mice, were not observed in the cells of injected animals. Thus, under the present experimental conditions estrogen is not capable of reproducing all the ultrastructural changes which occur in the mouse uterine epithelium during estrus.

Histochemical studies showed that the amount of ribonucleic acid (*9*, *13*) and alkaline phosphatase (*2*, *3*, *13*, *15*, *25*, *29*) in the epithelium was increased both after estrogen administration and during estrus. The ultrastructural studies demonstrated an increasing number of the small particles of the cytoplasm and of the α-cytomembranes both in 2-day animals and in estrous animals. As these cytoplasmic structures are assumed to contain RNA (*23*), the electron microscopical findings are in agreement with the histochemical observations on ribonucleic acid. The alkaline phosphatase was reported to be most active in the lumenal part of the epithelium. Both estrogen-treated and estrous animals showed an increase in the number and length

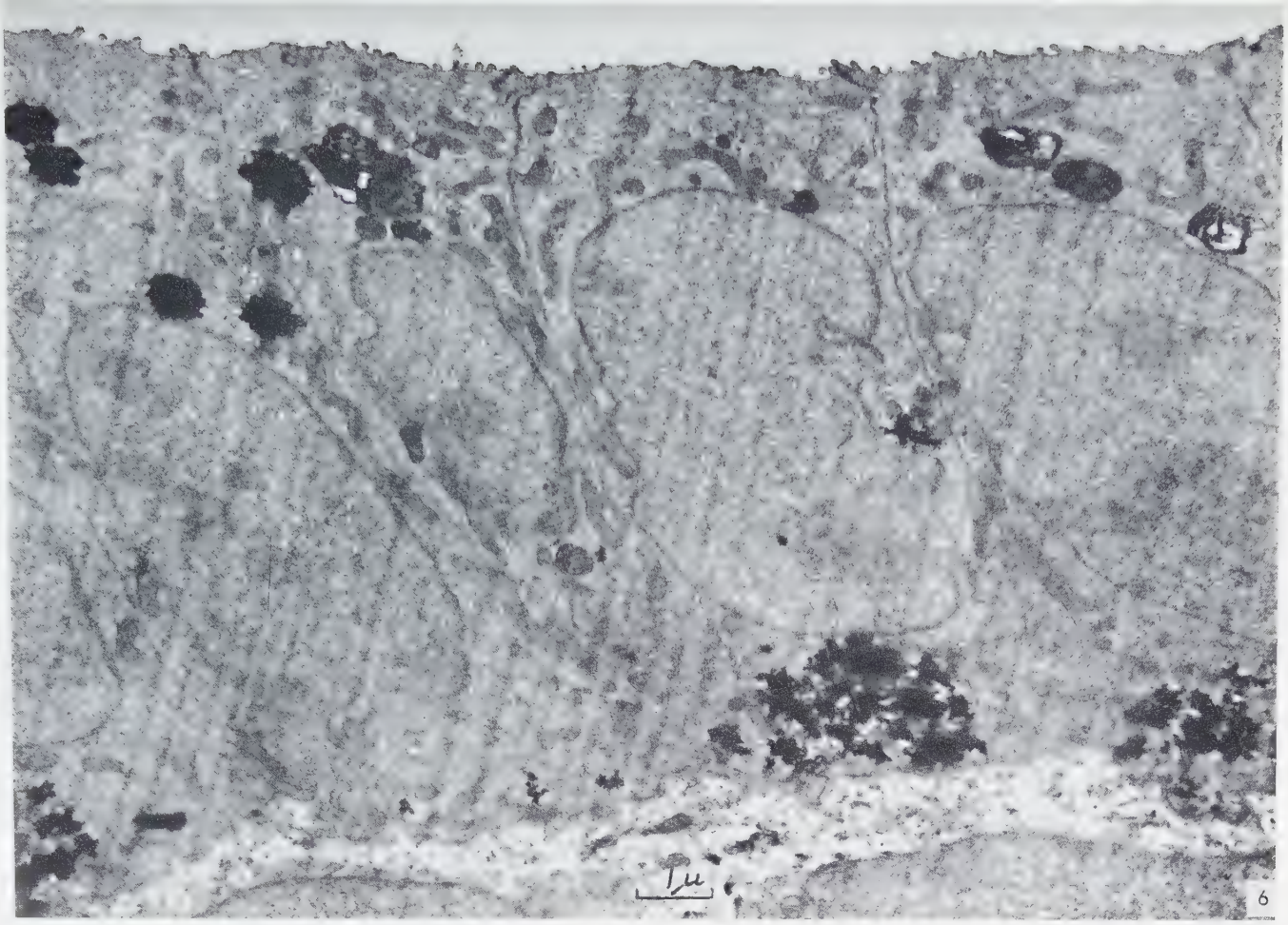

FIG. 6. Survey picture of uterine epithelium 4 days after injection of estrogen. The lumenal cell surface is plain and shows small microvilli. Lipid granules are seen in the apical and basal parts of the cells. The basement membrane and connective tissue are seen at the bottom. × 10,000.

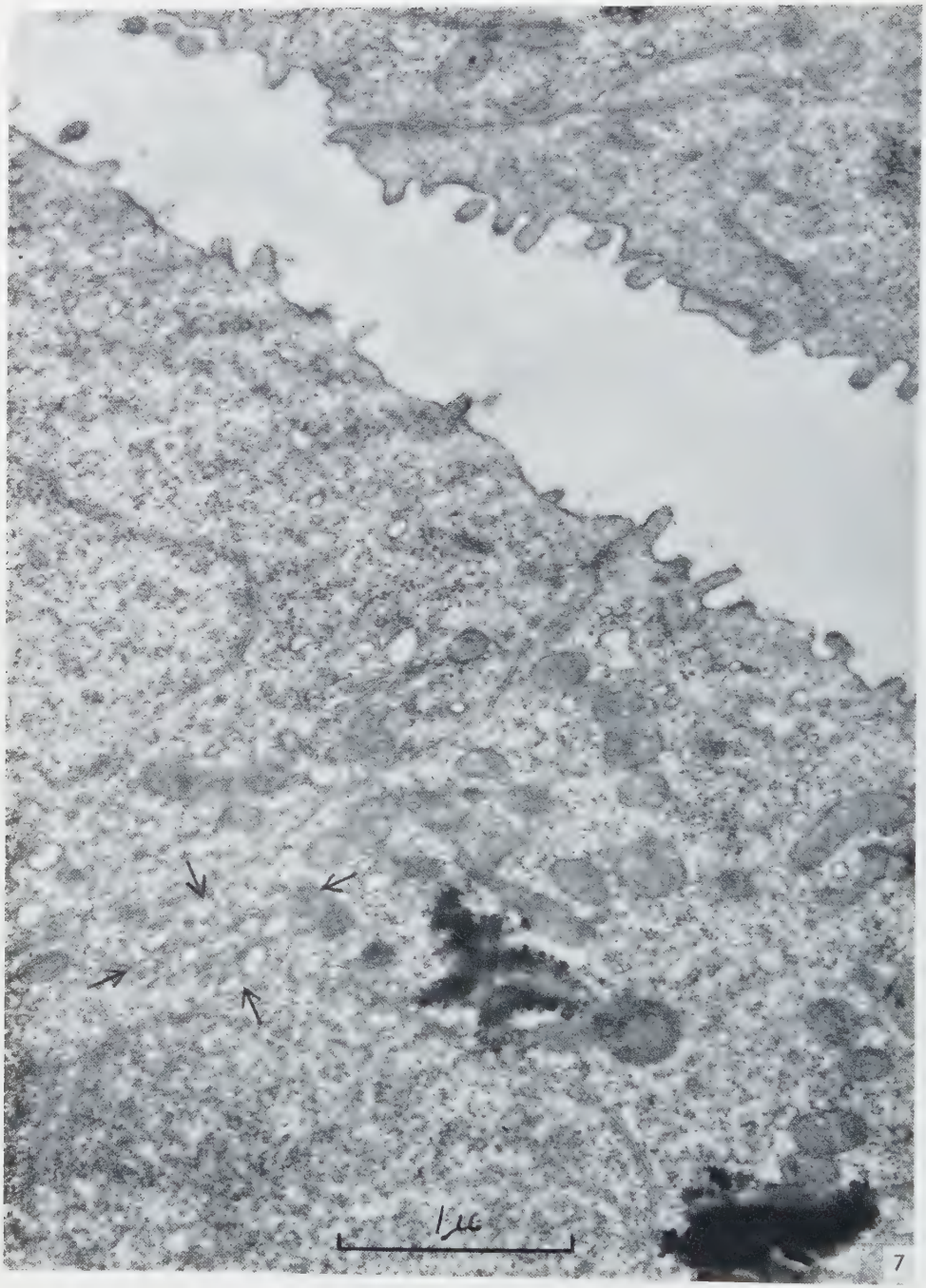

FIG. 7. Part of uterine epithelium 4 days after injection of estrogen. Microvilli are seen in the narrow lumen. Lipid granules and a Golgi apparatus (→) are visible in the cytoplasm of the epithelial cell located in the lower half of the picture. × 32,000.

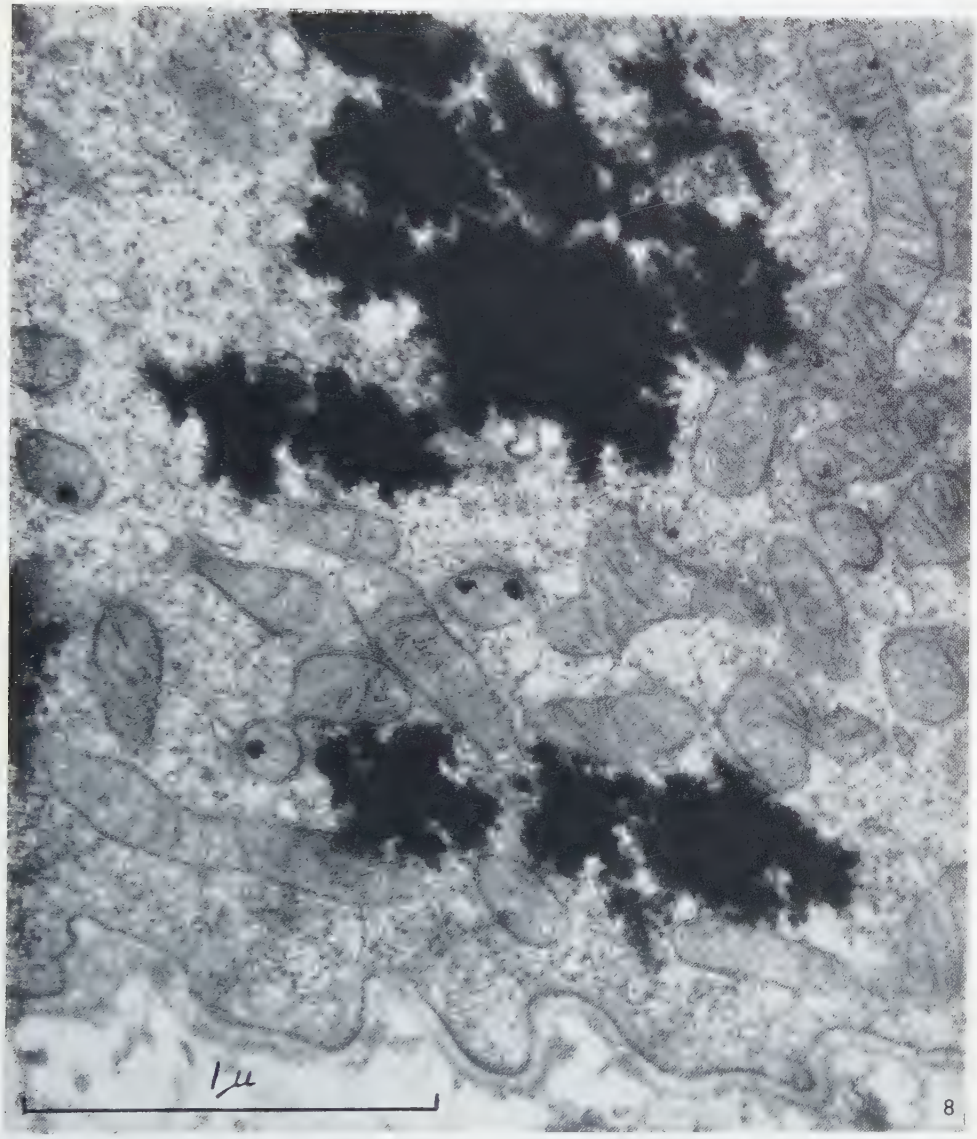

FIG. 8. Basal part of uterine epithelium 4 days after injection of estrogen. Lipid granules and mitochondria with small, dark granules are seen. The basement membrane is visible at the bottom. × 54,000.

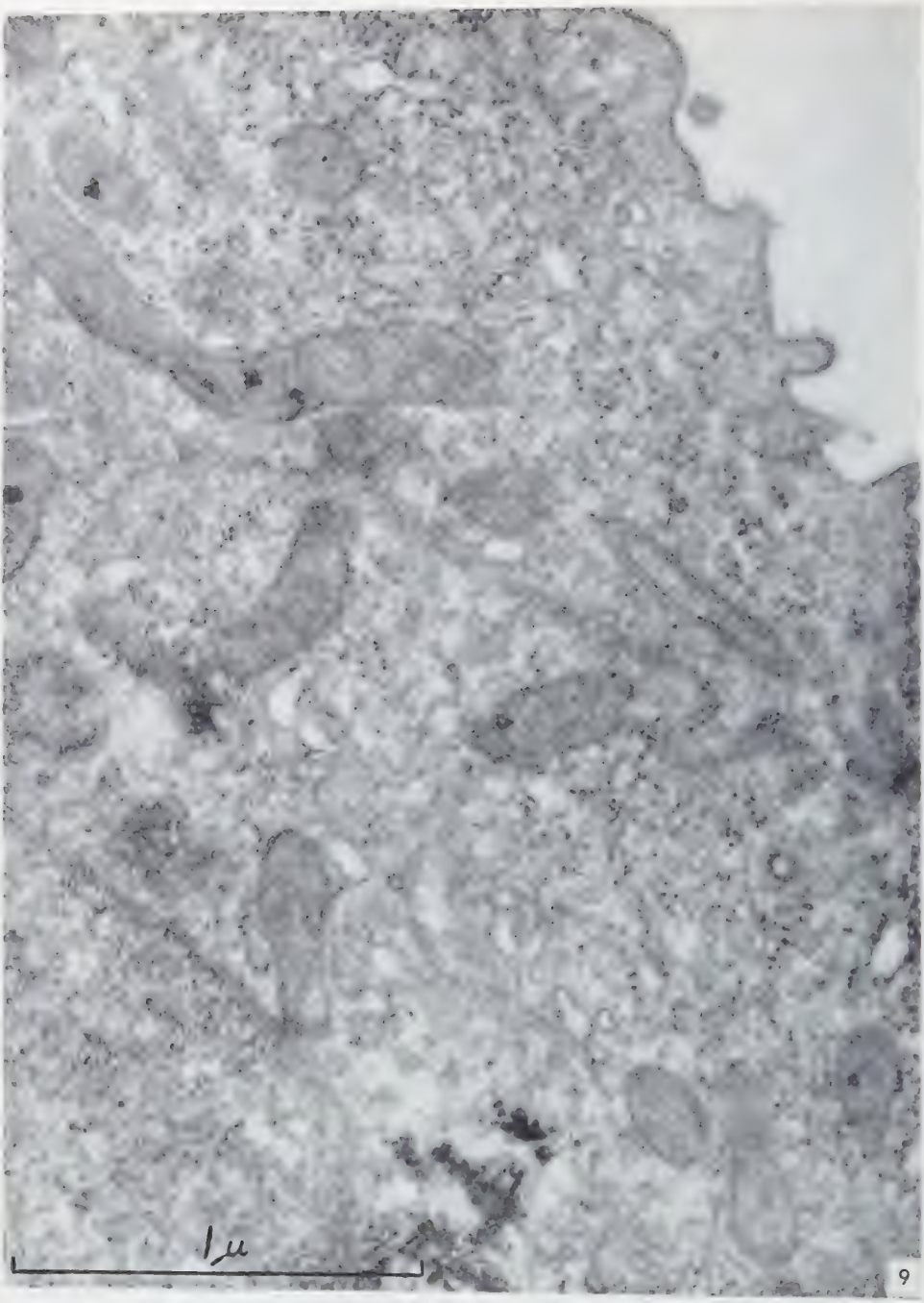

FIG. 9. Part of uterine epithelium 4 days after injection of estrogen. The lumenal cell surface is seen in the upper, right-hand corner, irregular cell borders are visible in the middle of the figure, and a portion of a nucleus is found in the lower, left-hand corner. To the right of the nucleus, fragments of lipid granules and a part of the Golgi apparatus are seen. To the left and above the nucleus, a vesicle with ring-shaped profiles appears. Mitochondria and ER-cytomembranes are also visible in the cytoplasm. × 56,000.

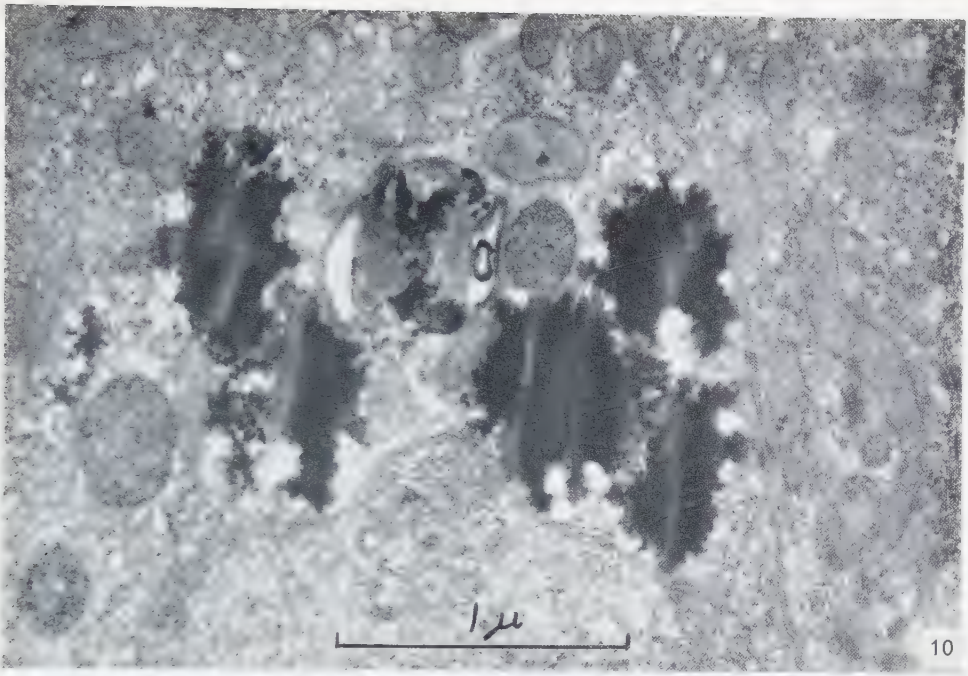

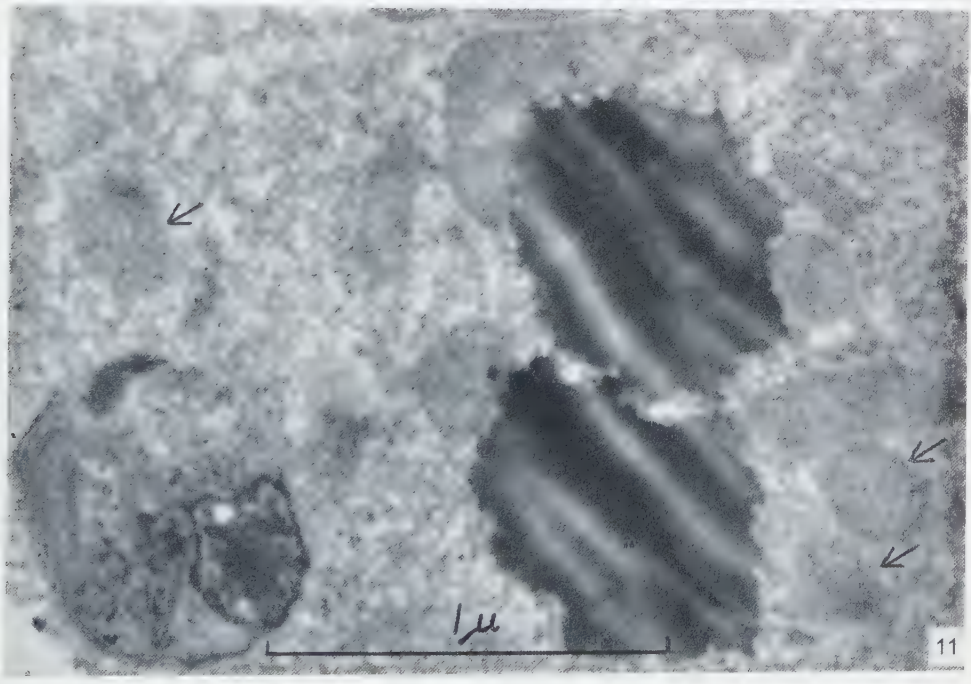

FIG. 10. Apical part of uterine epithelium 4 days after injection of estrogen. Above the nucleus, there is an accumulation of lipids, areas with granules and membranes, and cytoplasmic bodies. × 38,000.

FIG. 11. Part of uterine epithelial cell 4 days after injection of estrogen. Two lipid granules are seen surrounded by mitochondria and by granulated bodies (→). In the lower, left-hand corner, a structure is found, which has an intricate composition of granules, membranes, and dense substance. × 52,000.

of the microvilli. If some of the alkaline phosphatase is membrane-bounded (*7*, *27*, and others), these changes might contribute to the higher amount of alkaline phosphatase.

The lipid granules were seen as dark, homogeneous structures in the electron microscope. Some of the granules had a spherical shape, but most of them showed an irregular outline. This appearance might arise during the preparation procedure, which included a dehydration with ethyl alcohol.

The lipid granules were reported to diminish in number under the influence of estrogen (*5*, *16*). When the visible droplets of globular fat disappear from the cell, it is supposed (*8*) that the fat molecules are concealed as micellar fat in laminar micelles of phospholipid combined with protein. The combination of phospholipid and protein is common in the cell (*12* and others) and is visualized in the electron micrographs as a structure with alternating dark and light lines (*10*, *11*). It is probable that the membrane systems, which are connected to the lipid granules of this epithelium, also contain lipoprotein. As the estrogen injection caused a decrease in the number of the visible fat globules of the uterine epithelium with a simultaneous appearance of many lamellar structures, it is likely that these structures are concerned with the change of globular fat into micellar fat. The membrane systems were also present, when the lipid granules reappeared, which might imply that they are a basic structure concerned in fat metabolism of these cells.

The granulated bodies were commonly noticed in the uterine epithelial cells. As the bodies morphologically seem to be connected to the lipid granules and the complex areas of granules, membranes, and spaces (Figs. 3, 10 and 11), this might be an indication that they are cell organelles of importance in fat metabolism. Bodies of a similar appearance were suggested to be identical with the lysosomes, which are particles containing several enzymes (*21*).

Four days after the injection of estrogen into spayed mice, the ultrastructure of the uterine epithelium was further changed. The microvilli were shorter and more regular, and the lumenal substance had disappeared. But the cells were not yet quite similar to the cells from spayed animals. A difference was observed, in particular, between the shapes of the mitochondria from the two types of cells. In estrogen-treated animals, they appeared long compared to the small, rounded or rod-shaped mitochondrial profiles of spayed animals. However, 6 days after the injection of estrogen the epithelia from hormone-treated and spayed animals were similar.

Thus, the morphological changes in the uterine epithelium upon a single injection of estrogen last for 4 but not 6 days under the present experimental conditions. If animals are subjected to prolonged treatment with estrogen, the cornified vaginal smears will persist. The ultrastructure of the uterine epithelial cells under that condition will be described in a following paper (*20*).

"Professor Erik Ahlströms fond för obstetrisk-gynekologisk forskning" and the Swedish State made grants towards the expenses of the investigation. AB. Leo, Hälsingborg, supplied the estrogen preparation.

REFERENCES

1. Allen, E., Francis, B. F., Robertson, L. L., Colgate, C. E., Johnston, C. G., Doisy, E. A., Kountz, W. B. and Gibson, H. V., *Am. J. Anat.* **34**, 133 (1924).
2. Atkinson, W. B. and Elftman, H., *Endocrinology* **40**, 30 (1947).
3. Augustin, E., Heidenreich, O. and Thilo, A., *Arch. Gynäkol.* **184**, 281 (1954).
4. Burrows, H., Biological Actions of Sex Hormones, p. 369. The University Press, Cambridge, 1949.
5. Bourg, R., *Compt. rend. soc. biol.* **103**, 918 (1930).
6. Crelin, E. S. and Levin, J., *Endocrinology* **57**, 730 (1955).
7. Danielli, J. F., *Symposia Soc. Exptl. Biol.* **8**, 502 (1954).
8. Dixon, K. C., *Quart. J. Exptl. Physiol.* **43**, 140 (1958).
9. Drasher, M. L., *J. Exptl. Zool.* **119**, 333 (1952).
10. Finean, J. B. and Robertson, J. D., *Brit. Med. Bull.* **14**, 267 (1958).
11. Finean, J. B., Sjöstrand, F. S. and Steinmann, E., *Exptl. Cell Research* **5**, 557 (1953).
12. Frey-Wyssling, A., *in* Büchner, F., Letterer, E. and Roulet, F. (Eds.), Handbuch der Allgemeinen Pathologie, II. Band, 1. Teil, p. 69. Springer Verlag, Berlin,1955.
13. Gelfant, S., Meyer, R. K. and Ris, H., *J. Exptl. Zool.* **128**, 219 (1955).
14. Hooker, C. W., *Anat. Record* **93**, 333 (1945).
15. Jeener, R., *Biochim. et Biophys. Acta* **2**, 439 (1948).
16. Masson, G. and Selye, H., *Federation Proc.* **1**, 59 (1942).
17. Newman, S. B., Borysko, E. and Swerdlow, M., *J. Research Natl. Bur. Standards* **43**, 183 (1949).
18. Nilsson, O., *J. Ultrastructure Research* **1**, 375 (1958).
19. —— *J. Ultrastructure Research* **2**, 73 (1958).
20. Nilsson, O., in preparation.
21. Novikoff, A. B., Beaufay, H. and de Duve, C., *J. Biophys. Biochem. Cytol.* **2**, No. 4, Suppl., 179 (1956).
22. Palade, G. E., *J. Exptl. Med.* **95**, 285 (1952).
23. Palade, G. E. and Siekevitz, P., *J. Biophys. Biochem. Cytol.* **2**, 671 (1956).
24. Pincus, G., *in* Pincus, G. and Thimann, K. V. (Eds.), The Hormones, Vol. II, p. 1. Academic Press, New York, 1950.
25. Pritchard, J. J., *J. Anat.* **83**, 10 (1949).
26. Rhodin, J., Correlation of Ultrastructural Organization and Function in Normal and Experimentally Changed Proximal Convoluted Tubule Cells of the Mouse Kidney. Thesis. Stockholm, 1954.
27. Rosenberg, Th. and Wilbrandt, W., *Intern. Rev. Cytol.* **1**, 65 (1952).
28. Sjöstrand, F. S., *Experientia* **9**, 114 (1953).
29. Talmage, R. V., *Proc. Soc. Exptl. Biol. Med.* **70**, 719 (1949).

L'inclusion au polyester pour l'ultramicrotomie[1]

ANTOINETTE RYTER et E. KELLENBERGER

Laboratoire de Biophysique, Université de Genève

Reçu le 23 septembre 1958

The use of polyester, as embedding material for ultrathin sections, completely avoids swelling of the tissue fragments and formation of bubbles. We have found Vestopal W to be a very adequate commercial polyester, when used with adequate initiator (tert. butyl perbenzoate) and activator (cobalt naphthenate). The embedding procedure is similar to that used for other embedding materials. Acetone must be used, however, instead of ethanol for the dehydration.

Even relatively thick polyester sections provide much higher resolution than methacrylate sections of comparable thickness. This fundamental difference can be ascribed to a different response of these embedding materials when bombarded with electrons: during decomposition and partial volatilization, methacrylate melts while Vestopal does not. As consequences of this melting, surface tension tends to compress the sectioned specimen, altering its spatial arrangement, while capillary effects blur the contours of its structural details. The specimens embedded in polyester, on the contrary, remain undistorted and clearly defined.

Il est généralement reconnu que la polymérisation irrégulière du méthacrylate entraîne très souvent, surtout dans les tissus végétaux et les bactéries, des gonflements allant jusqu'à l'éclatement de la cellule ou de certains organelles (*5*). Le gonflement est dû à la formation du polymère plus rapide à l'intérieur de la cellule qu'à l'extérieur, suivie du gonflement de ce polymère par le monomère entourant la cellule. Ce grave inconvénient a poussé plusieurs auteurs à rechercher d'autres matières d'inclusion : Birch-Andersen et Maaloe (*17*) ont introduit l'emploi des résines du groupe « Epoxy », dont l'araldite est actuellement un représentant bien connu (*9*). En collaboration avec un chimiste spécialiste nous avons préconisé l'emploi des résines du groupe des polyesters (*15*). La polymérisation régulière de ces copolymères, qui n'entraîne jamais aucun gonflement, nous a permis d'entreprendre des études systématiques sur les bactéries et les bactériophages (*14*, *16*, *23*). Employé pour d'autres cellules isolées ou des tissus, le polyester a donné également d'excellents résultats (*7*, *8*, *12*, *21*, *22*, *25*). La qualité des résultats que nous avons pu atteindre

[1] Ces recherches ont été effectuées avec l'appui du « Fonds National Suisse pour la Recherche Scientifique ».

nous paraît justifier la description plus détaillée de ce procédé, que nous exposons ici. Lors de l'emploi régulier de ces résines polyesters nous avons pu observer quelques caractéristiques qui les différencient du méthacrylate. La constatation la plus frappante fut que même des coupes relativement épaisses de polyester (700 Å, couleur or (*20*)) permettent d'obtenir une résolution excellente, contrairement au méthacrylate pour lequel la résolution décroît très rapidement avec l'épaisseur. C'est également grâce à ce phénomène que l'on peut obtenir avec les polyesters des contrastes suffisants, car si on était obligé d'utiliser des coupes aussi minces que celles qui donnent les meilleures images avec le méthacrylate, le contraste serait trop faible. Nous avons constaté de plus que les coupes en polyester sont beaucoup plus souvent striées (ce sont la plupart du temps de très petites stries serrées). Nous montrerons dans ce travail que toutes ces différences dépendent du comportement du polyester sous le faisceau électronique. Tandis que le méthacrylate fond et s'évapore partiellement, les polyesters ne changent pas de volume; n'étant point thermoplastiques, leur décomposition n'est normalement pas accompagnée d'une fusion. Nous discuterons les conséquences de cette fusion du méthacrylate sur la résolution et l'arrangement spatial des structures incluses.

DESCRIPTION ET CHOIX DES POLYESTERS, INITIATEUR ET ACTIVATEUR

Composition chimique des polyesters et leur mode de polymérisation

La description complète de la chimie et de la technologie des polyesters est exposée dans un livre récent de Bjorksten *et al.* (*3*). Nous nous bornons ici à n'en donner qu'un résumé.

Les polyesters se composent d'acides bicarboxyliques tels que les acides fumarique et maléique, estérifiés avec des alcools bi- ou trivalents et copolymérisés avec des monomères non saturés comme le styrène qui joint les chaînes entre elles, formant ainsi un réseau extrêmement rigide. En faisant varier les différents constituants, on peut obtenir un nombre élevé de polyesters différant entre eux par leurs propriétés chimiques et physiques.

Les polyesters que l'on trouve sur le marché sont des substances dont la copolymérisation est commencée mais encore incomplète, une sorte de prépolymère. Ils se présentent sous l'aspect de liquides souvent assez visqueux. Leur thermostabilité varie suivant les matières premières dont ils sont composés et les inhibiteurs qu'ils contiennent. La plupart peuvent se conserver plusieurs mois à 20 environ avant de présenter un degré de polymérisation trop avancé. Leur conservation au réfrigérateur prolonge encore leur « vie ».

Le durcissement de ces prépolymères est amorcé par un initiateur qui, en règle générale, est un peroxyde. L'adjonction d'un activateur permet de régulariser la polymérisation et d'obtenir une polymérisation complète à des températures relativement basses (60°). Le choix de ces substances et leur dosage est décisif pour les qualités du produit final. En effet, les deux adjuvants déterminent la longueur des chaînes du polymère ainsi que la possibilité de terminer les réactions en un temps utile. Nous parlerons de ce choix un peu plus loin.

Le durcissement des polyesters n'est pas une simple polymérisation, mais est accompagné simultanément de réactions de condensation, ce qui confère aux polymères des propriétés non thermoplastiques et une insolubilité totale dans les solvants organiques. La plupart des polyesters commerciaux sont extrêmement durs et cassants.

Le choix du polyester

La possibilité d'employer une de ces résines pour des inclusions et des coupes minces est gouvernée par les trois facteurs suivants : 1° La viscosité du prépolymère ne doit pas dépasser une certaine limite pour que la pénétration dans les tissus soit complète et suffisamment rapide. 2° La dureté du polymère doit être suffisamment réduite pour que l'on puisse obtenir facilement des coupes avec des couteaux de verre. 3° Les coupes obtenues doivent se dégager du couteau et s'étaler rapidement sur une surface d'eau.

Dans un premier travail nous avons décrit l'emploi de polyester préparé à l'échelle du laboratoire (*15*). Depuis nous avons constaté, après de nombreux essais, qu'il était impossible à cette échelle d'obtenir une constance suffisante des propriétés de coupe d'un lot de fabrication à l'autre. En effet, s'il est possible de faire varier à volonté, dans de larges limites, les propriétés de viscosité du produit initial et de dureté finale des polyesters, il est impossible de prévoir la variation des propriétés de coupe, et même des blocs de dureté identique mais de composition légèrement différente peuvent montrer de grandes différences à ce point de vue. Nous avons alors essayé des polyesters de différentes provenances commerciales. Suivant une suggestion de Hotz nous avons étudié en particulier les produits Vestopal (Chemische Werke Hüls) qui sont déjà employés pour des inclusions d'objets macroscopiques (*10*). Ce produit existe en deux duretés : W (« weich ») et H (« hart ») et possède une viscosité voisine de celle du miel. Nous avons constaté que malgré cette viscosité plus élevée que celle du méthacrylate, la pénétration est bonne même dans les tissus à parois cellulaires épaisses comme les tissus végétaux. Il est indispensable cependant d'introduire les tissus par étapes successives du déshydratant dans le prépolymère. La dureté du polymère de Vestopal W obtenu avec les initiateur et activateur décrits plus loin est un peu plus grande que celle du mélange méthylméthacrylate–butylméthacry-

late 1 : 9 généralement employé. Mais il est néanmoins très facile d'obtenir des coupes bien étalées et des rubans de coupes successives (*24*). Il est possible de varier la dureté du Vestopal dans de larges limites sans affecter les bonnes propriétés de coupe : on peut obtenir un produit plus dur en mélangeant le Vestopal W avec du Vestopal H ou un produit plus mou en ajoutant 2–10% de dibutylphtalate comme plastifiant.

Le choix et le dosage de l'initiateur et activateur

Il existe un nombre élevé de produits fonctionnant comme initiateurs et comme activateurs (*3*). Selon la combinaison de ces adjuvants et leur dosage on obtient une polymérisation à des températures allant de la température de chambre à des températures plus élevées. Nous avons recherché des produits suffisamment peu actifs pour pouvoir faire toutes les manipulations d'inclusion à la température de chambre sans précautions particulières et tout de même suffisamment vigoureux pour que la polymérisation puisse se faire à une température ne dépassant pas 60° et se terminer en 24 ou au maximum 48 heures. Nous avons étudié un certain nombre de combinaisons susceptibles de satisfaire ces conditions. L'expérimentation de ces produits doit obligatoirement se faire en présence de tissus car dans plusieurs cas la dureté du polymère à l'intérieur du tissu est inférieure de celle du polymère seul. Il est probable que le tissu agit indirectement sur la polymérisation par l'intermédiaire des initiateur et activateur et empêche de ce fait la polymérisation de suivre sa progression normale à l'intérieur du tissu. De plus le dosage de chaque produit doit être soigneusement établi car il se répercute d'une façon critique sur la dureté du polymère. En règle générale la dureté du polymère augmente jusqu'à un maximum en fonction de la concentration de l'initiateur ou de l'activateur pour décroître ensuite de nouveau. Le maximum de dureté correspond à une polymérisation complète et doit toujours être recherché.

Pour effectuer cette expérience, on introduit des quantités variables de l'un des adjuvants dans le Vestopal accompagné d'une quantité adéquate et constante de l'autre adjuvant. On fait polymériser ce mélange à 60 en présence de tissu déshydraté selon la technique décrite plus loin. On choisira comme dose correcte la concentration minimum permettant d'atteindre le maximum de dureté.

La combinaison que nous employons actuellement est le Vestopal W avec le tert. butyl perbenzoate comme initiateur et le naphténate de cobalt comme activateur.[1]

Parmi les autres initiateurs essayés, le peroxyde de benzoyle s'est révélé adéquat. Il présente cependant le désavantage d'être sous forme solide ce qui complique

[1] Les trois produits peuvent être obtenus commercialement par la Maison M. Jaeger, Vésenaz, Genève (Suisse), testés avec ajustage exact de l'initiateur et de l'activateur à ajouter.

considérablement son emploi et sa dissolution dans le Vestopal. Le peroxyde d'éthyl–méthyl–cétone, le tert. butylhydroperoxyde et le peroxyde de cumène n'ont pas donné entière satisfaction pour diverses raisons.

Le lauryl mercaptan employé comme activateur donne également de bons résultats.

LA MÉTHODE D'INCLUSION

Le Vestopal n'étant pas miscible à l'alcool, la déshydratation doit se faire à l'acétone (*15*) dont l'emploi s'est révélé sans inconvénient en microscopie électronique même dans le cas d'autres matières d'inclusion (*19*).

La viscosité relativement élevée du Vestopal W nécessite le passage progressif du tissu à partir de l'acétone sec dans le Vestopal afin d'éviter des contractions trop fortes. Ces passages progressifs se font en laissant séjourner les fragments de tissus dans trois mélanges acétone–Vestopal dont la teneur en Vestopal croît du premier au troisième, pour aboutir finalement dans du Vestopal dépourvu d'acétone.

Préparation des mélanges :

Mélange I : acétone sec 3 parties–Vestopal 1 partie
Mélange II : acétone sec 1 partie–Vestopal 1 partie
Mélange III : acétone sec 1 partie–Vestopal 3 parties
Mélange IV : Vestopal + 1 % d'initiateur « Jaeger » + 0,5 % d'activateur « Jaeger »

Pour faire ce dernier mélange, il faut d'abord introduire l'initiateur et l'incorporer soigneusement au Vestopal avant d'ajouter l'activateur que l'on mélange également avec soin. Ce mélange IV doit se faire juste avant son emploi, car il ne se conserve que quelques heures à la température de la chambre.

Technique d'inclusion :

Déshydratation :	acétone	30 %	15–30 minutes
	»	50 %	15–30 »
	»	75 %	15–30 »
	»	90 %	30–60 »
	»	100 %	30–60 »
Inclusion :	mélange	I	30–60 »
	»	II	30–60 »
	»	III	30–60 »
	»	IV	30–60 »

capsules remplies de mélange IV laissées à 60° pendant 12 à 24 heures

La régularité de polymérisation du Vestopal se remarque macroscopiquement par la dureté régulière du polymère d'un bloc à l'autre et d'une inclusion à l'autre. Si la déshydratation et l'inclusion ont été convenablement faites, il n'y a jamais de bulles d'air autour du fragment de tissu.

La régularité de polymérisation se manifeste également sur la conservation du tissu et les résultats absolument reproductibles que l'on obtient d'une série d'inclusion à l'autre. Nous n'avons jamais noté aucun gonflement ou déformation dans les divers tissus étudiés.

Cependant, il est important de veiller à ce que la polymérisation soit complète, en particulier dans la partie du bloc qui contient le tissu, et qui polymérise presque toujours un peu plus lentement. Une polymérisation incomplète se manifeste toujours par des difficultés lors de la coupe.

Coupes :

Le Vestopal se coupe très facilement avec des couteaux de verre ainsi que de diamant (*21*, *22*). Les coupes s'étalent immédiatement et parfaitement si l'on a soin de couper assez lentement, de ne pas faire de trop grandes coupes et d'utiliser un angle de coupe inférieur à 45°. Si l'angle de coupe dépasse cette valeur, les coupes se tassent très facilement en formant une multitude de petits plis parallèles. Les tassements ne se défont plus, même sur de l'eau contenant de l'acétone ou de l'alcool. Cette exigence se traduit par la nécessité d'un soin particulier lors du choix de l'angle du couteau et lors de la mise en place du couteau.

La déformation elliptique très fréquente avec le méthacrylate (*20*) est très rare avec le polyester. On note parfois certaines déformations des parois nucléaires et cellulaires qui proviennent de contractions. Il est facile d'obtenir des rubans réguliers de coupes grises donc de moins de 600 Å d'épaisseur (*20*, *24*). Il est cependant plus difficile d'obtenir de longs rubans car les coupes n'adhèrent pas très bien les unes aux autres comme pour le méthacrylate. Il suffit cependant de tremper la pyramide dans une solution de Formvar, pour augmenter cette adhérence (*2*).

LE COMPORTEMENT DES COUPES POLYESTER SOUS LE FAISCEAU ÉLECTRONIQUE

Aspect des coupes polyester au microscope électronique

Il a été clairement démontré par Morgan *et al.* (*18*) que les coupes en méthacrylate subissent un éclaircissement marqué sous le faisceau électronique, éclaircissement qui est accompagné en même temps par la disparition des stries et par une augmentation considérable du contraste. Nous n'avons pas étudié quantitativement cet éclair-

cissement pour les coupes en polyester, mais nous l'avons constaté. Il est cependant moins frappant qu'avec le méthacrylate surtout si l'on augmente l'intensité du faisceau très progressivement. Les stries dues aux défauts du couteau restent parfaitement visibles. Un éclaircissement plus marqué se manifeste si l'on expose la coupe très brusquement à une forte intensité d'électrons. Dans ce cas, on voit de plus la coupe s'émailler de grains très fins. Nous parlons alors de « coupe brulée », phénomène que l'on tend à éviter en général.

L'observation la plus étonnante cependant est la résolution encore excellente que conservent des coupes d'apparence grise au microscope électronique donc relativement épaisses, résolution que l'on ne peut jamais observer dans des cas analogues avec le méthacrylate. Même des coupes de couleur dorée sur l'eau permettent encore d'obtenir une résolution suffisante sur les micrographies.

Nous avons pensé que ces différences de résolution devaient être étroitement liées au mécanisme de décomposition du matériel d'inclusion. Pour éclaircir ces problèmes nous avons comparé l'état de la surface des coupes de polyester et de méthacrylate avant et après avoir été irradiées par le faisceau électronique.

Transformation des coupes sous le faisceau électronique

La technique de l'ombrage permet d'obtenir des renseignements sur l'état d'une coupe avant l'observation (*27*). En effet, quand on ombre suffisamment fortement une coupe avant l'observation, la configuration de la couche d'ombrage représente l'état de la coupe avant l'observation, même dans le cas où l'observation entraîne des modifications assez profondes. L'ombrage après une première observation, par contre, permet de saisir les transformations qu'aura subies la coupe lors de la première observation.

Williams et Kallman (*27*) ont rapporté dans une étude fouillée effectuée à l'aide de cette technique, que les coupes au méthacrylate subissent un amincissement considérable sous le faisceau électronique. Cet amincissement affecte surtout le matériel d'inclusion et fait ressortir les structures incluses. Nous avons répété ces expériences sur le méthacrylate et le polyester.

Nous avons utilisé un microscope RCA EMU 2-D à 50 kV, avec un diaphragme de 260 μ dans le condenseur et un diaphragme contraste Canalco de 50 μ. Nous employions

---

FIG. 1. Inclusion dans le méthacrylate, ombrage avant l'observation. 36.000 ×.
FIG. 2. Inclusion dans le méthacrylate, ombrage après une première observation, coupe relativement mince. 36.000 ×.
Toutes les micrographies concernent des bactéries Escherichia coli B–B contenant des bactériophages T2r, et prélevées 30 minutes après l'infection. Fixation selon nos conditions standard et déshydratation à l'acétone.

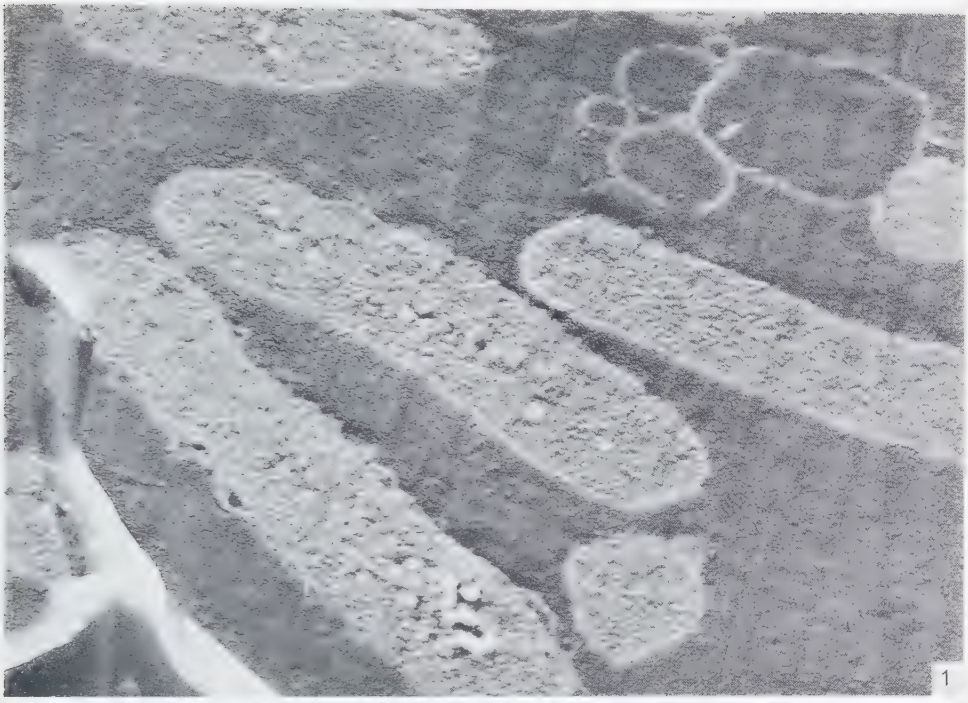

1

2

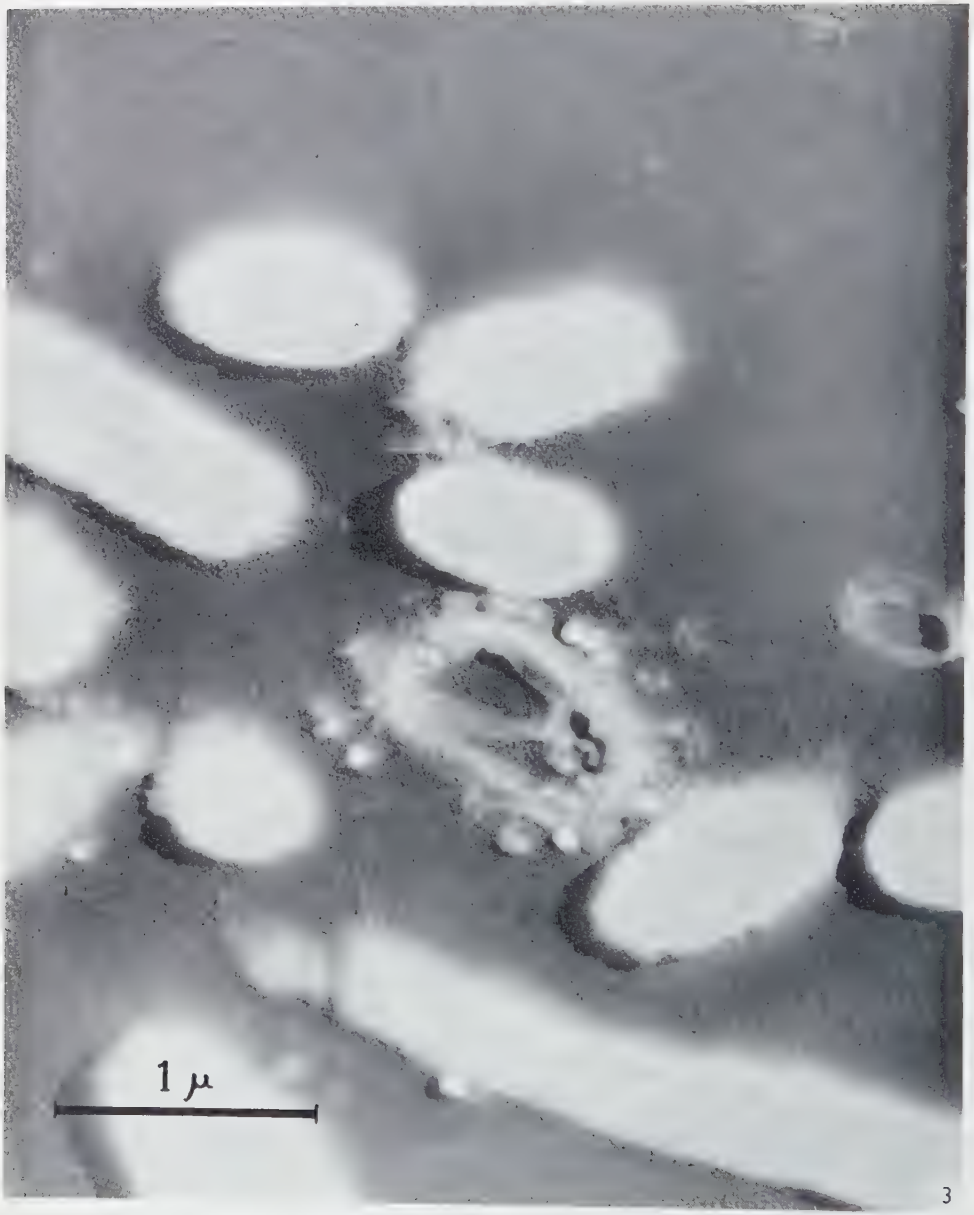

FIG. 3. Coupe épaisse d'une inclusion en méthacrylate, ombrée après une première observation. 36.000 ×.

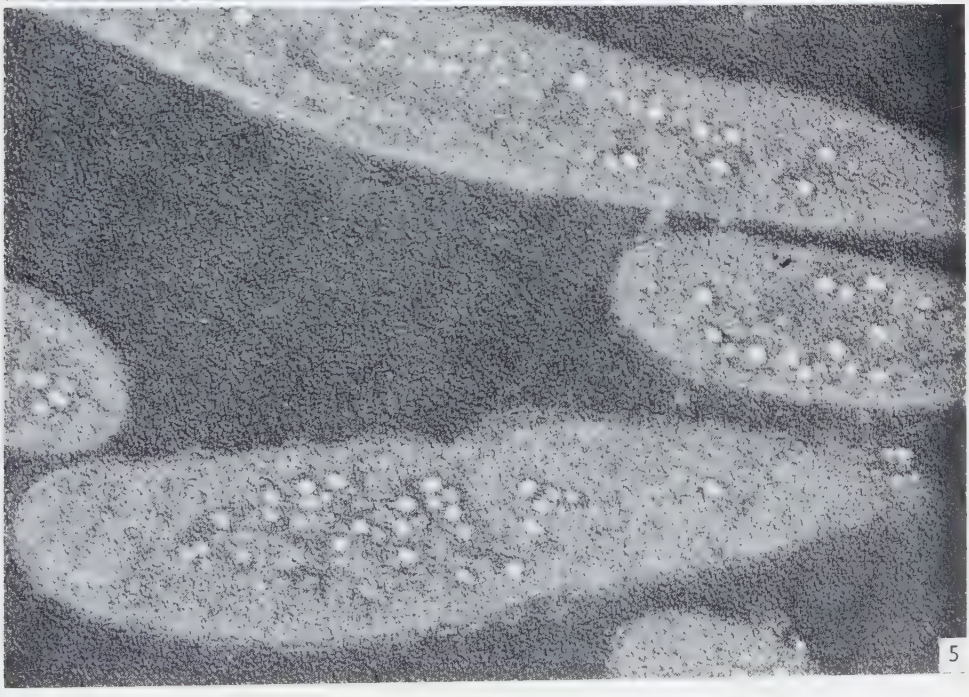

FIG. 4. Inclusion en Vestopal W, ombrage avant l'observation. 36.000 .
FIG. 5. Inclusion en Vestopal W, ombrage après une première observation. 36.000 .

des grossissements de 8000 à 10.000 au maximum pour n'être pas obligés d'exposer la coupe à des intensités électroniques trop fortes. Ainsi nous n'obtenons pas de « coupes brûlées ». L'ombrage est effectué avec de l'UO_2 sous un angle approximatif de 30°.

Avant une première observation les coupes de méthacrylate et celles de polyester offrent un aspect sensiblement identique (fig. 1 et 4). Leur surface est plane, sillonnée très souvent de nombreuses petites stries. Le nombre de ces dernières est statistiquement pareil dans les deux cas. Les bactéries et les phages qu'elles contiennent ne font pas saillie à la surface de la coupe. On note parfois un léger détachement des bactéries et des phages du côté où le couteau les a touchés en premier.

Après exposition aux électrons, les coupes de méthacrylate offrent l'aspect déjà décrit par Williams et Kallman (*27*), c'est-à-dire que les bactéries et les phages qu'elles contiennent sont en relief par rapport au fond de méthacrylate (fig. 2 et 3). Leurs contours sont arrondis et un peu flous. Cet aspect s'accentue avec l'épaisseur de la coupe. La figure 3 qui est l'image d'une coupe très épaisse montre en effet des ombres très longues ce qui indique un fort relief et les contours des bactéries extrêmement arrondis et flous. Les phages adsorbés sur les parois ne sont plus entourés par le matériel d'inclusion mais ont l'air d'être posés sur le fond de méthacrylate.

Les stries ne sont plus visibles sur le fond de la coupe mais on les devine dans le cytoplasme bactérien. Parfois une rangée de trous dans le méthacrylate témoigne des plus gros défauts du couteau.

Les coupes de polyester irradiées (fig. 5) n'offrent que peu de changement par rapport à leur aspect primitif avant l'observation au microscope électronique (fig. 4). Leur surface est plane et les bactéries ne présentent aucun relief. Les stries restent aussi visibles qu'avant. On note parfois une granulation un peu plus marquée de la surface. Cette granulation devient d'autant plus importante que les coupes ont été fortement irradiées. Il doit s'agir ici de l'image de la décomposition de la matière organique.

Les coupes de polyester qui ont été irradiées très brusquement en amenant rapidement une partie de coupe non encore observée sous le faisceau au maximum d'intensité (diaphragme dans le condenseur 650 μ) présentent parfois également un certain relief. Ce phénomène n'apparaît que dans des conditions très spéciales, tandis que pour le méthacrylate les intensités employées pour l'observation sont suffisantes pour produire le phénomène.

CONCLUSION ET DISCUSSION

On sait que les substances organiques subissent des transformations chimiques profondes par l'action conjuguée de la température élevée et de la ionisation produite dans le spécimen sous l'influence des électrons (*4*, *11*). L'étendue de cette décomposi-

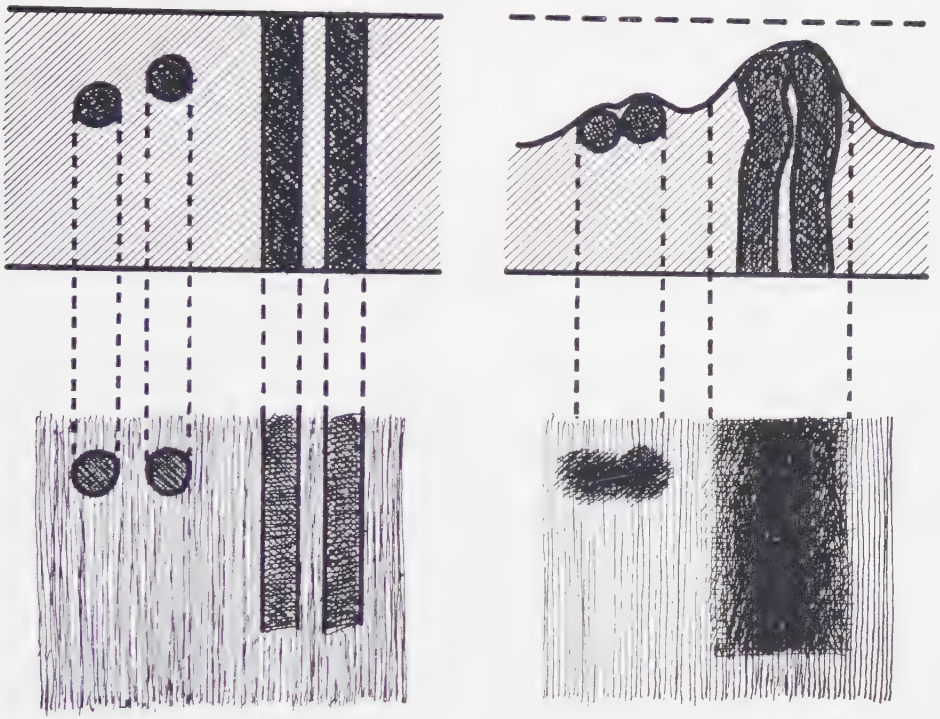

FIG. 6. Influence de la fusion du matériel d'inclusion sur l'arrangement spatial et sur la formation de l'image.

tion est encore mal connue. Von Borries admet une perte d'environ 50% de la matière qui serait volatilisée, même avec une intensité courante. Il paraît cependant évident qu'aucune règle générale ne peut être émise, car la décomposition doit dépendre aussi bien de la composition initiale du spécimen que de la façon d'administrer le rayonnement électronique (*26*). L'augmentation de contraste observée sur les coupes lors de l'irradiation électronique est certainement l'expression d'une décomposition différente des structures incluses et du matériel d'inclusion.

Les expériences que nous rapportons ici prouvent que la réaction du méthacrylate envers les électrons est très différente de celle du polyester. Tandis que le méthacrylate subit une fusion et une évaporation le polyester subit une sorte de distillation sèche. Des substances volatiles quittent la résine sans cependant provoquer le changement de volume de la coupe, mais cette perte de matière abaisse par contre sensiblement la densité du polymère. Puisque nous savons que le méthacrylate est thermoplastique et que le polyester ne l'est pas, cette réaction différente est en réalité peu surprenante.

Dès l'exposition au faisceau électronique le méthacrylate doit fondre par suite de l'échauffement, s'évaporer partiellement puis se solidifier probablement à nouveau au cours de sa dénaturation.

Le passage par l'état liquide entraîne des conséquences importantes pour l'aspect de la coupe de méthacrylate. Nous savons que l'épaisseur du méthacrylate est réduite d'environ 50%. La tension superficielle doit donc exercer une compression sur les tissus inclus. Des membranes peu rigides p.ex. doivent être fortement déformées (*20*) avant d'émerger à la surface de la matière d'inclusion, comme le montre la figure 6. De plus, des composants particulaires seront déplacés et auront tendance à se rapprocher les uns des autres ou à s'accoler à d'autres structures. Ces phénomènes ont été décrits de façon détaillée pour les suspensions de particules préparées par évaporation (*1*). L'état liquide a cependant encore d'autres répercussions fâcheuses: la capillarité tend à remplir et à arrondir les angles formés par des structures saillant hors de la surface du liquide et produit ainsi un « empâtement » des structures fines. L'épaisseur du méthacrylate et par conséquent le pouvoir diffuseur envers les électrons n'étant pas constants, il se produit un « dégradé » autour de l'image électronique des structures, qui n'offriront donc plus une image bien définie. Cette situation est également indiquée dans la figure 6.

Le polyester ne passant pas par un état liquide, la décomposition n'agit qu'à l'échelle moléculaire et se manifeste par la surface plus rugueuse de la coupe de polyester. Il est facile de comprendre maintenant que même des coupes épaisses de polyester permettent d'atteindre une bonne résolution, car les effets de compression et de capillarité n'ont pas lieu.

Des coupes sériées de bactériophages présentées dans un autre travail (*24*) démontrent que des coupes de 500–550 Å donnent encore d'excellentes images. Cette épaisseur correspond d'ailleurs à des mesures effectuées récemment sur les coupes de méthacrylate (*20*). Les épaisseurs de coupes généralement indiquées ne correspondent donc que rarement à la réalité. La règle empirique indiquée par Cosslett (*6*) et qui énonce que la résolution atteignable dans une coupe d'épaisseur d est égale à $d/10$ nécessitera une certaine révision. Elle n'est applicable que pour les coupes en méthacrylate, où la diminution de la résolution est la conséquence de la capillarité et de la compression plutôt que d'une augmentation de l'erreur chromatique. Si l'on calcule l'erreur chromatique introduite par le ralentissement des électrons dans la préparation, on s'aperçoit que même des coupes de 600 Å d'épaisseur d'une densité de 0,6 environ n'introduisent une erreur chromatique que de 4 Å environ[1], tandis que selon la

[1] Selon von Borries (*4*) la formule pour l'erreur chromatique est $\delta = \alpha c \Delta u/u$ où α est l'ouverture numérique, c la constante de l'objectif (valeur mesurée et égale à 0,18 pour une lentille magnétique et à 2,3 pour une lentille électrostatique) et u la tension d'accélération des électrons. Selon une formule de Lenard (*4*) $\Delta u/u$ peut être fixé approximativement à $\Delta u/u \quad 50 \varrho x$ lorsque la tension employée est de 50 kV; ϱ est la densité du matériel et x son épaisseur; si nous choisissons $\varrho = 0{,}6$ pour la matière

règle empirique la résolution n'atteindrait que 60 Å. Les observations que nous avons faites sur des bactéries infectées avec des phages nous ont montré que l'on peut atteindre facilement une résolution d'au moins 20 Å sur des coupes d'une épaisseur de 500 Å environ. Il est évident que dans les coupes relativement épaisses de polyester, les différentes couches d'une membrane par exemple ne sont visibles que dans le cas où la membrane est perpendiculaire au plan de la coupe, condition qui dépend du hasard. On constate en effet que les structures fines stratifiées ne sont en général visibles comme telles, que sur des portions relativement courtes de ces structures (*13*).

Les stries si visibles sur les coupes de polyester sont également liées au comportement du polyester sous le faisceau électronique différent de celui du méthacrylate. On s'aperçoit que les tissus inclus dans le polyester ne sont pas plus endommagés par le couteau que ceux inclus dans le méthacrylate puisqu'autant de stries sont visibles sur les coupes de méthacrylate et de polyester avant exposition aux électrons. Leur absence dans les coupes de méthacrylate non ombrées ou ombrées après une première exposition aux électrons est donc due à leur disparition au cours de la fusion du matériel d'inclusion. Cette disparition ne supprime par contre pas les dégâts que les défauts du couteau ont produits dans les tissus. On s'aperçoit donc que si au premier abord la visibilité des stries sur les coupes de polyester semble présenter un désavantage, elle permet au contraire de distinguer facilement et avec sécurité les coupes les moins endommagées par le couteau et qui dans ce cas sont exemptes de stries de celles qui ont davantage souffert et qui risquent de présenter des arrachements et des altérations des structures fines souvent difficilement discernables sur l'écran du microscope électronique.

En conclusion, on peut affirmer que, comme la théorie le laissait prévoir, le polyester et le méthacrylate se comportent très différemment sous le faisceau électronique. Cette différence dans le comportement permet d'expliquer celle qui existe entre l'aspect des coupes de polyester et celles de méthacrylate.

REMERCIEMENTS

Nous tenons à remercier tous ceux de nos amis étrangers, des membres associés ou des hôtes de notre laboratoire qui ne se sont pas découragés dans l'emploi du polyester malgré les difficultés et déboires du début. Leurs critiques et suggestions ont été indispensables à

organique décomposée et $x = 600$ Å nous obtenons $\delta = 3{,}5$ Å dans le cas de la lentille magnétique et 45 Å pour la lentille électrostatique. Cette différence explique parfaitement pourquoi les microscopes électrostatiques se sont révélés inadéquats pour l'observation des coupes.

Concernant l'erreur de sphéricité, nous savons que les électrons subissent en moyenne chacun un choc élastique pour une épaisseur de 2900 Å de « carbone biologique ». Pour une épaisseur de 600 Å il y a certainement au moins 70 % des électrons qui ne subissent pas de déviations au cours de leur trajet. L'influence sur la résolution est donc négligeable.

la mise au point définitive de ce procédé. Nous avons une dette de reconnaissance tout particulière envers A. Gautier et son collaborateur I. Marcovici du Centre de microscopie électronique de Lausanne avec qui nous avons eu maintes discussions fructueuses et qui ont apporté des suggestions très utiles. Nous remercions également M^lle^ Sigrid von Taeuffenbach pour l'aide technique précieuse qu'elle nous a apportée dans ce travail.

Nous remercions les Maisons Hüls à Marl (Recklinghausen, Allemagne) et Noury & van der Lande à Deventer (Hollande) pour des échantillons de diverses substances.

BIBLIOGRAPHIE

1. Anderson, T. F., *Compt. rend. congrès de microscopie électronique, Paris* 1950, p. 567. Rev. opt., 1953.
2. Anderson, T. F., communication personnelle.
3. Bjorksten, J., Tovey, H., Harker, B. et Henning, J., Polyesters and their Applications. Reinhold Publishing Corp., New York, et Chapman and Hall Ltd., London, 1956.
4. Borries, B. von, Die Übermikroskopie. Verlag Editio Cantor, Aulendorf Württ., 1949.
5. Borysko, E., *J. Biophys. Biochem. Cytol.* **2**, Suppl., 3 (1956).
6. Cosslett, V. E., *J. Biophys. Biochem. Cytol.* **3**, 815 (1957).
7. Feissly, R., Gautier, A. et Marcovici, I., *Compt. rend.* VII^e^ *congr. soc. intern. transf. sang., Rome*, 1958.
8. Gautier, A., Frei, J. et Ryser, H., *Proc. Fourth Intern. Conf. Electron Microscopy, Berlin*, 1958, sous presse.
9. Glauert, A. M. et Glauert, R. H., *J. Biophys. Biochem. Cytol.* **4**, 191 (1958).
10. Goslar, H. G., *Anat. Anz.* **101**, 100 (1954).
11. Hall, C. E., Introduction to Electron Microscopy. McGraw-Hill Publ. Co., Ltd., London, 1953.
12. Heitz, E., *Z. Naturforsch.* **12 b**, 283 (1957).
13. Kellenberger, E. et Ryter, A., *J. Biophys. Biochem. Cytol.* **4**, 323 (1958).
14. Kellenberger, E., Ryter, A. et Séchaud, J., *J. Biophys. Biochem. Cytol.*, sous presse.
15. Kellenberger, E., Schwab, W. et Ryter, A., *Experientia* **12**, 421 (1956).
16. Kellenberger, E., Séchaud, J. et Ryter, A., en préparation.
17. Maaloe, O. et Birch-Andersen, A., Bacterial Anatomy, p. 261. Cambridge Univ. Press, 1956.
18. Morgan, C., Moore, D. H. et Rose, H. M., *J. Biophys. Biochem. Cytol.* **2**, Suppl., 21 (1956).
19. Mühlethaler, K., communication personnelle.
20. Peachey, L. D., *J. Biophys. Biochem. Cytol.* **4**, 233 (1958).
21. Policard, A., Collet, A. et Prégermain, S., *Bull. microscop. appl.* **7**, 49 (1957).
22. —— *ibid.* **7**, 73 (1957).
23. Ryter, A. et Kellenberger, E., *Z. Naturforsch.* **13 b**, 597 (1958).
24. Séchaud, J., Ryter, A. et Kellenberger, E., en préparation.
25. Vogel, A. et Glatthaar, E., *Oncologia* **11**, 138 (1958).
26. Watson, M. L., *Biochim. et Biophys. Acta* **10**, 349 (1953).
27. Williams, R. C. et Kallman, F., *J. Biophys. Biochem. Cytol.* **1**, 301 (1955).

A Quantitative Study of the Effects of Mercuric Chloride on the X-Ray Diffraction Data from the Myelin Sheath of Frog Sciatic Nerve

P. F. MILLINGTON and J. B. FINEAN

Department of Medical Biochemistry and Pharmacology, The Medical School, The University of Birmingham

Received July 16, 1958

Quantitative relationships between changes in the diffraction pattern of nerve myelin and the amount of mercuric chloride introduced into the nerve tissue have been demonstrated. The possible positions of the mercuric ions in the myelin unit have been predicted from a consideration of Difference Patterson functions. This information has been used to derive electron density distributions for the mercuric chloride treated myelin.

From polarised light (*16–18*), X-ray diffraction (*8*, *19*, *20*) and electron microscope studies (*2–4*, *11*, *14*, *21*), it has been possible to suggest general structural features of the myelin sheath. Further information on the nature and location of specific (molecular) groups in the layered lipoprotein system has been sought from studies of the interactions of heavy ions. Qualitative studies of the changes in the X-ray diffraction pattern of frog sciatic nerve resulting from treatment with solutions containing various heavy ions (*6*, *13*) indicated the possibility of obtaining further information from detailed quantitative work. This paper deals with both the quantitative relationships found to exist between changes in the diffraction pattern and the amount of mercuric chloride taken up by the specimen and structural calculations based upon these results.

MATERIALS AND METHODS

Data on the frog sciatic nerve only are reported in this paper. Segments of nerve trunk were immersed in a mercuric chloride solution for various lengths of time and the moist specimens were sealed in thin-walled glass capillary tubes for examination in evacuated low-angle diffraction cameras (*5*, *7*) using $CuK\alpha$ radiation. The diffraction patterns were recorded on Ilford Industrial G X-ray film and plots of the line densities were made using a Hilger microdensitometer. The diffraction intensities were

then calculated from this plot of the film transmission values, estimating the effect of the background from the general slope of the curve. The diffracting powers of the specimens varied, and thus the densities of the bands from different specimens could not be compared directly. However, the ratios of the densities could be compared with the corresponding ratios in other patterns.

A preliminary investigation showed that changes could be induced at a suitable rate using 0.3% mercuric chloride in 0.6% saline. This concentration was therefore chosen for the subsequent quantitative work. The ionic strength, μ, of this solution is about the same as that of physiological saline according to the formula of Lewis and Randall (*12*) $\mu = \frac{1}{2}\sum m_1 \cdot Z_1^2$, where m_1 is the stoichiometric molality and Z_1 is the valency.

The mercury estimations

Sciatic nerves from two or three frogs (the number depending on the size of the nerve trunks) were immersed in the mercuric chloride solution for a known time. A low-angle X-ray diffraction pattern was recorded from a segment taken from the centre of one of the treated specimens, and all the nerves were washed carefully in normal saline, dried superficially on filter paper, and freeze-dried in an Edward's commercial freeze drier. When dry, the nerves were weighed, and the specimen, together with its weighing bottle, was placed in a digestion tube. After the addition of 1.0 ml nitric acid and 0.5 ml sulphuric acid, the tube was warmed gently until the specimen had dissolved. The digestion was continued until white fumes coming from the sulphuric acid indicated that all the nitric acid had been removed. The resulting solution was transferred to a volumetric flask and made up to volume with distilled water. It was arranged that the acidity of the solution thus obtained was approximately half normal.

Diphenylthiocarbazone (dithizone) was used as the colorimetric reagent for the estimation of mercury, and by a reversion procedure (*13*, *15*) independence from standard solutions was attained once the calibration curve had been obtained. This reversion technique involves the measurement of a change in the optical density arising from the breakdown of a mercury-dithizone complex by the addition of potassium iodide, and has many advantages over the titration methods. In particular, when this reversion procedure is used, trace elements (e.g. copper) do not affect the determination of mercury.

A measured volume of the aqueous solution containing mercuric ions was pipetted into a separating funnel and a known quantity of dithizone in chloroform was added. Standardisation of volumes was necessary in order to eliminate errors due to the solubility of the chloroform in the aqueous phase and to reduce the error due to variations in the areas of the reactive surfaces. The funnels were shaken mechanically

for one minute and after standing to allow separation of the layers, an aliquot of the chloroform containing the mercury-dithizone complex was run off into a centrifuge tube. About 3 ml of a solution of potassium iodide was added and the tube vigorously shaken to facilitate the reversion. Separation of the chloroform and water layers was effected by centrifugation, and the chloroform layer was pipetted into a 1 cm Beckmann absorption cell. The optical density of the dithizone solution both before and after reversion was measured in the Beckmann spectrophotometer. Under these conditions, the calibration curve for the mercury estimations proved to be linear between the limits 1 to 40 μg mercury. The rate of change of density with increasing quantities of mercury was 0.0155 per μg and the reproducibility between specimens was better than 1 μg.

–SH group blocking agents

Since mercuric ions were expected to react primarily with any available –SH groups, specific blocking agents for these groups were sought. Dinitrofluorobenzene (D.N.F.B.) has been used extensively for the chemical estimation of –SH groups, and despite the fact that this reagent will also react with $-NH_2$ and tyrosine groups (*1*) it was thought to be a suitable blocking agent for this investigation. The procedure adopted was to immerse the fresh nerve specimen in a saturated aqueous solution of the blocking agent (using 0.9% saline as the substrate) for a known period of time before immersing in the mercuric chloride solution. The X-ray diffraction patterns were recorded after each stage in the preparation, and the mercury content of the specimen was then estimated in exactly the same way as outlined above. Dinitrochlorobenzene (D.N.C.B.) and Iodoacetamide were used as alternative blocking agents. The Iodoacetamide was applied in concentrations of 0.1% and 0.5% in saline (made up to 1% with saline), and of 1% in distilled water.

Phosphorus determinations

The sulphuric acid digest obtained for the mercury estimations was also suitable for phosphorus determinations by the Fiske-Subbarow method (*10*). The total phosphorus value was taken as an index of the total phospholipid present in nerve and was used as an alternative reference to that of dried weight.

RESULTS

When frog sciatic nerve was immersed in the mercuric chloride solution a reproducible sequence of changes in the low-angle diffraction pattern of the myelin was observed. By halting the mercury treatment at different stages as established by the diffraction pattern, and estimating the mercury content of the nerve fibre at each

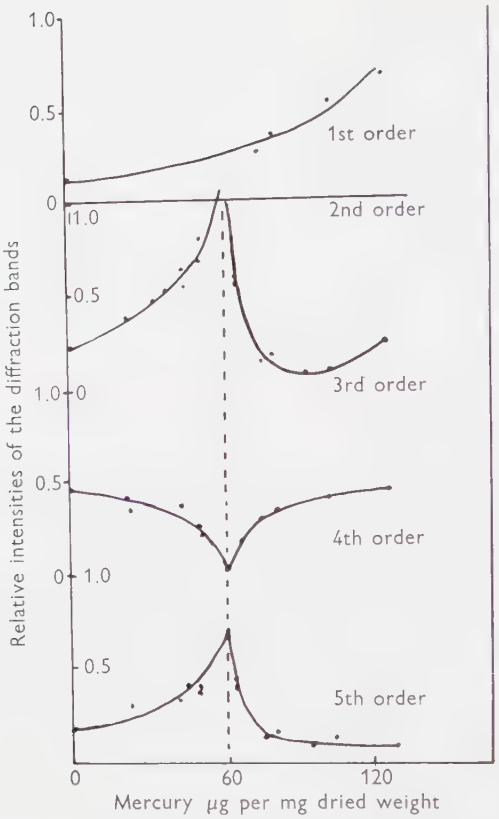

FIG. 1. Variations in the diffraction band intensities with increasing quantities of mercury.

stage, it was possible to refer the changes in the diffraction pattern of the myelin to the total mercury content of the nerve.

In order to express the intensity data, it was assumed on general observations that the intensity of the strong second order reflection was constant throughout the series, and the intensities of the other bands were referred to this. The results showing the values of the mercury content (in μg/mg dried weight) and the relative intensities of the bands of the associated diffraction patterns are shown graphically in Fig. 1. The early changes were most prominent in the third, fourth and fifth order reflections. The intensity of the third and fifth orders increased whilst that of the fourth order decreased rapidly. On prolonged immersion in the mercuric chloride solution the fourth order was found to pass through an intensity minimum and thereafter to

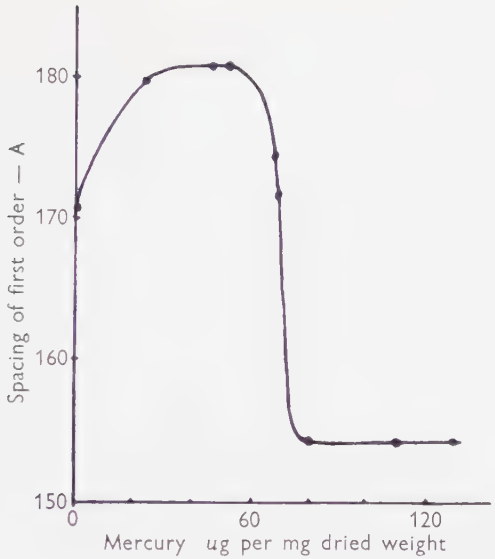

FIG. 2. Changes in the dimension of the fundamental repeating unit of the nerve myelin structure with increasing quantities of mercury.

increase again to almost its original intensity. The third and fifth order intensities passed through a maximum which coincided with the attainment of a minimum intensity of the fourth order. Beyond this point, the intensity of the third order decreased very rapidly with increasing mercury content, but subsequently increased again to a value close to its original intensity. The fifth order intensity also decreased rapidly and remained at a low level. Meanwhile, the first order reflection became progressively stronger than in the untreated specimens. The treatment with mercuric chloride also caused changes in the diffraction spacings. In Fig. 2, the change in the fundamental period is plotted against mercury content. Initially the increase in spacing was fairly rapid, but attained a semi-stable state at about 184 Å as the mercury content increased from 40 to 60 μg. Then followed a very rapid contraction to 154 Å and thereafter no further change of the spacings was observed. After 48 hours, structural changes became apparent in controls kept in normal Ringer's solution and therefore experiments continued beyond this time were considered unreliable.

There was an apparent time sequence in the uptake of mercury, but this varied from one supply of frogs to another and with the condition of the nerve. It can be noted, however, that in general 21 to 23 μg Hg/mg dried weight was taken up in the first two hours. The value had reached about 50 to 80 μg in 24 hours, and after immersion for 48 hours the maximum recorded value was 130 μg/mg dried weight.

TABLE I

Blocking agent and concentration	Time of immersion in blocking agent (hrs)	Time in $HgCl_2$ (hrs)	Mercury mg dried weight (μg)
D.N.F.B., saturated	24	24	25.8
	24	24	22.0
	24	24	31.0
	24	48	34.5
	24	48	27.8
	48	24	26.7
	48	48	29.2
D.N.C.B., saturated	24	24	33.3
	24	24	31.7
	24	24	31.0
	24	48	37.4
	24	48	41.0
	48	24	42.9
	48	48	36.0
Iodoacetamide, 1 %	24	24	36.5
0.5 %	24	24	26.0
0.5 %	24	24	27.2
0.5 %	24	48	35.0
0.1 %	24	24	44.4
0.1 %	24	48	50.0
Saline	24	24	52.4
	24	24	51.7
	24	24	52.4
	24	24	47.2
	24	48	38.0
	24	48	38.7
	24	48	28.5
	48	24	32.5

–SH group blocking agents

In further experiments, specimens were treated with different blocking agents prior to immersion in the mercuric chloride solution. The blocking agents themselves all modified the low-angle diffraction pattern and only small changes occurred on subsequent treatment with mercuric chloride. However, determinations of the mercury content showed that the pre-treatment with blocking agents had reduced the subsequent uptake of mercury. Typical results are shown in Table I. The uptake of mercury after preliminary treatment of the tissue with blocking agents was very rapid and a relatively constant mercury level was quickly attained.

Control experiments in which specimens were immersed in physiological saline for up to 48 hours before treatment with mercuric chloride showed that, although this pre-treatment did not affect the diffraction pattern, it did reduce appreciably the

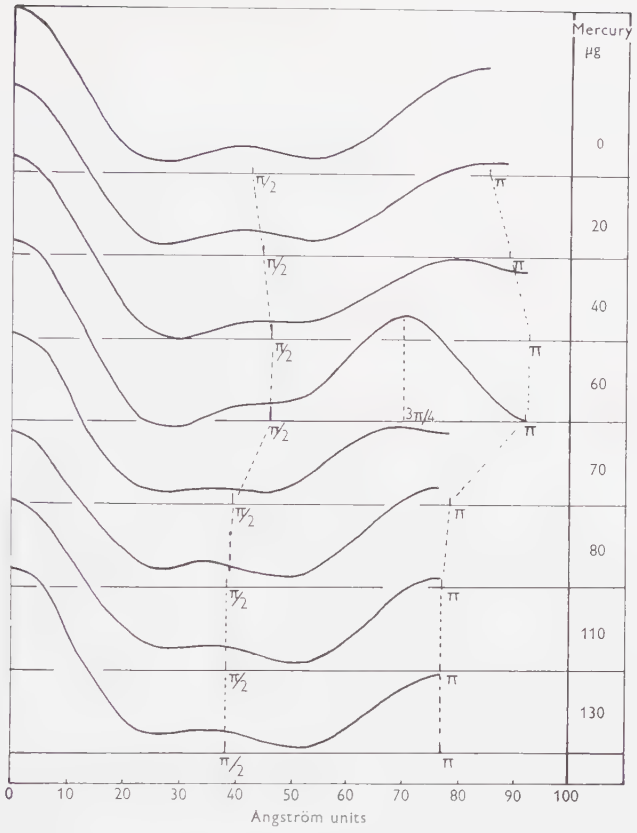

FIG. 3. Patterson functions calculated from intensity data at a succession of mercury levels and plotted against the dimension of the fundamental repeating unit.

subsequent uptake of mercuric chloride (Table I). Furthermore, although the subsequent treatment with mercuric chloride produced a change in the diffraction pattern similar to that already established for a mercury level of about 60 μg, the pattern of the relative intensities did not correspond to any of those used in the construction of Fig. 1.

TREATMENT OF RESULTS

The intensity data can be expressed directly as a one-dimensional Patterson synthesis using the equation $P = \sum (F_{00l})^2 \cdot \cos 2\pi \cdot lz$, where F, the structure amplitude, is proportional to the square root of the band intensity and l the diffraction order. Throughout the series of calculations it was assumed that the unit cell had a centre

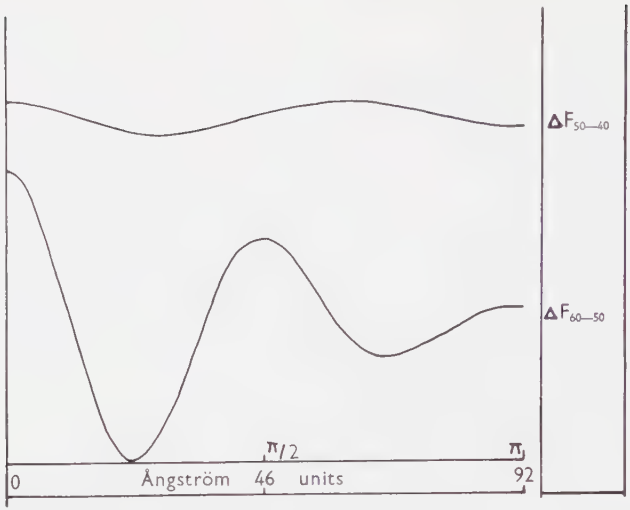

FIG. 4. Difference Patterson diagrams calculated for changes in mercury content of 40 to 50 and 50 to 60 μg Hg/mg dried weight.

of symmetry. Syntheses were made from the intensities at selected values of the mercury content taken from Fig. 1. The resulting Patterson diagrams are given in Fig. 3. In the preliminary stages of mercury treatment, the z vector prominent in the Patterson diagram derived from the fresh nerve diffraction pattern is gradually replaced by a strong vector at $3z/4$. In the region corresponding to an increase in mercury content from 60 μg to 70 μg there is a relatively abrupt change of emphasis back to a z vector, and this change coincides with a marked reduction in the fundamental repeating period. The peak at $3z$ 4 in the expanded (184 Å) structure represents a 70 Å vector whilst the most prominent vector (at z) in the contracted (174 Å) structure is at about 77 Å. A small peak at about $z/2$ is evident throughout the series.

The calculation of the electron density distribution ($\sum(\pm F_{00l}) \cdot \cos 2\pi \cdot lz$) through the structure requires a knowledge of the signs of the structure amplitudes. These signs cannot be deduced directly from the intensity data. However, the effects of introducing a heavy atom such as mercury into the structure may be used to facilitate a prediction of these signs. By taking Difference Patterson Functions it is possible to obtain a vector diagram due solely to the added mercury and from this to suggest positions at which mercury may be deposited. The Difference Patterson Function, ΔP, is given by the equation $\Delta P \quad \sum(\Delta F_{00l})^2 \cos 2\pi lz$, where ΔF is the difference in the amplitude of the reflection 00l before and after the addition of mercury to the structure. In order to avoid any uncertainties due to simultaneous changes in the size of the repeating unit, only those regions in which the spacings were relatively con-

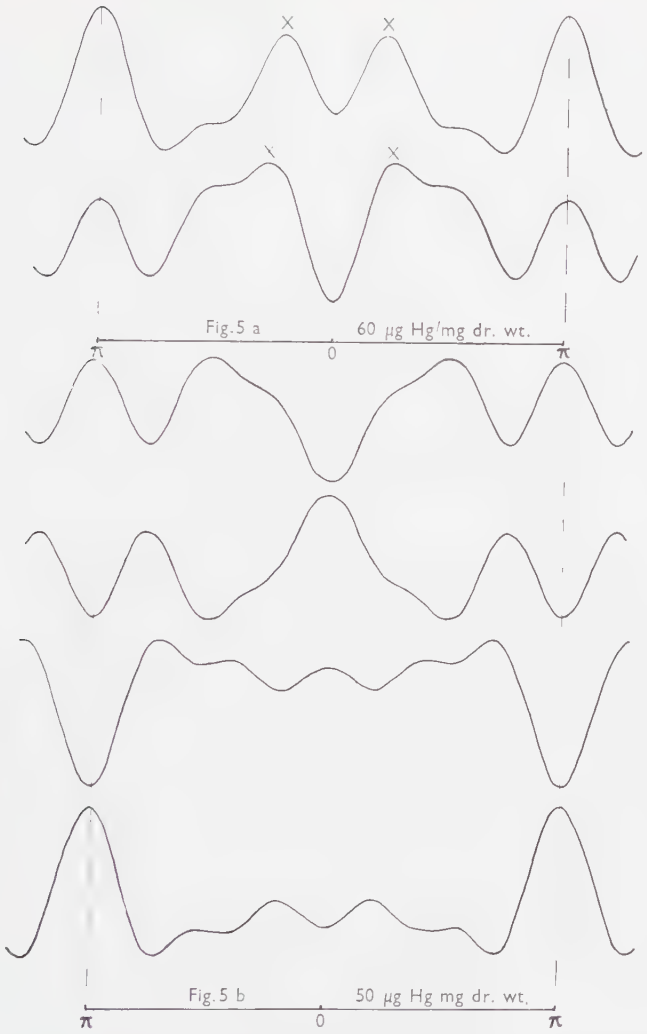

FIG. 5. *a*: Two alternative electron density distributions derived for the 60 μg level. (The peaks which may be involved in the contraction process are indicated by *X*.) *b*: Four alternative electron density distributions derived for the 50 μg level.

stant were considered. Changes in the diffraction intensities in the 80 to 130 μg region were relatively small, and therefore considerations in terms of Difference Patterson Functions were confined to the region corresponding to an increase in mercury content from 40 to 60 μg/mg dried tissue. This region was considered in two parts, and the resulting plots of the Difference Patterson Functions (ΔP_{50-40}

and ΔP_{60-50}) are shown in Fig. 4. (A relative magnification of two has been introduced in plotting the former in order to preserve its clarity.) The peak heights in the curve ΔP_{50-40} were very much smaller than those in the ΔP_{60-50} curve and therefore further detailed interpretation was carried out only in the case of the latter. The peaks at $\pi/2$ and π in this vector diagram could be accounted for in terms of two alternative types of arrangement of mercury deposits.

Assuming that the structure retains its centre of symmetry, interactions of suitable magnitudes at π 2 and π could be obtained either with a mercury deposit coinciding with the centre of symmetry or with the centre of symmetry placed midway between two such deposits. From a consideration of the effects these alternative arrangements would have on the diffraction intensities, the number of possible sign combinations for the five structure amplitudes was limited to six. The six corresponding Fourier plots showed some marked similarities which permitted a further reduction of the possible types of electron density distribution to four at the 50 μg Hg level and two at the 60 μg level. These remaining possibilities are shown in Fig. 5. The resolution of such plots can be no greater than about 30 Å.

DISCUSSION

In considering the effects of the mercuric chloride solution on the nerve structure, it is necessary to distinguish between specific ion effects and general osmotic effects. A previous study (*9*) of the effects on the myelin diffraction pattern of immersion media (saline and Ringer's) at different concentrations showed no appreciable changes between 0.5 and 2.0%. Thus, since the saline concentration was within this range throughout the present experimental series, changes in the diffraction patterns were considered to be due specifically to the presence of the mercuric ion.

Mercuric ions have a strong affinity for sulphydril groups, and the fact that the uptake of mercuric ions was appreciably reduced by the preliminary application of –SH blocking agents indicates that such groups are involved in the interactions. However, the interpretation is complicated by the observations that pre-treatment of the nerve preparation for comparable periods of time with saline also reduced the subsequent uptake of mercury. It should also be noted that the chemical data applies to the nerve fibre as a whole, and no direct conclusions concerning the mercury content of the myelin can be derived. Thus no quantitative significance can be attached to the mercury values as used in Figs. 1 and 2 to relate to the properties of the myelin. In order to establish any quantitative relationship it would be necessary to determine the mercury content of the myelin component alone, possibly by applying the X-ray absorption technique.

Nevertheless, even though the estimations of mercury were made on whole nerve, the fact that the diffraction pattern from the myelin showed progressive changes as the mercury content of the tissue increased indicates a direct correlation between these diffraction changes and the amount of mercury in the myelin. The consistency of the phosphorus estimations is against the possibility that the variations in the mercury content may have been due to gross changes in the myelin content.

The most striking feature of the results as shown in Fig. 1 is the rapidity of the changes in the diffraction intensities in the region of 60 μg Hg/mg dried weight. Such abrupt changes would not be expected from the gradual increase in the mercury content and are probably related to the rapid shrinkage of the diffraction unit which takes place at about the same stage (Fig. 2). These rapid changes are featured in the Patterson analysis as a replacement of the $3\pi/4$ vector prominent before contraction by a vector at π. It would seem that the $3\pi/4$ vector is either eliminated or that it expands slightly (about 7 Å) and eventually contributes to the new π vector. Such an expansion might be of great significance when considered in relation to the overall contraction of the structure.

The fact that the vectors prominent in the Patterson synthesis from the mercury treated specimen differ from the mercury-mercury vectors as shown in the corresponding Difference Patterson Function, ΔP_{60-50}, indicates that the electron dense regions associated with the normal structural components still make a major contribution to the diffraction pattern even after the addition of mercury. Thus the $3\pi/4$ vector arises from interactions between mercury deposits and the normal myelin components.

The resolution of the electron density distribution diagram obtained would be sufficient only to define very broad structural features, so that the reduction of the number of curves for final consideration by neglecting small variations in shape is justifiable. The two remaining curve shapes for consideration at 60 μg mercury level are in fact inversely related. Such a result would be anticipated from the well-known principle (Babinet's Principle) that diffraction does not distinguish between two inversely related structures. Therefore in the absence of any additional evidence the real structure cannot be established. Similarly among the four curves deduced from the 50 μg level, two inversely related pairs can be recognised. Comparison with the 60 μg level does not lead to the elimination of any of these possibilities. From earlier discussion of the Difference Patterson Functions, the addition of mercury would be expected to have only a small effect on the electron density distribution, but comparison of the two sets of curves shows that this criterion may be satisfied in every case.

Despite the inability to find a unique solution, it is possible to comment on the contraction phenomenon in terms of the electron density distribution assuming that

the structure just prior to contraction is represented by one of the electron density distributions shown in Fig. 5*a*. It would appear that an expansion of the main vector by 7 Å during the general contraction of the structure could be achieved by the elimination of a trough, thereby producing a fusion of two major peaks (*X*, *X*) which could provide a new centre of electron density. If the rest of the structure is relatively unaffected by the contraction then interactions with the new peak will be at greater distances than they were with the two separate peaks (*X*, *X*). It would seem likely that mercury added at this stage would be located at the site of contraction.

The implications of the electron density distributions in terms of the molecular components will be considered together with other relevant data in a further paper.

ACKNOWLEDGEMENTS

We wish to thank Dr. P. J. Black, Department of Physics, for helpful discussion, and Professor A. C. Frazer for his continued interest in this work.

REFERENCES

1. Bowyer, F., *Nature* **174**, 355 (1954).
2. Fernández-Morán, H., *Exptl. Cell Research* **1**, 309 (1950).
3. —— *Progr. Biophys. and Biophys. Chem.* **4**, 112 (1954).
4. Fernández-Morán, H. and Finean, J. B., *J. Biophys. Biochem. Cytol.* **3**, 725 (1957).
5. Finean, J. B., *J. Sci. Instr.* **30**, 60 (1953).
6. —— Biochemical Problems of Lipids, *2nd Intern. Conf., Ghent*, 1955, p. 127. Butterworth, London.
7. —— *J. Sci. Instr.* **33**, 161 (1956).
8. —— *Acta Neurol. et Psychiat. Belg.* **5**, 462 (1957).
9. Finean, J. B. and Millington, P. F., *J. Biophys. Biochem. Cytol.* **3**, 89 (1957).
10. Fiske, Ch. and Subbarow, Y., *J. Biol. Chem.* **66**, 375 (1925).
11. Geren, B. B., *Exptl. Cell Research* **7**, 558 (1954).
12. Lewis, G. N. and Randall, M., *J. Am. Chem. Soc.* **43**, 1112 (1921).
13. Millington, P. F., M.Sc. thesis. Birmingham, 1957.
14. Robertson, J. D., *J. Biophys. Biochem. Cytol.* **1**, 271 (1955).
15. Rowles, S. L., Thesis. St. Catherine's Soc., Oxford, 1947.
16. Schmidt, W. J., *Z. Zellforsch. u. mikroskop. Anat.* **23**, 657 (1936).
17. —— *Z. wiss. Mikroskop.* **54**, 159 (1937).
18. Schmitt, F. O. and Bear, R. S., *J. Cellular Comp. Physiol.* **9**, 261 (1937).
19. —— *Biol. Revs. Cambridge Phil. Soc.* **14**, 27 (1939).
20. Schmitt, F. O., Bear, R. S. and Clark, G. L., *Radiology* **25**, 131 (1935).
21. Sjöstrand, F. S., *Experientia* **11**, 68 (1953).

The Structure and Development of a Polyhedral Virus Affecting the Moth Larva, *Pterolocera amplicornis*

M. F. Day, J. L. Farrant and Coralie Potter

Division of Entomology, Commonwealth Scientific and Industrial Research Organization, Canberra (M.F.D.), and Division of Chemical Physics, C.S.I.R.O. Chemical Research Laboratories, Melbourne (J.L.F. and C.P.)

Received August 5, 1958

Thin sections of nuclei of the larvae of the pasture caterpillar *Pterolocera amplicornis* infected with a polyhedral virus disease have revealed details of the structure of the virus and of some of its developmental stages. Virus multiplication occurs in the chromatin and the virus is released into the nucleoplasm as rods. These acquire membranes singly or in groups of up to 8 and membrane-covered rods become enclosed within polyhedra. These are shown to be protein crystals composed of approximately isometric molecules 71 Å in diameter probably arranged in a face-centred cubic lattice.

In 1953, the results of an initial study of a nuclear polyhedral virus disease affecting a pasture caterpillar *Pterolocera amplicornis* Walker were published by Day *et al.* (*6*). Thick and thin rods and also spheres were described, but no conclusion concerning the relation of these to the development of the virus could be reached. Thin sections of infected nuclei and of polyhedra have now provided further information about the virus and some of these data have already been presented in abstract form (*7*). They indicate that this virus is a particularly suitable object for the study of the virus and its development, and further details of these are presented in this paper.

METHODS

Small pieces of fat body were dissected from virus infected larvae and fixed by immersion for 4 hours in 1% solution of osmium tetroxide in acetate-veronal buffer at pH 7.4, as recommended by Palade (*16*). In later work, Rhodin's (*17*) fixative was used and gave results very similar to those with Palade's fixative. The tissue fragments were then washed in distilled water, and dehydrated by passage through graded dilutions of ethyl alcohol. They were embedded in butyl methacrylate containing 10% of the methyl ester (*15*).

Sections were cut with glass knives (*13*) with a microtome of the type described by Hodge, Huxley and Spiro (*9*). Even though the hardness of the plastic was increased by the addition

of the methyl ester the cutting of thin sections was made difficult by the hardness of the polyhedra, which frequently shattered on the side first impacted by the knife. However, the thicker sections not only showed the full length of greater numbers of virus rods, but also exhibited the enclosing membranes with better contrast than did the thinner sections.

A modified RCA EMU–1 electron microscope was used.

OBSERVATIONS

Rods present in all recently infected nuclei are interpreted as those of the virus. Many of these rods have been cut during sectioning, but their maximum length is 3000 Å and their diameter is about 300 Å. The discrepancies in measurements between these measurements and those given by Day *et al.* (*6*) are due partly to the adherence of extraneous material to the rods illustrated in the earlier paper.

These rods are generally found also in later stages of infection (Figs. 1–8). Their form and dimensions are the same whether they are found attached to the chromatin mass or in mature polyhedra. The rods are particularly abundant within the chromatin mass and multiply there (Figs. 1 and 2). Where they occur peripherally (Figs. 3 and 4) they appear to be attached to peripheral chromatin. We cannot be certain of details of the actual process of viral multiplication in spite of careful search in the relevant parts of infected nuclei. The virus rods at this stage appear to be flexuous (Figs. 4 and 6). There is evidence that the osmium-fixed virus rods sometimes contain an axial concentration of dense material (Fig. 11), but this is not established unequivocally. There is also some indication that they may be hexagonal in cross-section (see Figs. 6 and 7).

The virus rods break away from the chromatin mass and the majority of those free in the nucleoplasm are enclosed within membranes (Figs. 5 and 6). These membranes are ovoid in shape and contain little osmiophilic material other than the rods. Membranes cut in cross-section are approximately 100 Å thick. They average 3500 Å in length and 2000 Å in width, but these measurements are rather variable. The membranes show clearly in many instances the number of virus particles enclosed

---

FIG. 1. Portions of 2 nuclei are shown with cell wall between them. The enlarged nuclei occupy almost the entire cytoplasm. Virus rods are abundant within residual chromatin mass in the centre of the nucleus on the right. A few virus rods are enclosed within membranes in the surrounding nucleoplasm (labelled *A*). Incipient polyhedron formation can be seen at *B*. × 15,000.

FIG. 2. A later stage than Fig. 1. Polyhedron formation well advanced and most chromatin has disappeared. Virus multiplication is continuing in isolated pieces of residual chromatin and it is suggested that the rods are in the process of becoming enclosed within membranes at the points marked with arrows. × 14,500.

FIGS. 1–11. Electron micrographs of thin sections of nuclei of larvae of *Pterolocera amplicornis* infected with polyhedral virus.

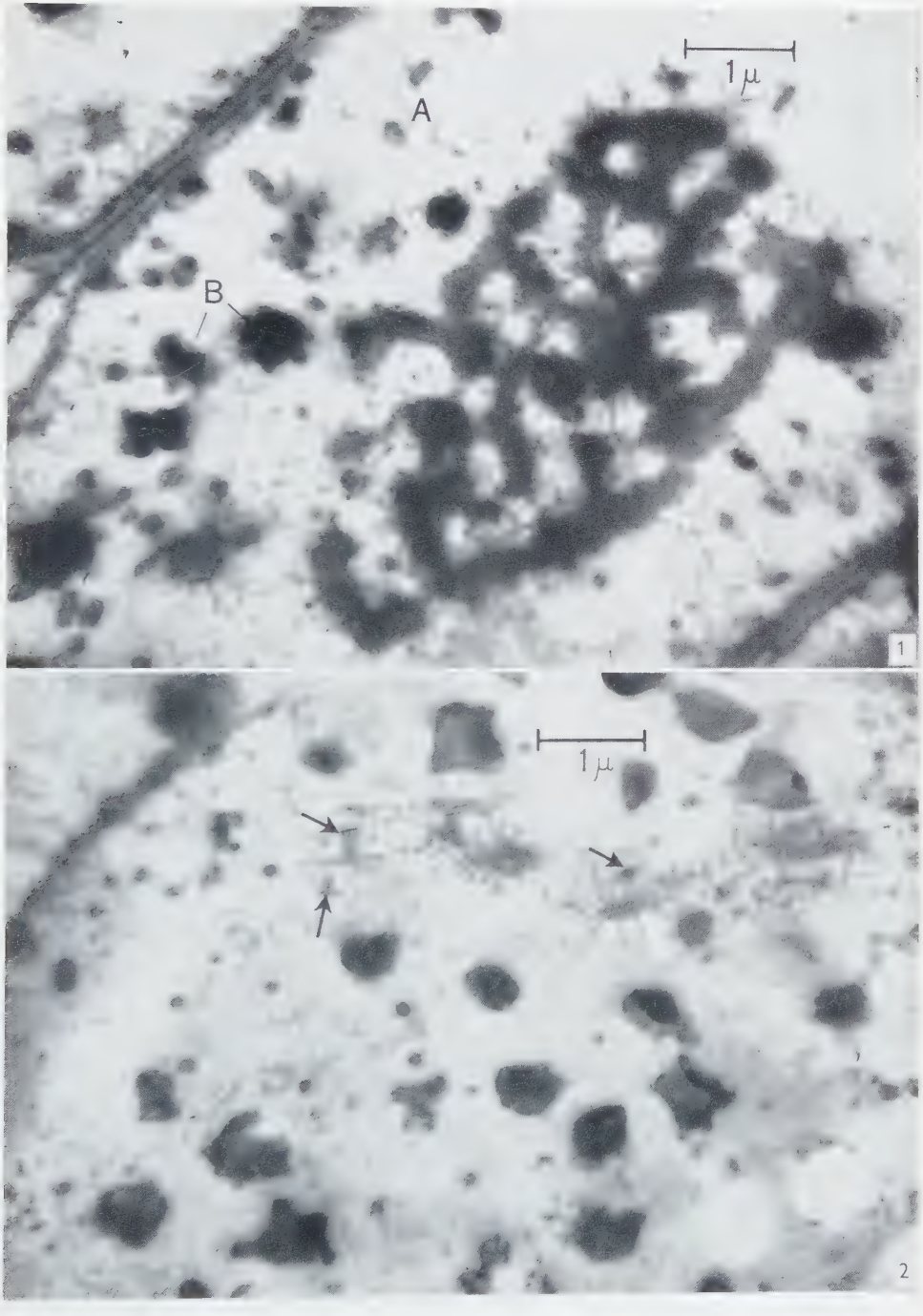
1 μ
A
B
1
1 μ
2

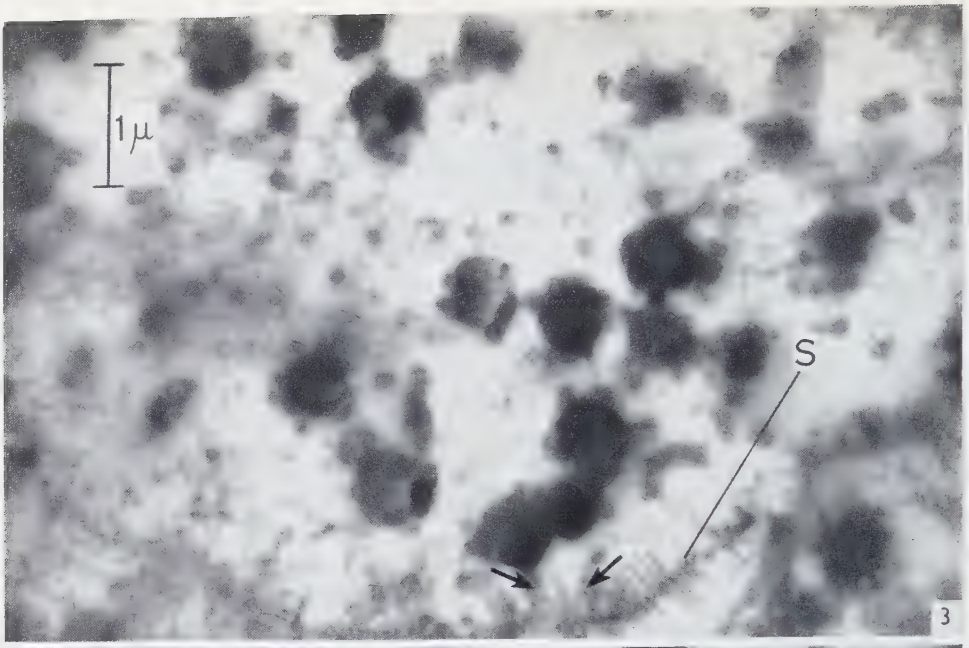

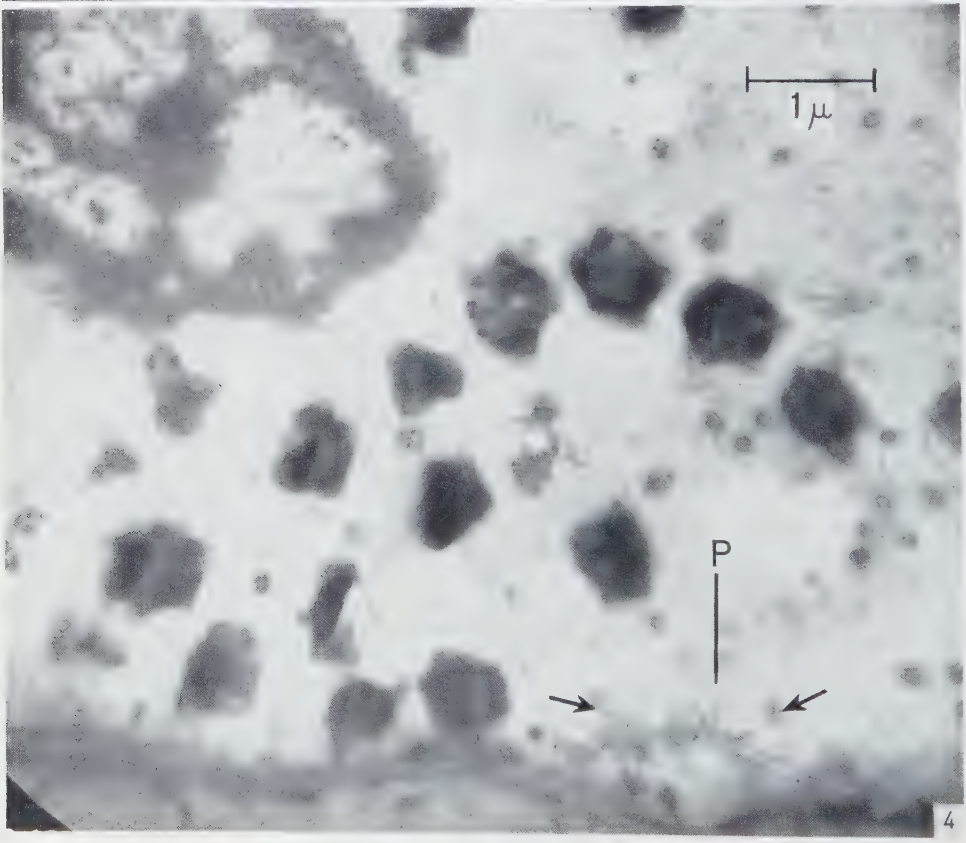

FIG. 3. Same stage as Fig. 2. Virus rod formation at *S* and membrane formation occurring at the points marked with arrows. Some spherical, apparently empty membranes present in the nucleoplasm. At several points, membranes enclosing virus rods are sectioned transversely showing clearly the number of rods within the membranes. ×16,000.

FIG. 4. Section of a nucleus showing virus synthesis in residual chromatin and peripherally at *P*. Suggested membrane formation in progress at points marked with arrows. ×16,000.

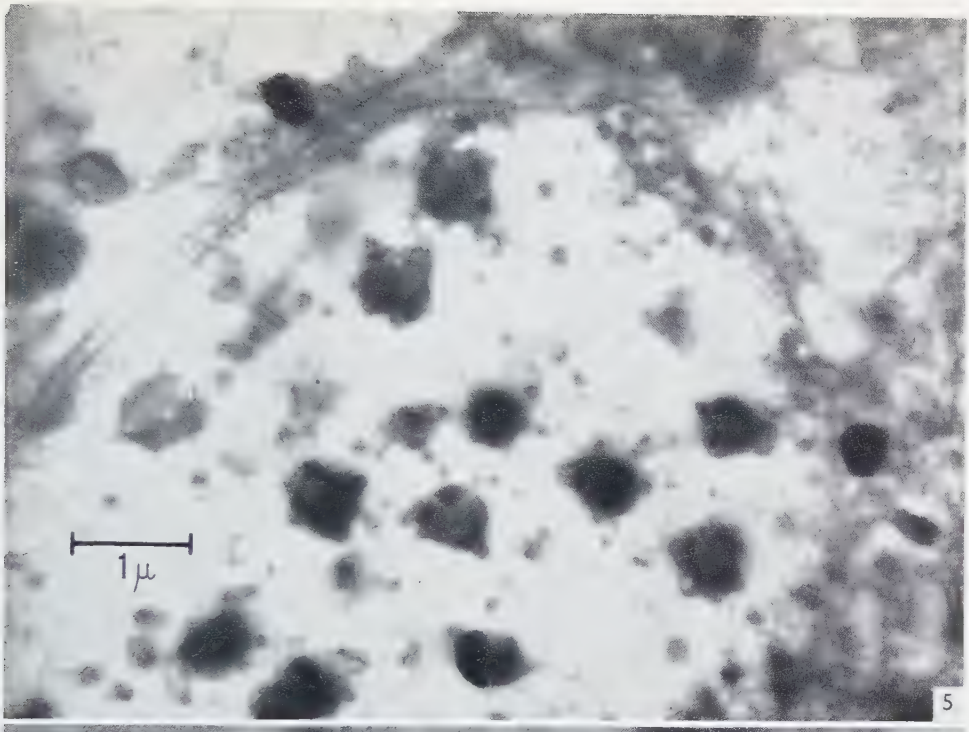

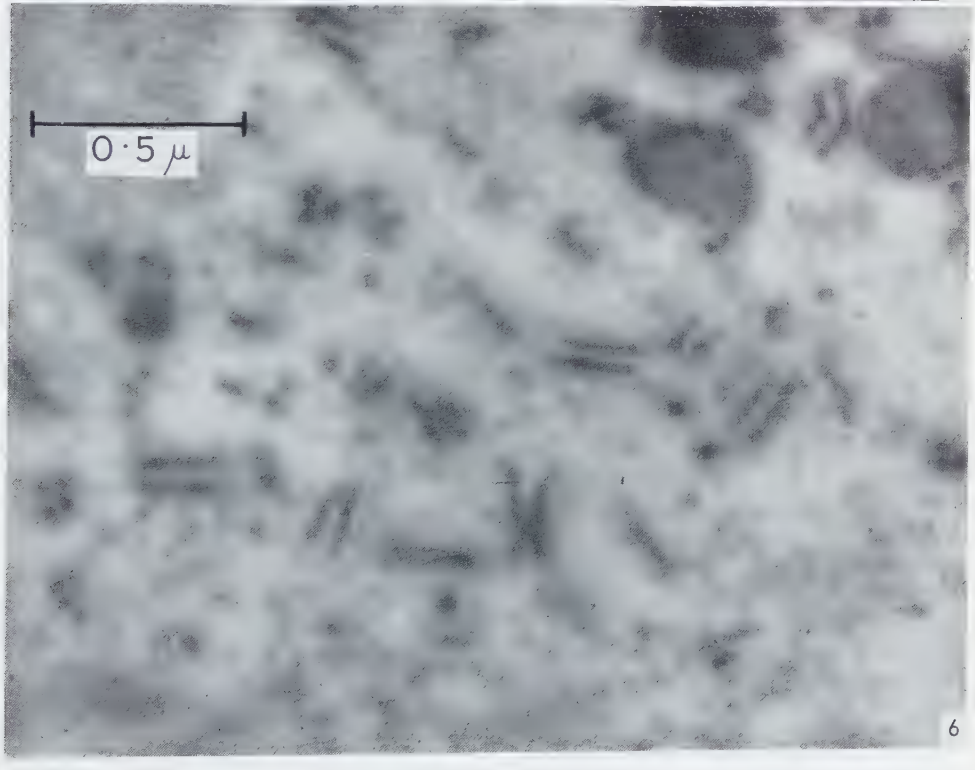

FIG. 5. Later stage in infection. Polyhedron formation well advanced, but most polyhedra still have projections where virus membranes are being incorporated within polyhedra. Very few virus rods not enclosed within membranes. Some empty spherical membranes present. Cytoplasm is necrotic. ×15,000.

FIG. 6. Section of nucleus at higher magnification showing virus rods mostly enclosed within membranes and cut in longitudinal section. Three polyhedra in process of formation at top right. 54,000.

TABLE I

NUMBERS OF VIRUS RODS CONTAINED WITHIN 205 MEMBRANES

No. of rods	1	2	3	4	5	6	7	8
No. of membranes	36	45	58	44	16	3	2	1

within them. Table I shows the frequency of membranes containing increasing numbers of rods. Membranes are frequently laid down initially around aggregates of rods. The frequencies suggest that virus multiplication does not occur within the membranes. We have not found more than 8 rods within a membrane, and numbers in excess of 5 occur infrequently.

The details of the initial formation of the membranes around the virus particles is in doubt, but it is tempting to interpret the images marked with arrows in Figs. 2–4 as stages in this process. These micrographs suggest that the membranes are laid down around the rods shortly after the virus escapes from the chromatin network.

Circular objects averaging 1400 Å in diameter, which may be sections of the spherical bodies described in our earlier paper, may be seen in Figs. 5 and 8. It seems possible that these represent the membranes from which viral rods have emerged, for the membranes surrounding rods are clearly flexible and would probably assume a spherical form if they were not stretched by the presence of enclosed virus rods. The wide range of diameters observed in Figs. 1–3 and 8 may reflect the differing numbers of virus rods originally enclosed within the membranes. Thus, it may be that the presence of many empty membranes indicates that the virus undergoes a second (or subsequent) cycle of multiplication within a single nucleus. This hypothesis obtains some support from the observation that there is an inverse relationship between the presence of empty membranes and the amount of residual chromatin (see Figs. 1, 3, 5 and 8 in that sequence).

Alternatively the evidence can be interpreted as supporting the view that open membranes may form separately and then most, but not all of them, capture rods which would be subject to rapid Brownian movement. This possibility is suggested by Xeros' conclusions concerning membrane formation in a nuclear polyhedrosis of *Lymantria dispar* (*18*).

FIG. 7. Same stage but majority of virus particles cut in transverse sections. Section shows arrangement of groups within membranes and arrangement of membranes within developing polyhedra. × 50,000.

FIG. 8. Late stage in polyhedron formation. Nucleoplasm and cytoplasm largely destroyed and polyhedra generally with virus membranes completely enclosed. Some empty spherical membranes present in nucleoplasm. × 13,500.

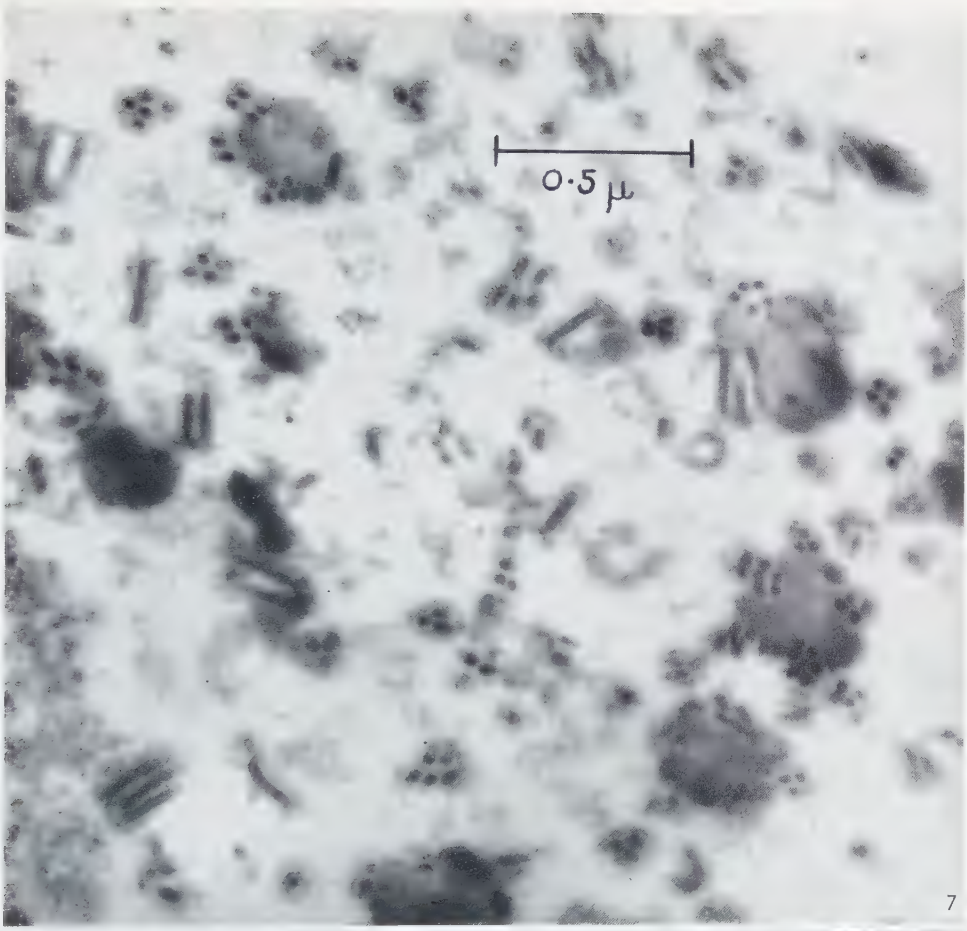

7

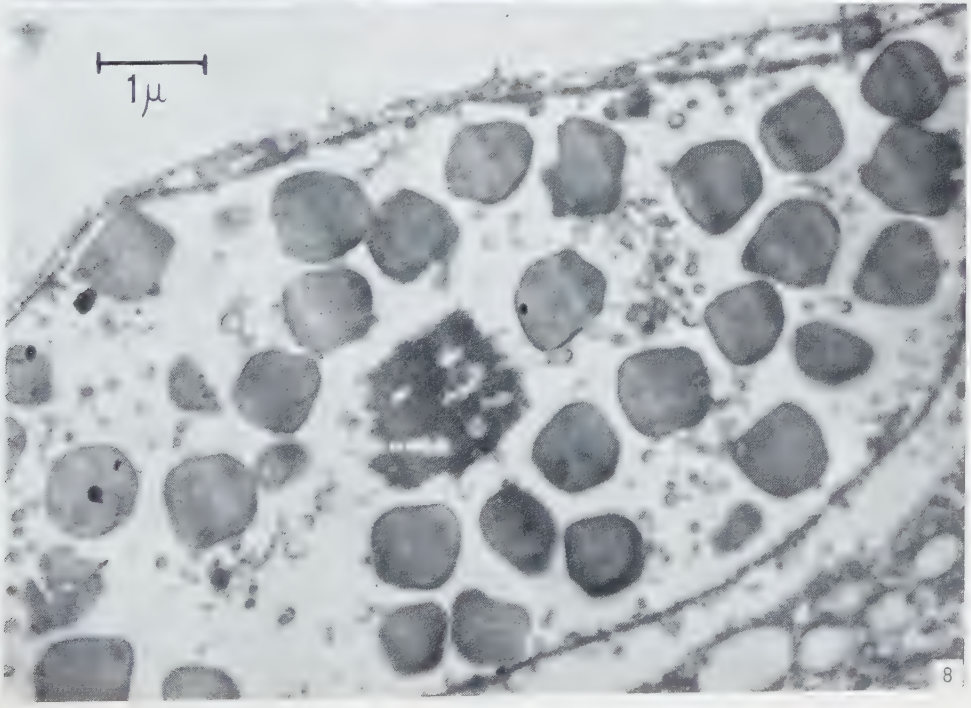

8

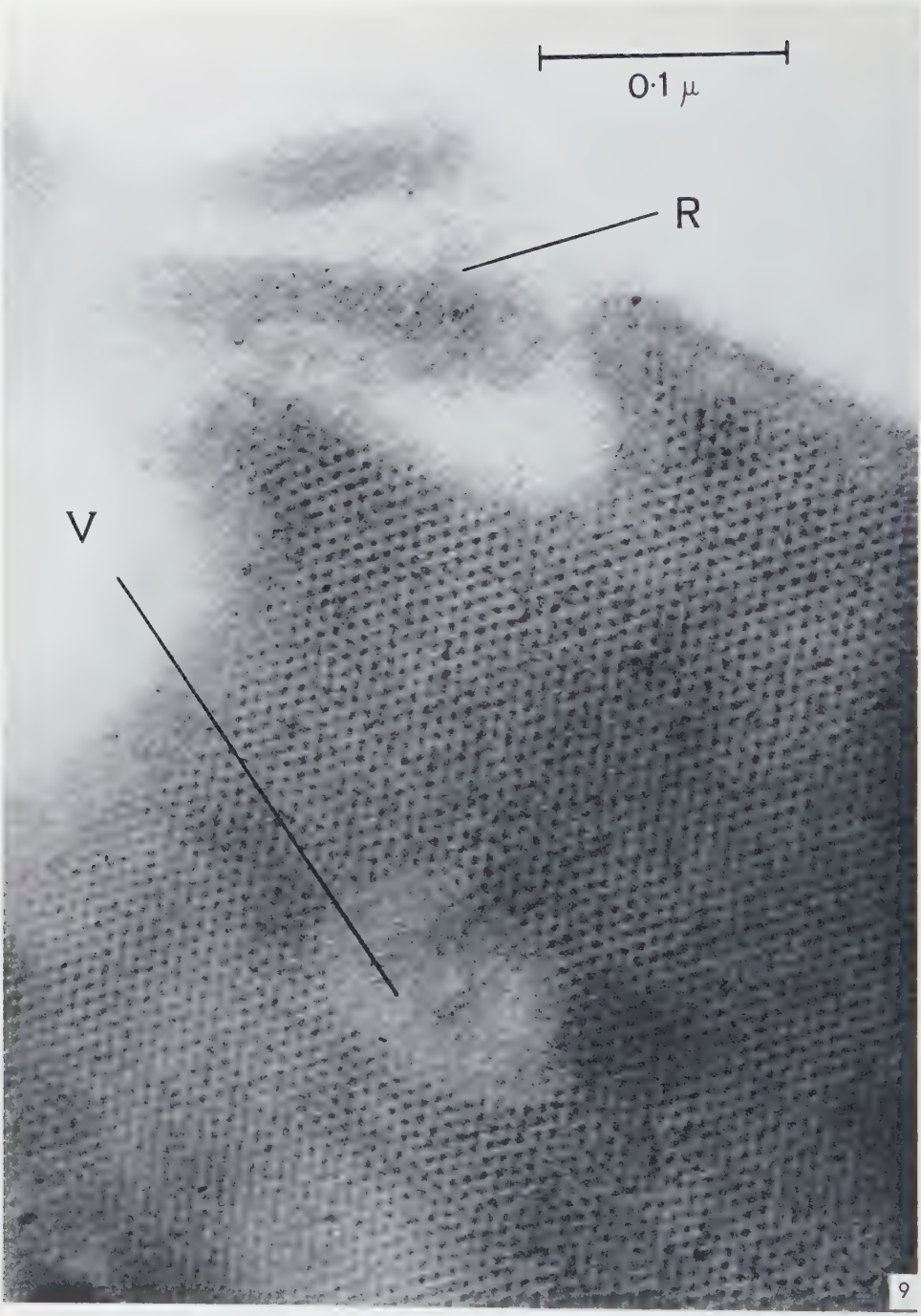

FIG. 9. High magnification section of part of single polyhedron, showing a virus rod (*R*) being incorporated within it. It is possible that the position of the rod has been altered during sectioning. The crystalline lattice of the polyhedron is clearly discernible. It is not disturbed over a distance of about 1000 Å by the presence of an enclosed virus particle at *V*. The thinness of the section has made it impossible to differentiate the virus rod at *V*, or the membrane of the virus rod at *R*. × 330,000.

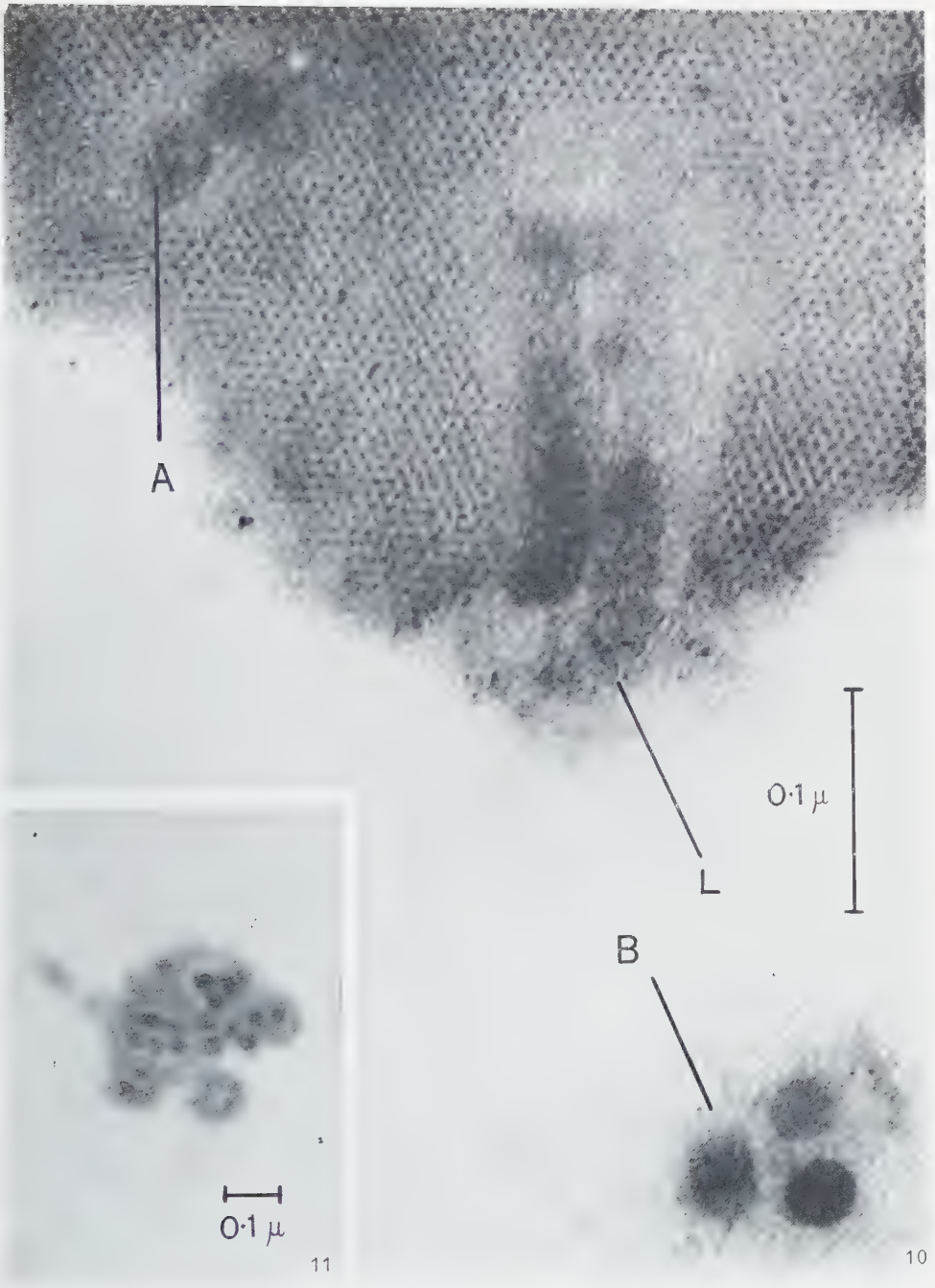

FIG. 10. Section of part of polyhedron surrounding nucleoplasm at high magnification, showing enclosed virus rods at *A*, two rods in process of incorporation at *L*, and a section of a membrane containing 3 virus rods at *B*. × 300,000.
FIG. 11. Section of groups of virus rods showing indication of osmiophilic central cores in some rods × 75,000.

The initial stages of polyhedron formation have not been identified with certainty, because examples which may appear to illustrate this may result from the sectioning of the edge of a mature polyhedron. The polyhedra do not form within the chromatin. They appear in the nuclear sap as the crystallization of a specific protein and regular patterns (Figs. 9 and 10) ranging from almost hexagonal (Fig. 9) to almost square have been observed in the sections. It appears that the molecules are approximately isometric, 71 Å in diameter and probably they are arranged close-packed in a face-centred cubic lattice. Swelling and distortion of the crystals during embedding and sectioning render this conclusion somewhat uncertain. Virus rods within membranes appear to act as foci of crystallization and unencapsulated rods are not observed in the polyhedra. Virus rods enclosed within membranes are randomly incorporated within the crystallizing polyhedral protein, as is shown in Figs. 2, 3, 5 and 6. It is an observation of some interest that the regularity of the crystalline array is not disturbed by these inclusions over distances of roughly 1000 Å (Fig. 9; *14*).

DISCUSSION

Many details of the infection and maturation of polyhedral viruses remain obscure. A number of previously published observations on a variety of polyhedral diseases agree in many respects although some of the interpretations are at variance with one another. It should be appreciated that no infectivity data are available for any of the various stages of development of the virus, but the evidence for the arrangement of some of the stages in sequence is reasonably good. Thus, sections of polyhedra give no evidence of any maturation or development of the virus within the polyhedron.

Virus rods enclosed within membranes are incorporated in the crystalline polyhedra and emerge in the same form after dissolution of the mature polyhedra. Also, virus multiplication takes place in the rod stage and the acquisition of membranes occurs subsequently. Only those membranes containing virus rods become enclosed within polyhedra. These observations suggest a working hypothesis of viral development which seems worthwhile formalizing in diagrammatic fashion (Fig. 12) even though it is appreciated that many additional features of polyhedral virus multiplication are not included.

Fig. 12 illustrates the cycle of virus development as it appears from the work of Bergold (*1*), Bird (*2*, *3*) and Hughes (*10*) and from the data presented above. Xeros (*18*, *19*) has been mainly concerned with the early stages of virus multiplication, but the present study has contributed nothing new concerning this process.

After infecting a susceptible nucleus it is possible that the virus rod breaks up prior to its entry into the synthetic mechanisms of the cell. Such a stage would be equivalent to the "dark phase" of viruses affecting plants, vertebrates and bacteria

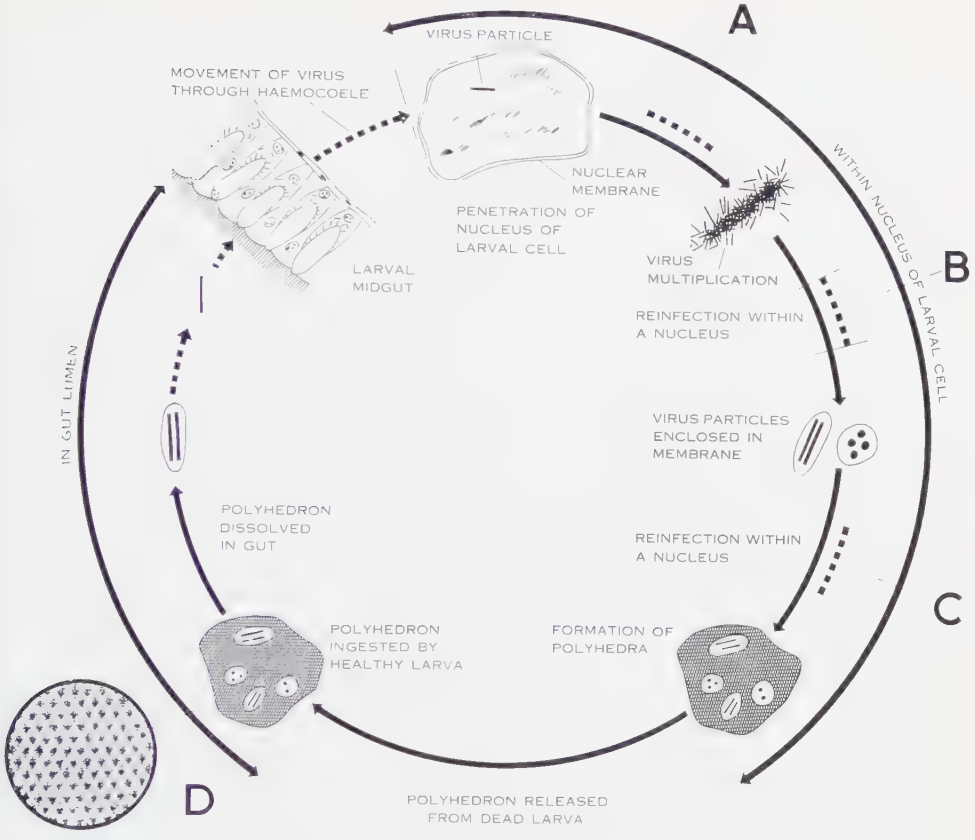

FIG. 12. Diagram of stages in development of polyhedral virus. Broken lines indicate hypothetical parts of the cycle. For description, see text.

and is suggested by the work of Krieg (*12*). The stage is represented by the dotted alternative *A* in the diagram. Following virus synthesis there may be subsequent cycles of virus reproduction as indicated at *B*. Alternatively, or perhaps in addition, subsequent cycles of multiplication may occur after the virus rods acquire their membranes. The inclusion of such a stage at *C* would possibly explain the presence of many empty membranes in infected nuclei containing many polyhedra. The inset at *D* illustrates diagrammatically the crystalline lattice of the mature polyhedron. We have no method for determining whether infection in the gut lumen occurs in the form of isolated rods or of rods within membranes, but the sequence illustrated represents our current working hypothesis. Further information on these details is being sought in infections of insect tissue cultures.

This polyhedrosis exhibits two possible parallels with two other virus diseases. Firstly Bloch *et al.* (*4*) have found that adenovirus growing in the nuclei of HeLa cells appears to develop from a "reticulated dense granular matrix" and it seems that this may be analogous to the "chromatin mass or network" in which our virus rods first appear. In the HeLa cells the matrix is initially Feulgen negative as is the case with the chromatic mass or net of several nuclear polyhedroses studied by Xeros (*18*). Xeros (*19*) has proposed the term "virogenic stroma" to replace the terms chromatin mass and chromatin network. Secondly, several instances (Fig. 11) where the rods show evidence of dense axial material suggests that they may consist of hollow protein rods possibly with DNA near the axis just as tobacco mosaic virus consists of hollow protein rods with RNA near the axis (*5*, *8*, *11*).

Our thanks are due to Dr. N. Xeros for several discussions and for showing us his unpublished work on insect viruses.

REFERENCES

1. Bergold, G. H., *Can. J. Research E* **28**, 5 (1950).
2. Bird, F. T., *Biochim. et Biophys. Acta* **8**, 360 (1952).
3. —— *Virology* **3**, 237 (1957).
4. Bloch, D. P., Morgan, C., Godman, G. C., Howe, C. and Rose, H. M., *J. Biophys. Biochem. Cytol.* **3**, 1 (1957).
5. Caspar, D. L. B., *Nature* **177**, 928 (1956).
6. Day, M. F., Common, I. F. B., Farrant, J. L. and Potter, C., *Australian J. Biol. Sci.* **6**, 574 (1953).
7. Day, M. F., Farrant, J. L. and Potter, C., *J. Appl. Phys.* **26**, 1396 (1956).
8. Franklin, R. E., *Nature* **177**, 928 (1926).
9. Hodge, A. J., Huxley, H. E. and Spiro, D., *J. Histochem. and Cytochem.* **2**, 54 (1954).
10. Hughes, K. M., *Hilgardia* **22**, 391 (1953).
11. Huxley, H. E., *Proc. Stockholm Conf. Electron Microscopy*, 1956, p. 260. Almqvist & Wiksell, Stockholm, and Academic Press Inc., New York, 1957.
12. Krieg, A., *Z. Naturforsch.* **13 b**, 27 (1958).
13. Latta, H. and Hartmann, J. F., *Proc. Soc. Exptl. Biol. Med.* **74**, 436 (1950).
14. Morgan, C., Bergold, G. H., Moore, D. H. and Rose, H. M., *J. Biophys. Biochem. Cytol.* **1**, 187 (1955).
15. Newman, S. B., Borysko, E. and Swerdlow, M., *J. Research Natl. Bur. Standards* **43**, 183 (1949).
16. Palade, G. E., *J. Exptl. Med.* **95**, 285 (1952).
17. Rhodin, J., Correlation of Ultrastructural Organization and Function in Normal and Experimentally Changed Proximal Convoluted Tubule Cells of the Mouse Kidney. Thesis. Stockholm, 1954.
18. Xeros, N., *Nature* **175**, 588 (1955).
19. —— *ibid.* **178**, 412 (1956).

The Origin and Structure of Brochosomes

M. F. Day and Margaret Briggs

C.S.I.R.O. Division of Entomology and John Curtin School of Medical Research, Australian National University, Canberra, A.C.T.

Received August 11, 1958

Minute regular bodies found associated with insects and called brochosomes by previous investigators have been shown to be identical with bodies that originate in the malpighian tubules of leafhoppers. The bodies, which are regular dodecahedra with projections from each corner, are formed within the cytoplasm of the malpighian tubule cells, but their composition and their function are obscure.

In a series of papers, Tulloch, Cochrane and their collaborators (*5–8*) have recorded the presence of remarkable minute bodies (which they have called "brochosomes") on the wings of many species of insects from many parts of the world. These bodies were particularly associated with leafhoppers, but were occasionally found on certain other insects. No clue to their origin was obtained, but a series of presumptive developmental stages was described (*5*), and their occasional occurrence within the body cavity of leafhoppers was reported.

The fact that "brochosomes" were mainly found on the wings of leafhoppers suggested to us that they were excretory products, for Storey and Nichols (*4*) had described in some detail the extraordinary habit of the leafhopper, *Cicadulina mbila*, of picking up on the hind legs a drop of excreta and smearing it over the wings. This behaviour has been confirmed with other species of leafhoppers (*2*). Storey and Nichols (*4*) suggested that those droplets which were picked up by the legs (as distinct from the much more frequent clear droplets ejected as "honey dew") contained some of the contents of the malpighian tubules.

The uncontaminated malpighian tubules of four species of leafhoppers (*Orosius argentatus* (Evans), *Cicadulina bimaculata* (Evans), *Austroagallia torrida* (Evans), *Eurymeloides* sp.) were placed directly on collodion coated screens and examined in the electron microscope (Type RCA EMU-3B). Brochosomes were found present in large numbers on all screens (Fig. 1 *A*). We thus demonstrated not only the site of origin of the brochosomes, but also that the suggestion of Storey and Nichols (*4*) is correct, namely that the substances smeared on the wings contained materials from the malpighian tubules.

FIG. 1. *A*: Brochosomes from the malpighian tubules of *A. torrida*. Outer membrane surrounding brochosome is visible. *B–E*: Model of brochosome, photographed from four positions. Note similarity to many of the brochosomes, especially the smaller ones. × 25,000 (Fig. 1 *A*).

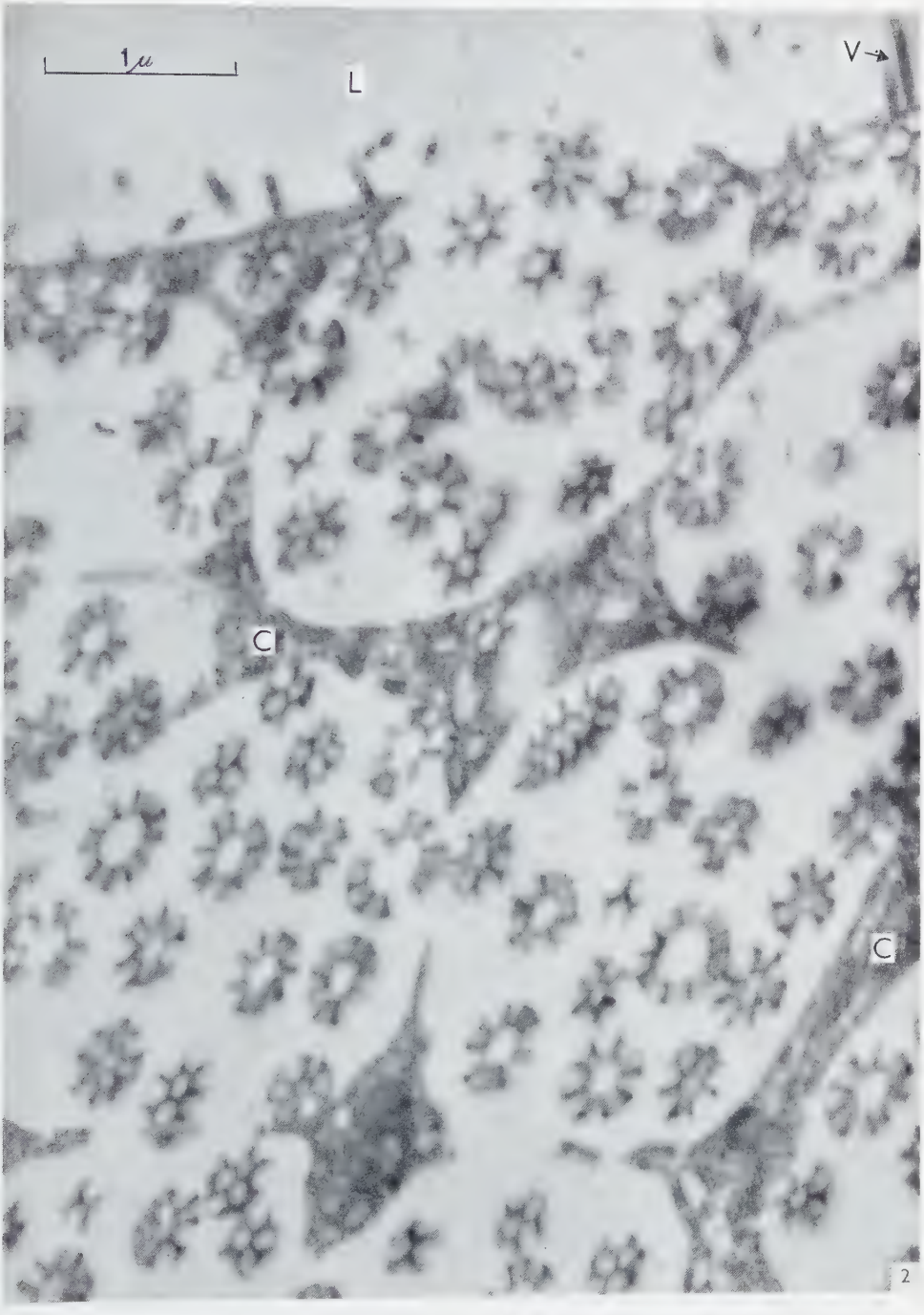

FIG. 2. Section of posterior cell of malpighian tubule of *A. torrida* showing cytoplasm (*C*) reduced to strands surrounding brochosome-containing cavities. Lumen surface has sparse microvilli (*V*) and is ruptured, releasing brochosomes into the lumen (*L*). ×26,000.

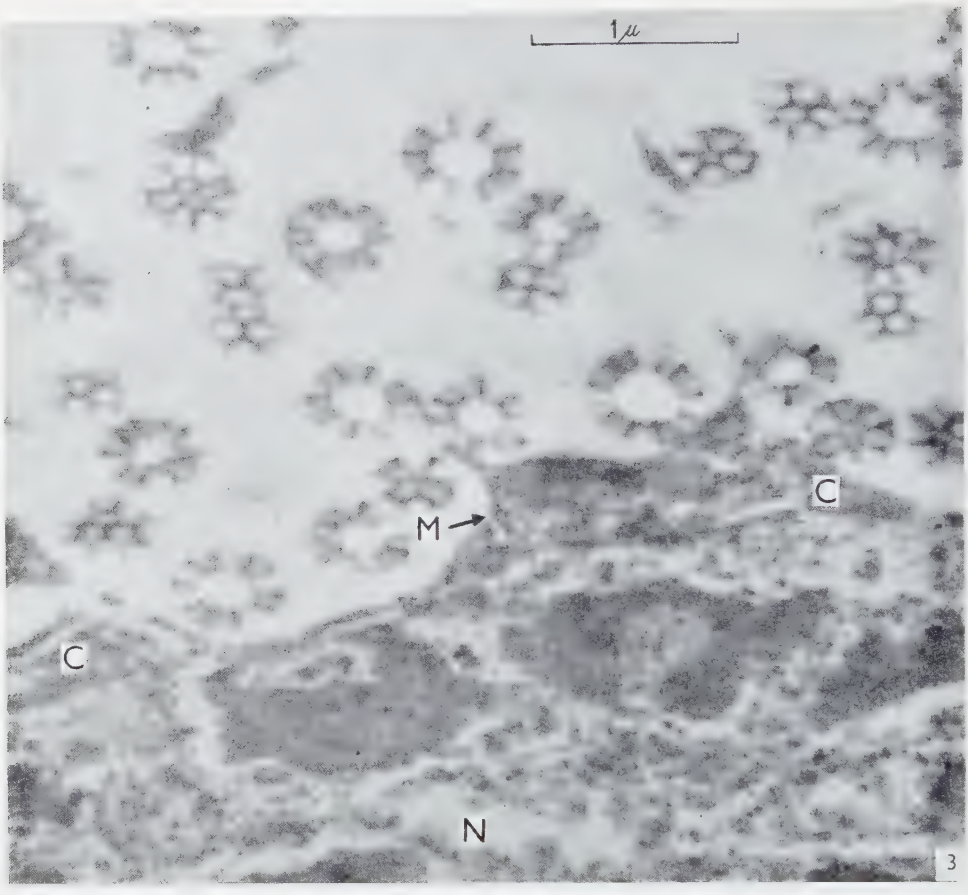

FIG. 3. Nucleus (*N*) of malpighian tubule cell surrounded by thin layer of cytoplasm (*C*) bounded by a thin membrane (*M*). ×27,000.

The contents of the malpighian tubules of the following species of insects were examined in the electron microscope: *Ctenolepisma longicaudata* Esch. (Thysanura), *Periplaneta americana* (L.) (Orthoptera), *Nezara viridula* (L.) (Hemiptera), *Myzus persicae* (L.) (Hemiptera), *Tenebrio molitor* L. (Coleoptera), *Apis mellifera* L. (Hymenoptera), *Aedes aegypti* L. (Diptera), *Musca domestica* L. (Diptera), *Tineola bisselliella* (Humm.) (Lepidoptera).

None contained brochosomes, although other interesting bodies were observed. It seems likely that the brochosomes on the wings of a mosquito recorded by Tulloch and Shapiro (*5*) were due to contamination. Uncontaminated haemolymph of leafhoppers was examined, but no brochosomes were found. In view of the difficulty of

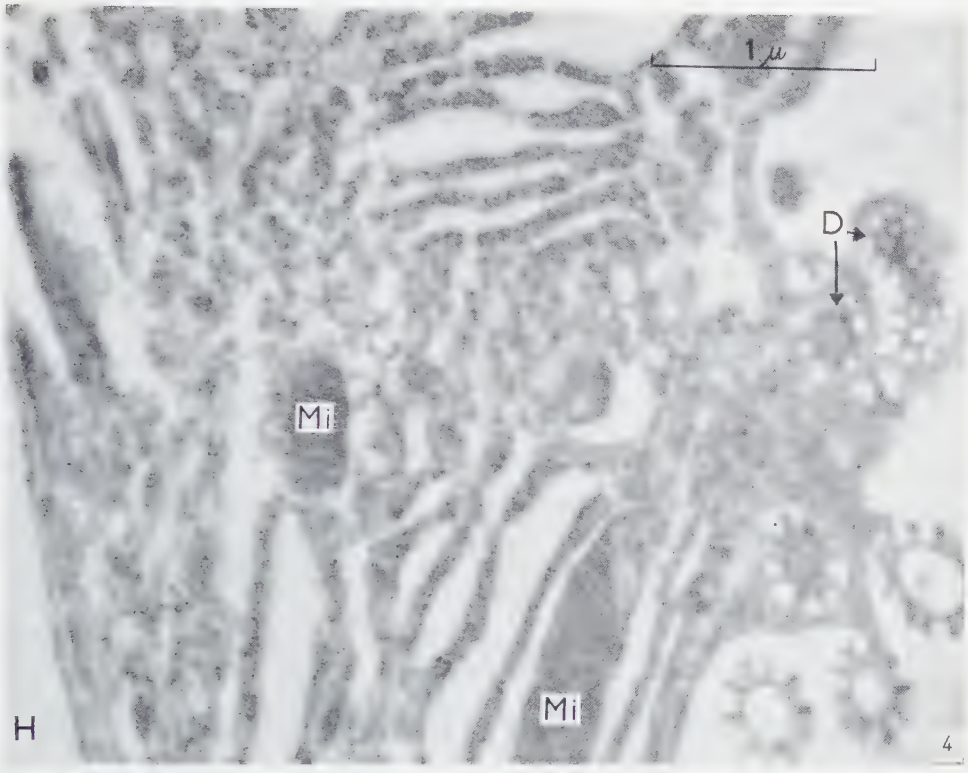

FIG. 4. Basal portion of cell showing haemocoele (*H*) on left. In cytoplasm are mitochondria (*Mi*), membranous structures, and developmental forms of brochosomes (*D*). × 29,000.

avoiding contamination, it may be that the occasional occurrence of brochosomes in body fluids reported by Tulloch and Shapiro (*6*) was due to contamination with the contents of the malpighian tubules.

Having demonstrated that the brochosomes originate in the malpighian tubules, it seemed desirable to examine their mode of formation in these organs. The malpighian tubules of leafhoppers are four in number and are made up of two regions, a posterior wider region of large cells and a narrower anterior part where the tubules are attached to the filter chamber. These anterior cells, when examined in the electron microscope, are seen to have microvilli on the lumen surface and an infolded basal membrane similar to grasshopper malpighian tubules (*1*); they resemble mammalian cells involved in water transport (*3*). The histology of the posterior cells is peculiar. Almost every cell is binucleate and in the light microscope the cytoplasm has a foamy appearance. When thin sections of this material, fixed in buffered 1% OsO_4,

are examined in the electron microscope, the cytoplasm is found to be reduced to interconnected threads surrounding large cavities containing the brochosomes (Fig. 2). The cytoplasm limiting the vacuoles is surrounded by a membrane probably double and about 60 Å in width; no other electron-dense material is observed in these vacuoles. A few microvilli are seen on the lumen surface (Fig. 2) and adjacent to the basal surface membrane are the remains of infoldings of the membrane and most of the mitochondria of the cell (Fig. 3). The brochosome-containing sacks fill the cytoplasm, and only a thin layer of cytoplasm surrounds the nucleus (Fig. 4).

Some presumed developmental forms have been seen in vacuoles in undifferentiated cytoplasm. They have a dense core and the peripheral "spokes" appear first (Fig. 3). These small vacuoles presumably fuse with the larger ones containing fully formed brochosomes. It is suggested that the brochosomes pass into the lumen when the wall of a cavity adjacent to the lumen surface ruptures. The sections of the brochosomes suggested that the tentative structure assigned to them by Tulloch and Shapiro (*5*) was in need of modification. A model incorporating the features observed in whole brochosomes and in sections was constructed of wire and photographed from several angles (Fig. 1 *B-E*). The distribution of material is along the edges of a regular dodecahedron with a single projection out from each of the corners, symmetrically placed with respect to each corner, and in length approximately equal to a side of the constituent pentagons. There is a thin membrane surrounding the body which is difficult to see in sections because of lack of contrast but which is plainly visible in isolated brochosomes and is applied closely over the "spokes" (Fig. 1 *A*). Although the majority of brochosomes conform to this structure, many anomalous forms are seen, the most common of which is the substitution of two or more hexagons as sides of the figure. This accounts for the observed variation in size.

The extraordinary structure of these minute bodies, which appear very similar irrespective of the leafhopper from which they are obtained, gives no clue to their composition or function.

REFERENCES

1. Beams, H. W., Tahmisian, T. N. and Devine, R. L., *J. Biophys. Biochem. Cytol.* **1**, 197 (1955).
2. Day, M. F. and McKinnon, A., *Australian J. Sci. Research Ser. B* **4**, 125 (1951).
3. Pease, D. C., *J. Biophys. Biochem. Cytol.* **2**, Suppl., 203 (1956).
4. Storey, H. H. and Nichols, R. F. W., *Proc. Roy. Entomol. Soc. London* **12**, 149 (1937).
5. Tulloch, G. S. and Shapiro, J. E., *Bull. Brooklyn Entomol. Soc.* **48**, 2, 57 (1953).
6. —— *Science* **120**, 232 (1954).
7. Tulloch, G. S., Shapiro, J. E. and Cochran, G. W., *Bull. Brooklyn Entomol. Soc.* **47**, 41 (1952).
8. Wilde, W. H. A. and Cochrane, G. W., *Proc. Entomol. Soc. Brit. Columbia* **53**, 19 (1957).

Submicroscopic Structure of Frozen-Dried Epiphyseal Plate and Adjacent Spongiosa of the Rat[1]

W. C. DURNING, M.D.S. (N.Z.), PH.D.

Departments of Anatomy and Physiology and the Zoller Memorial Dental Clinic, the University of Chicago, Chicago, Illinois[2]

Received September 8, 1958

The epiphyseal plate and adjacent spongiosa of young rats were prepared for electron microscopy by freezing and drying, followed by post-fixation and staining. Cartilage cells fill their lacunae and extend delicate processes into the matrix. Their protoplasm contains numerous submicroscopic vacuoles. Changes in cartilage cells during maturation are described. The structure of cartilage matrix is interpreted as consisting of two components, the denser interrupting the homogeneous one, which is Hotchkiss-positive.

Osteoblasts and osteocytes contain ribonuclease-sensitive granules associated with the walls of the cytoplasmic submicroscopic vacuoles. There is osteoid between the closely-packed collagen fibrils of bone and the osteoblasts. Somewhat removed from the latter, collagen fibrils seem to arise in a close-meshed network of non-striated elements. The deposition and resorption of the mineral crystals in cartilage are described. Changes in the cells and matrix of cartilage after fixation in aqueous osmium tetroxide are also described.

Most of the literature dealing with the fine structure of cartilage and bone is concerned with bone mineral and its relations to the organic structures in these tissues. Little has been published on the fine structure of cartilage matrix, and less on the cellular elements of cartilage and bone.

The findings described in this paper are the summary of a systematic study of the fine structure of the epiphyseal plate and the adjacent spongiosa of young rats. The material was prepared by freezing and drying and studied morphologically and to some extent cytochemically. Unstained tissue post-fixed in alcohol served for study of the distribution of crystals, while material stained with platinic tetrabromide was suitable for morphological studies of both cells and matrix. In addition, some specimens were stained with gallocyanin-chromalum for basophilic components of

[1] The expenses of the study were shared by grants from the Wallace C. and Clara A. Abbott Memorial Fund and the Zoller Memorial Dental Clinic, both of the University of Chicago, the Commonwealth Fund, and the Josiah Macy, Jr. Foundation.

[2] Present address: University of Otago Dental School, Dunedin, New Zealand.

nucleus and cytoplasm, and others were stained by the Hotchkiss procedure. Material prepared in these ways was compared with specimens fixed by immersion in the buffered aqueous osmium solution of Palade (*19*).

MATERIALS AND METHODS

Eighteen Sprague-Dawley rats seven to forty-eight days old were used. The animals were killed by decapitation or by a blow on the head followed by exsanguination from the large thoracic blood vessels. The hind limb was quickly removed, cleared of attached soft tissue, and the proximal half of the tibia was placed in a moist chamber where it was split lengthwise. Slices of epiphyseal plate and spicules of adjacent spongiosa were subdivided into very small pieces (about $50\mu \times 100\mu \times 1$ mm). Several pieces at a time were placed on small squares of metal foil and quickly immersed in liquid propane cooled to about -175°C in liquid nitrogen (*10*). The total elapsed time between the death of the rat and the freezing of the specimens was usually three to four minutes.

The specimens remained in liquid nitrogen until they were placed in a refrigerated tube at about -37°C, and dried *in vacuo* for about twenty-four hours. The drying tube was then allowed to reach room temperature, and most of the specimens were heated *in vacuo* at 100°C for about twelve hours and then infiltrated with 95% alcohol. The others were infiltrated with alcohol without heating. The apparatus used was designed by Finck (*9*). The vacuum was then broken and the specimens were transferred to 95% alcohol in Feigl tubes, in which they remained for at least twelve hours.

One group of tissues was fixed by immersion in 2% aqueous buffered osmium tetroxide according to the method of Palade (*19*). After two and one-half hours, the tissues were rinsed briefly in distilled water, dehydrated through graded alcohols and double embedded without further treatment. The details of the double embedding procedure will be given later.

In the preliminary stages of the work, the heat- and alcohol-denatured specimens were stained in alcoholic solutions of platinic tetrabromide, osmium tetroxide, lead acetate, phosphotungstic acid, and phosphomolybdic acid. Platinic tetrabromide was found to be most satisfactory, and in time came to be used almost exclusively for general morphology.

Some specimens were stained with gallocyanin-chromalum for basophilia. As controls, other specimens were treated with ribonuclease or with distilled water. The procedure was essentially that of Finck (*9*) with the following modifications: the time of immersion in each grade of alcohol was reduced from two hours to one hour; the time of digestion with ribonuclease was reduced from ten hours to two; and the washing time in distilled water was reduced from two hours to ten minutes. The time of immersion of the water controls was modified accordingly.

In order to preserve the morphologic detail, which was disturbed by this treatment despite the modifications noted above, some specimens were embedded in nitrocellulose before staining. This was later removed prior to rehydration before staining with gallocyanin-chromalum.

Another group of specimens was stained with the Hotchkiss method as modified by Bondareff (*1*). In control preparations, specimens were treated exactly as for the Hotchkiss method, except that the dye was omitted.

The following schedule, devised by Isenberg (*14*) and previously unpublished, for embedding of specimens in methacrylate, was used:

(1) 95% alcohol	
(2) Absolute alcohol	2 hours
(3) Absolute alcohol and ether (1:1)	2 hours
(4) 7.5% nitrocellulose	2–3 hours
(5) 15% nitrocellulose	48 hours
(6) Chloroform until hardening takes place	
(7) Methacrylate monomer and chloroform (1:3)	1–2 hours
(8) Methacrylate and chloroform (1:1)	2 hours
(9) Methacrylate and chloroform (3:1)	2 hours
(10) Methacrylate monomer	Overnight in refrigerator

The methacrylate-containing specimens were polymerized by the platform method described by Finck (*9*).

The blocks were trimmed and very thin sections were cut, floated on water and mounted on formvar films over the slit in the silver specimen mounts. To reduce solution of inorganic crystals, sections were floated on water partly saturated with chemically pure tricalcium phosphate (Baker). Each section was mounted as soon as it was cut.

Sections were viewed with a Philips EM 100 A electron microscope, with a rated resolution of 20 Å, calibrated with a replica grating of 30,000 lines per inch. Electron micrographs were made at a magnification on the screen of 4000 to 90,000 ×, with Adox KB–14 film, or in some instances with Kodak Spectroscopic film type 649GH. The image on the film is about one-third that on the screen. The Adox film was developed in Microdol (six minutes at 20° C) and the spectroscopic film in D19 (ten minutes at 20° C). The prints were usually enlarged 5 × and occasionally 8 .

RESULTS

Description of Cartilage

Cells

The cytoplasm and nucleus of cartilage cells of the epiphyseal cartilage stained with platinic tetrabromide consist of submicroscopic vacuoles ranging from 500 to 1000 Å (Figs. 1, 2 and 4). The walls of the nuclear vacuoles are thin and fairly uniform, except in regions corresponding with chromatin and the nucleolus, where they are thicker. In the cytoplasm, the size of the submicroscopic vacuoles and the thickness of their walls varies more noticeably. In some areas of the younger cells, at low magnification, the cytoplasm seems to contain denser lines, fibers, or elongated channels. Closer study reveals that these are thicker walls of the general vacuolar pattern coursing through the cytoplasm singly, in pairs, or in larger numbers. They are clearly interconnected by thinner walls completing the vacuolar structure. Sometimes these are regularly aligned (Fig. 4). The thicker walls appear in all planes of

section of the cartilage cells and must therefore be distributed in three dimensions throughout the cytoplasm as continuous denser sheets.

As the cells hypertrophy, the submicroscopic vacuoles increase in size in certain regions and, accompanying this, two particular changes take place. One is the formation of microscopic vacuoles, and the other the formation of cytoplasmic fibers or sheets in older cells. The lined-up submicroscopic vacuoles previously described increase in size and eventually the connecting walls are no longer apparent. The cross-connecting walls become thinner and eventually disappear. The remaining thicker walls persist as long fibers or sheets with small irregular densities along their course (Fig. 4). In other areas, the walls of the enlarged submicroscopic vacuoles break down (Fig. 3) and by progressive coalescence of these areas, larger spaces are formed. In some instances these large spaces are filled with homogeneous material while in others they appear empty. The main features of the cartilage cells are the same in unstained alcohol control preparations.

Cytoplasmic processes extend into the matrix, and their submicroscopic structure is essentially that of the cell body. As the processes become thinner, they seem to terminate imperceptibly in intimate contact with the matrix (Figs. 1, 2 and 3). Although uncommon in the more elongated (younger) cartilage cells, except at the ends (Fig. 1), they become more widely distributed along all surfaces as the cells hypertrophy (Fig. 2). In the older cells, they become uncommon again (Fig. 3) and in the degenerating cells they are rare.

All staining procedures of the frozen-dried specimens involving the use of watery reagents cause shrinkage of the cartilage cells, retraction of their cell processes, loss of fine structure, and leaching out of material with a consequent reduction of contrast. These changes are less marked following the Hotchkiss procedure and are

---

FIG. 1. Electron micrograph of section of a young cartilage cell in the proximal tibial epiphyseal plate of a rat sixteen days old. Fixation was by freezing and drying with post-fixation by heat denaturation *in vacuo* and 95% alcohol, with subsequent staining for five hours with alcoholic platinic tetrabromide. × 4350.

FIG. 2. Electron micrograph of section of a mature cartilage cell in the epiphyseal plate of the tibia of the same rat as in Fig. 1. Fixation and staining were the same as for Fig. 1. × 4350.

FIG. 3. Electron micrograph of section of a moderately hypertrophied cartilage cell of the epiphyseal plate of the tibia of a rat thirty-two days old. The specimen was treated as described for Fig. 1. 4350.

FIG. 4. Electron micrograph of part of the same cartilage cell as illustrated in Fig. 2 to show details of cell structure. × 17,000.

FIG. 5. Electron micrograph, at very high magnification, of calcified cartilage from the proximal tibial epiphysis of a twenty-one day old rat. Fixation and subsequent treatment the same as that described for Fig. 6. × 93,600.

FIG. 6. Electron micrograph of calcifying cartilage matrix. Fixation was by freezing and drying with post-fixation by heat denaturation *in vacuo* and 95% alcohol. No stain was used. Sections were cut into a partly saturated solution of chemically pure tricalcium phosphate and mounted singly in order to reduce the solution of the inorganic elements. × 17,000.

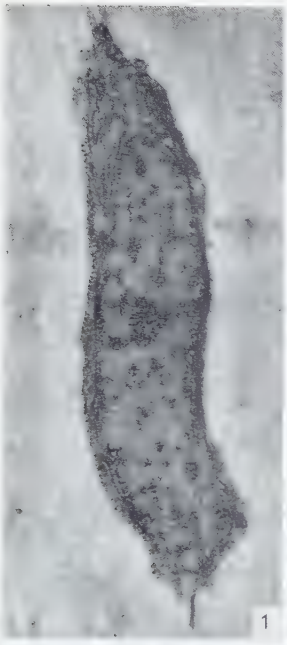
1


2

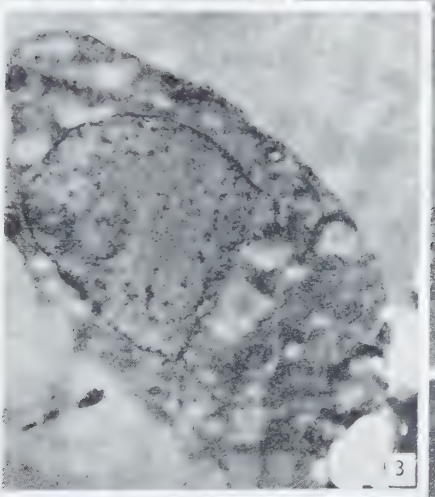
3


4

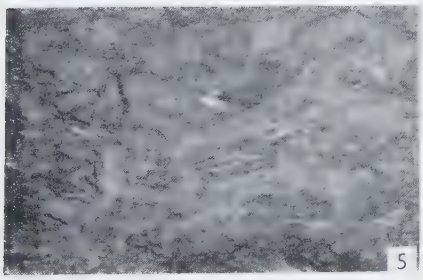
5

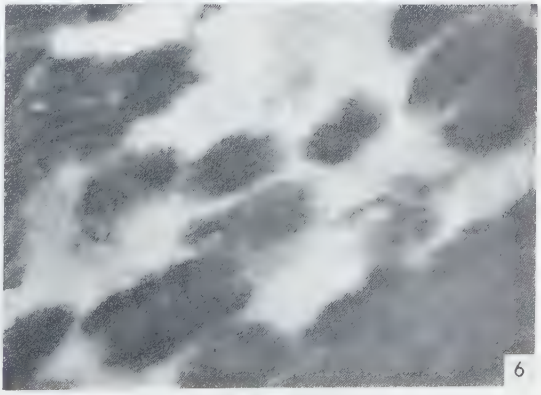
6

more marked following the use of ribonuclease, buffered saliva, distilled water, and frequently the gallocyanin-chromalum stain. Many of these changes occurred also after fixation by immersion in aqueous buffered osmium solution. Because of the artifacts caused by the use of aqueous reagents, it was not possible to study the distribution of glycogen and basophilic components in the cartilage cells.

Organic cartilage matrix

After staining uncalcified and decalcified matrix with alcoholic platinic tetrabromide, two components of different contrast appear (Fig. 2). The same components appear in the unstained alcohol controls, but with less marked contrast. The denser component consists of thin "walls" with side branches of different sizes which divide the homogeneous component of lower contrast into "chambers" which are partly continuous (Fig. 9). The matrix chambers adjacent to the cartilage cells are in general less dense and larger than those closer to the middle of the matrix columns and matrix cross-plates between the columns (Fig. 9). These differences are less marked in the matrix chambers surrounding the older cells.

The orientation of the matrix walls (and the matrix chambers they enclose) varies with the plane of section. If the section is cut parallel to the long axis of the matrix columns, the walls in the latter give the impression of being long fibrils (Fig. 2), while the walls in the matrix plates appear to form interconnecting net-like lines. These relations are reversed when the section is transverse to the long axis of the matrix columns. In no plane of section are there dense granules which would be expected from transverse sections of elongated fibrils.

FIG. 7. Electron micrograph of a section of an osteoblast and adjacent osteoid from the proximal tibial epiphyseal plate of a twenty-one day old rat. Fixation and subsequent treatment the same as that described for Fig. 1. The osteoblast is separated from the bone matrix by an osteoid border. 20,000.

FIG. 8. Electron micrograph of calcified matrix of bone spicule of the secondary spongiosa of the tibia of a rat forty-eight days old. The specimen was frozen and dried, denatured in heat and alcohol, and embedded in methacrylate without staining. × 92,000.

FIG. 9. Electron micrograph showing higher magnification of the structure of cartilage matrix near a moderately hypertrophied cartilage cell and prepared in the same way as Fig. 1. A portion of the cell is seen in the lower right-hand corner. × 16,700.

FIG. 10. Electron micrograph of undecalcified, unstained, cartilage matrix of a twenty-one day old rat. This micrograph illustrates the most commonly seen type of resorption. × 16,700.

FIG. 11. Electron micrograph of cartilage from the proximal tibial epiphysis of a fifteen day old rat to show the termination of cytoplasmic extensions of a growing cartilage cell within the cartilage matrix. × 35,500.

FIG. 12. Electron micrograph of cartilage matrix from an area of beginning calcification in the tibial epiphyseal plate of a twenty-one day old rat. Fixation was by freezing and drying with post-fixation by heat denaturation *in vacuo* and 95% alcohol. No stain was used. Sections were cut into a partly saturated solution of chemically pure tricalcium phosphate and mounted singly as they were cut in order to reduce the solution of the inorganic elements. × 33,500.


7


8


9

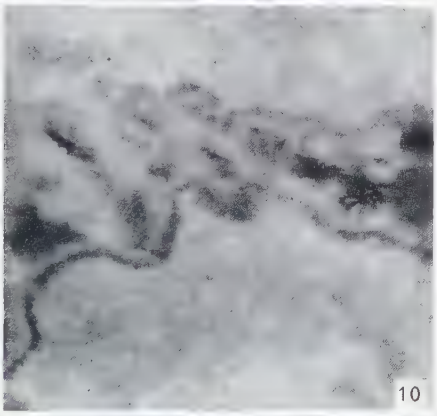
10


11

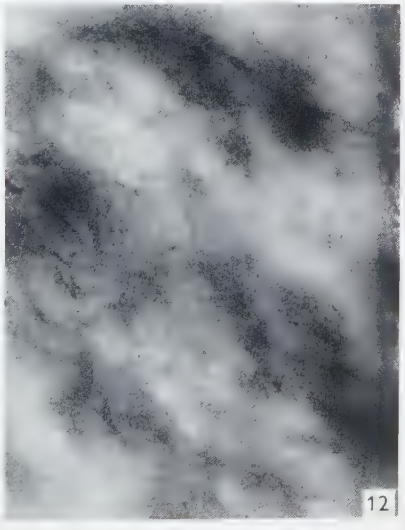
12

At higher magnifications, the walls vary somewhat in thickness and density from the elongated ones in the central parts of the matrix columns, where they are thickest (about 500 Å), to the various orders of sheet-like extensions which, in their finest branchings, approach the density of the homogeneous component (Fig. 9).

In order to learn which of the two components of the matrix is more stainable with the Hotchkiss reagents, electron micrographs were made of comparable regions of cartilage from the same epiphyseal plate. One group of sections was made from specimens stained with the Hotchkiss method; another group of sections was made from specimens treated in the same way, except that leucofuchsin was omitted. The micrographs were made at the same magnification, accelerating voltage, and estimated electron intensity. Prints were made in which the homogeneous matrix component was matched. In nearly all pairs of prints, in the specimens treated with the Hotchkiss method, the matrix walls are thicker and have less contrast.

The effects of water on the matrix of frozen-dried specimens are quite marked. In frozen-dried material treated by any of the aqueous stains, as well as in material fixed by immersion in aqueous osmium solution, the long sheets of denser material with their lateral extensions now appear as fine fibrils of irregular length and thickness, and as granules.

Calcified cartilage matrix

The deposition and resorption of mineral were studied in sections of the alcohol control specimens. Calcified regions are apparent because of their increased density and correspondingly greater capacity for electron scattering, as compared with the organic matrix. Calcium deposits appear first in the longitudinal matrix columns at the level of markedly hypertrophied cartilage cells, usually three or four cells removed from the area of bone formation. The earliest stage is seen as an increased density associated with the walls of the cartilage matrix, which thus become more prominent and thicker than in decalcified matrix (Fig. 12). The chamber matrix then becomes filled with dense material. Each unit consists finally of a heap of unoriented, interlaced, needle-like crystals (Fig. 6), 35 Å to 60 Å in diameter, and up to 1000 Å long (Fig. 5). Because the sections were thin, it is possible that some crystals may have been longer. Lengthwise, the crystals are divided into sub-units of about 40 Å.

Calcification occurs first in the middle part of the cartilage columns and later in the middle part of the cross plates. In the end, in both regions, the final picture is one of closely apposed units (or foci) of calcification (Fig. 6). Resorption of the calcified deposits is first evident in the cross plates, usually in regions where mesenchymal cells occupy the space formerly filled by a degenerated cartilage cell. Here calcium densities are confined to a pattern of dense matrix walls and of less dense regions giving an appearance resembling that seen in the early stages of calcium

deposition. Between the area of calcium resorption and the surrounding uncalcified area is a dense layer of crystals oriented at right angles to the resorbing surface (Fig. 6). This layer of crystals (about 500 to 700 Å thick) is separated from the calcium-rich cartilage matrix by a decalcified zone of about 0.25 μ thick. The organic matrix remaining after decalcification is in general not different from uncalcified cartilage matrix, though sometimes the homogeneous matrix compartments seem less dense. Only rarely are cells in immediate contact with such regions of decalcification.

While this description is general for calcium resorption, some exceptional areas are noted. In these areas, the cytoplasm of adjacent cells is often seen in quite close apposition to the resorbing surface. Calcium salts appear to be removed from the surface of the fully calcified cartilage directly, and there is no evidence of the "line" or layer previously described. As compared with the homogeneous component of normal uncalcified matrix, there are now irregularities in density of this component, some regions being largely empty. In addition, non-crystalline, apparently amorphous, deposits of calcium occur.

Description of Bone Spicules

Cells

The submicroscopic vacuoles of the protoplasm of osteoblasts are very clear after frozen-dried specimens are stained with platinic tetrabromide (Fig. 7). They are also apparent, though less distinct, in unstained alcohol controls. In the cytoplasm, the submicroscopic vacuoles are rather randomly arranged and evenly distributed. There is a variable number of homogeneous, rather dense granules (possibly mitochondria), which are spherical (about 0.2 μ) or oval (about 0.2 $\mu \times 0.6$ μ). In the nucleus, the submicroscopic vacuoles are in general uniform except in small patches chiefly around the periphery of the nucleus, where the walls are thicker and denser and the vacuoles correspondingly smaller.

After staining with gallocyanin-chromalum, many small granules are observed in the cytoplasm and nucleus. In the cytoplasm, granules occur in groups in the walls of the submicroscopic vacuoles. In some areas, the granules are aligned in rows. In the nucleus, the granules are distributed in a pattern corresponding with the dense regions, chiefly peripheral, of material stained with platinic tetrabromide. A large nucleolus is frequently seen. When specimens are digested with ribonuclease before staining with gallocyanin-chromalum, the cytoplasmic granules are no longer detectable, although the nuclear (chromatin) granules persist. In the specimens treated with distilled water and then stained, the granules are less numerous than in untreated preparations. Both ribonuclease-treated and water-treated specimens show some disruption of fine structure.

Osteocytes are seen relatively infrequently. Frozen-dried osteocytes, stained with platinic tetrabromide, have essentially the same fine structure as that of osteoblasts. The osteocytes are smaller, with many long processes extending into the matrix. The nucleus is relatively large, and is enclosed by a thin layer of cytoplasm impinging directly on the lacunar wall. After staining with gallocyanin-chromalum, discrete granules appear in both the nucleus and the cytoplasm. In the cytoplasm, they are fairly sparse and in large areas there are none. In the nucleus, they are also small and distributed as in the nucleus of the osteoblast. The nuclear granules are not affected by treatment with ribonuclease prior to staining. No granules are observed in the cytoplasm after this treatment. In the specimens treated with distilled water as a control for ribonuclease digestion, some granules are still found to be present in both cytoplasm and nucleus. The treatment with enzyme and with water results in some disruption of fine structure.

Organic bone matrix

In specimens stained with platinic tetrabromide, the calcium crystals are removed. The mature matrix consists largely of closely packed fibrils with a regular periodicity of about 600 Å. The osteoid border consists of an open network structure. Close to the cell there are usually no striated fibrils, but further from the cell there is a gradual orientation of the network so that it appears to be made up of long, interconnected, non-striated fibrils. These become more closely oriented and packed, striations become visible in parts of some of them, and eventually they become indistinguishable from the collagen fibrils in the mature matrix (Fig. 7). In areas where bone is being deposited on cartilage this same sequence of events occurs. As the osteoblast moves away from the cartilage and the osteoid border becomes wider, mature bone matrix is seen adjacent to the cartilage.

Unstained calcified bone

No calcium crystals were observed in the more open reticulated portion of the osteoid border. In fully developed bone, many needle-shaped particles appear with their long axes parallel to the general direction of the long axis of the fibers. The crystals are 40 Å to 60 Å thick and vary from 140 Å to 300 Å in length (Fig. 8).

DISCUSSION

Cartilage

Cells

The structure of cartilage cells prepared by freezing and drying is essentially similar to that of liver cells (*9*, *11*) and of fibroblasts (*2*). The outstanding characteristic of the protoplasm is its appearance as a system of submicroscopic vacuoles (500 Å to

1000 Å in diameter), most of which are enclosed by even, thin walls. However, the thickness of the walls does vary. In some parts of the cytoplasm, these thickenings form a linear pattern in all planes of section of the cartilage cells. Because of this, they should be regarded as thickened walls of oriented submicroscopic vacuoles which form sheet-like structures related to each other and to the walls of other submicroscopic vacuoles by the thinner walls of the component submicroscopic vacuolar units.

The thickened part of the walls of the submicroscopic vacuoles seems to be considerably more stable than the thinner parts. It persists in older cartilage cells long after the thinner parts of the wall have disappeared. The nucleolus and the cytoplasmic lamellae are quite regularly the only morphologically distinguishable elements remaining in markedly degenerated cartilage cells.

The special arrangements of thickened walls observed in frozen-dried cartilage cells correspond to the ergastoplasmic lamellae described by Scott and Pease (*26*) after their study of cartilage cells fixed by immersion in a buffered solution of osmium tetroxide. The presence of these structures in osmium-fixed cartilage cells was confirmed in this study.

It is suggested that the sheet-like appearance in osmium-fixed cells is an artifact arising during fixation through breakage and solution of the walls of submicroscopic vacuoles intervening between the adjacent, continuous, thickened wall complexes observed in frozen-dried preparations. In support of this suggestion is the observation that treatment of frozen-dried preparations with aqueous reagents results in structural patterns which simulate the ergastoplasmic lamellae observed after immersion in buffered aqueous osmium solution. Although the fine structure of younger and moderately hypertrophied cells prepared by freezing and drying differs from that of the same cell stages prepared by osmium fixation, the details and organization of the degenerating cartilage cells are in many instances quite similar.

Cartilage cells after freezing and drying fill their lacunae. Fine processes extend from the cell body into the cartilage matrix. In the younger cells, these processes extend from the truncated blunt surfaces; in the moderately hypertrophied cells they occur on all surfaces; and in the most hypertrophied cells, which presumably are no longer increasing in volume, they are absent or uncommon. This sequence suggests that the cell extensions are taking part in the process of enlargement of the cell lacunae, perhaps by inducing solution of matrix components and filling out the solubilized area of matrix. In marked contrast to the fully occupied appearance of cartilage lacunae after freezing and drying are the lacunar spaces around cartilage cells fixed in aqueous osmium solution. This effect of fixation in osmium is interpreted as a shrinkage artifact. The irregular outline of such cells would seem to represent regions of retraction, and the extensions of their cytoplasm may not correspond with the cell processes observed in frozen-dried material.

Matrix

The structure of the cartilage matrix after freezing and drying appears to be significantly different from that observed after fixation in aqueous osmium solution. When frozen-dried epiphyseal plate is post-fixed by heat denaturation and alcohol (with or without subsequent staining with platinic tetrabromide), the cartilage matrix consists of two components: a homogeneous component of moderate density and a series of long sheets (about 500 Å thick) interconnected by several orders of decreasingly thin sheets. The net result is the occurrence of oriented, partly separated and intercommunicating chambers containing the homogeneous component. The sheets form a pattern in the columns of matrix and in the cross plates and the dimensions of the chambers vary as they approach the cartilage lacunae.

The appearance of the denser component of cartilage matrix is markedly different after fixation in aqueous osmium. After such treatment, this component appears as a system of fibrils with irregular thickenings along their course and with granules intervening between them. Martin (*18*) described the matrix as a felt-work of nonperiodic, interlacing fibers. Jackson (*15*) described the matrix as a meshwork of unbanded fibrils associated with amorphous material near the cartilage cells. Robinson and Cameron (*23*) described fibrils sometimes arranged in bundles in neonatal human cartilage and were the only investigators to describe a repeating period of 200 Å in some of the fibrils. In their illustration, a finely granular element is present between the fibrils. Scott and Pease (*26*) classified matrix in the epiphyseal cartilage of kittens as "non-fibrillar capsular matrix" surrounding the cells, and an "intercapsular matrix" consisting of a network of fine fibrils. It would seem that this capsular matrix is an artifact resulting from shrinkage of the cartilage cells and the filling-in of the shrinkage space with materials dissolved in the osmium solution during fixation.

The fibrillar network described in cartilage matrix after fixation in osmium was observed in this study also. It was also observed in varying extent in frozen-dried material post-fixed by heat denaturation and alcohol and then treated with aqueous reagents. It is suggested that the fibrils of cartilage matrix observed after fixation in osmium solutions may be fragmented portions of the sheets observed in material prepared by freezing and drying and suitably post-fixed.

When epiphyseal cartilage is stained by the periodic acid leucofuchsin method of Hotchkiss and examined in the light microscope, the cartilage matrix appears pink to red. It was of interest to learn which of the two submicroscopic components of cartilage matrix is responsible for the color. It appears that the reactive groups responsible for the color are chiefly in the homogeneous component.

In calcified cartilage matrix, Robinson and Cameron (*23*) describe inorganic crystals 250–750 Å long and 50–70 Å wide, which are not related to the fibers. They

show further that as calcification progresses, clusters form, with the crystals arranged haphazardly at their centers but radially arranged at the periphery. Scott and Pease (*26*) report essentially the same findings.

The results reported in this paper for the inorganic element of cartilage matrix are in general agreement with the findings reported above, but the needle-like crystals are seen with diameters 35–60 Å, and 220–1000 Å long, with the long dimension divided into sub-units of about 40 Å. With the better preservation of the matrix when it is prepared by freezing and drying it is possible to get more reliable information on the relationship of the crystals to the organic elements. The earliest deposition of calcium appears associated with the walls of the cartilage matrix, and as crystals accumulate they appear to fill the adjacent chambers, giving the appearance of clusters of unoriented needle-like crystals, with the crystals at the periphery of the cluster radiating out along the walls in the matrix.

Bone

Cells

After freezing and drying, the most prominent feature of the protoplasm of osteoblasts and osteocytes is the occurrence of submicroscopic vacuoles. These were not observed after osmium fixation, as reported by Jackson (*16*) and by Scott and Pease (*26*) in the only published reports on the fine structure of these cell types. Jackson (*16*) described the presence of numerous granules in the cytoplasm, not visible in material prepared by freezing and drying and like Scott and Pease (*26*) described a series of channels enclosed within lamellae. These were observed in frozen and dried cells only when they had been treated with aqueous reagents.

In an extensive study of frozen-dried liver cells, Finck (*9*) showed that gallocyanin-chromalum stains basophilic components of protoplasm for study with the electron microscope as specifically as for the light microscope. In osteoblasts, fine basophilic granules frequently were observed in the walls of groups of submicroscopic vacuoles in the cytoplasm, in the nuclear chromatin, and in the nucleolus. After treatment with ribonuclease followed by staining with gallocyanin-chromalum, only the granules of the chromatin remained intact. In osteocytes, there were few basophilic granules in the cytoplasm. No nucleoli were seen, perhaps because of the small number of osteocytes observed.

These observations are consistent with some recent descriptions of basophilia in osteoblasts and osteocytes based on studies with the light microscope. Pritchard (*21*) regarded intense basophilia as a characteristic feature of osteoblasts. Cappellin (*3*) described loss of cytoplasmic basophilia and reduction in the size of the nucleolus as the osteoblast is surrounded by matrix and becomes an osteocyte. Heller,

McLean and Bloom (*12*) and Pritchard (*20*) presented evidence which suggests that the degree of basophilia varies with the state of activity of the osteoblast. In accord with this is the observation in this study that the number of basophilic granules varies in different osteoblasts.

Matrix

The most prominent features of the organic part of mature bone matrix are the closely packed collagen fibrils with a regular periodicity of about 640 Å (*13*, *16*, *25*). This arrangement of fibrils in the mature matrix differs from that in the developing osteoid border. Jackson and Randall (*17*) and Jackson (*16*) described the earliest fibrils as merging with the cell surface. They stated that the mature collagen is separated from the cell by disoriented fine fibrils about 200 Å thick and unbanded. Robinson and Cameron (*23*), on the other hand, claim that the first fibrils are recognizably collagen in the osteoid network laid down between osteoblasts and calcified cartilage. A "fibrous pre-osseous zone" is described by Scott and Pease (*26*). In most of these studies, no calcium deposits are described in this zone, the calcium appearing only where mature collagen fibrils are present.

The osteoid border in frozen-dried material appears initially to be a coarse net of very thin fibrils (about 250 Å thick) which could be interpreted as a system of irregular vacuoles enclosed by thin walls. In some of them appear the characteristic cross striations of collagen. The findings resemble closely those of Bondareff (*2*) on the origin of fibrils in rat tail tendon. He presented evidence suggesting that collagen fibrils identified by their characteristic periodicity arise within the walls by a rearrangement of some precursor. It is suggested that collagen fibrils arise extracellularly in osteoid in a similar way.

The literature on calcium crystals in bone is rather large and shows in some respects a developing measure of agreement. Wolpers (*28*) described bone crystals with diameters of 30–60 Å and 400 1000 Å long. The first comprehensive study on bone crystals was published by Robinson (*22*) and Robinson and Watson (*24*). These authors, in a series of papers, described the largest inorganic elements as platelike particles about 1500 · 500 · 100 Å in senile human bone and of smaller size in a calcification front of rib cortex. The large size of their particles may be due to overlay in sectioned or fragmented preparations, or to the effect of the high intensity of the electron beam.

Fernández-Morán and Engström (*7*) described needle-shaped crystals 30–40 Å in diameter and 200 Å long, with sub-units in the long axis of about 40 Å. Jackson (*16*) described the earliest deposits as granules of about 100 Å, and claimed they were related to the banding pattern of the collagen fibrils. Speckman and Norris (*27*)

reported that the crystals in sections of fresh and frozen-dried bone were 50 Å in diameter and usually 600–700 Å long.

Studies of bone crystals by X-ray diffraction are in better agreement (*4–6*, *8*). Their values for the crystallites range from 50–75 Å in diameter and 200–220 Å in length. Carlström and Finean (*5*) reported also that the X-ray diffraction pattern remained after removal of the organic part of bone with ethylenediamine, and concluded that the X-ray diffraction pattern of intact bones must be attributed to their inorganic components.

Most investigators have observed that the needle-shaped crystals are arranged with their long axes generally parallel to the direction of the long axis of the fibril. Whether the crystals are arranged on the outside of the collagen fibrils of the matrix or are present also within them is not definitely known. Robinson and Watson (*25*) and Jackson (*16*) suggest that the earliest calcium deposits are possibly present both within and on the outside of the fibrils. The crystals observed in bone matrix in this study were 40–60 Å × 140–300 Å with no clear indication of smaller sub-units as described by Fernández-Morán and Engström (*7*).

ACKNOWLEDGEMENTS

The author wishes to express his grateful appreciation to Dr. Isidore Gersh and Dr. Franklin C. McLean for advice and assistance and for their continued interest and encouragement during the course of this work.

REFERENCES

1. Bondareff, W., *Anat. Record* **129**, 97 (1957).
2. —— *Gerontologia* **1**, 222 (1957).
3. Cappellin, M., *Boll. soc. ital. biol. sper.* **24**, 1228 (1948).
4. Carlström, D., *Acta Radiol.*, Suppl. 121 (1955).
5. Carlström, D. and Finean, J. B., *Biochim. et Biophys. Acta* **13**, 183 (1954).
6. Engström, A., *Ciba Foundation Symposium. Bone Structure and Metabolism*, p. 3, 1956.
7. Fernández-Morán, H. and Engström, A., *Biochim. et Biophys. Acta* **23**, 260 (1957).
8. Finean, J. B. and Engström, A., *Biochim. et Biophys. Acta* **11**, 178 (1953).
9. Finck, H., *J. Biophys. Biochem. Cytol.* **4**, 291 (1958).
10. Gersh, I., Isenberg, I., Stephenson, J. L. and Bondareff, W., *Anat. Record* **128**, 91 (1957).
11. —— *ibid.* **128**, 149 (1957).
12. Heller, M., McLean, F. C. and Bloom, W., *Am. J. Anat.* **87**, 315 (1950).
13. Huber, L. and Rouiller, C., *Experientia* **7**, 338 (1951).
14. Isenberg, I., unpublished, 1955.
15. Jackson, S. F., *Proc. Roy. Soc. London B* **142**, 536 (1954).
16. —— *ibid.* **146**, 270 (1957).

17. Jackson, S. F. and Randall, J. T., *Ciba Foundation Symposium. Bone Structure and Metabolism*, p. 47, 1956.
18. Martin, A. V., *J. Embryol. Exptl. Morphol.* **2**, 38 (1954).
19. Palade, G. E., *J. Exptl. Med.* **95**, 285 (1952).
20. Pritchard, J. J., *J. Anat.* **86**, 259 (1952).
21. —— *in* Bourne, G. H. (Ed.), Biochemistry and Physiology of Bone, p. 187. Academic Press Inc., New York, 1956.
22. Robinson, R. A., *J. Bone and Joint Surg.* **34 A**, 389 (1952).
23. Robinson, R. A. and Cameron, D. A., *J. Biophys. Biochem. Cytol.* **2**, Suppl., 253 (1956).
24. Robinson, R. A. and Watson, M. L., *Anat. Record* **114**, 383 (1952).
25. —— *Ann. N. Y. Acad. Sci.* **60**, 596 (1955).
26. Scott, B. L. and Pease, D. C., *Anat. Record* **126**, 465 (1956).
27. Speckman, T. W. and Norris, W. P., *Science* **126**, 753 (1957).
28. Wolpers, C., *Grenzgebiete Med.* **2**, 527 (1949).

The Projection X-Ray Microscope for Divergent-Beam Diffraction[1]

D. CARLSTRÖM and B. LUNDBERG

Department of Medical Physics, Karolinska Institutet, Stockholm

Received December 2, 1958

The projection X-ray microscope is a suitable instrument for divergent-beam diffraction. Monochromatization of the radiation improves the diffraction patterns and increases the possibilities of the divergent-beam method. The use of photographic emulsions with extremely high resolution facilitates the recording of the diffraction patterns.

The divergent-beam method is quite unique among X-ray diffraction techniques, as it does not require any kind of collimating system; instead, the full beam emanating from a point source is utilized. X-ray tubes with suitable properties for this kind of diffraction work have not been easy to obtain in the past, and the divergent-beam method has therefore more or less been looked upon as an interesting curiosity of little practical value for crystallographic routine work. The recent development of the X-ray projection microscope has given new possibilities which make the method more accessible and useful. Because of its simplicity, the divergent-beam method may prove to be a valuable complement to the ordinary single-crystal techniques. It enables quick determination of orientation and symmetry elements of single crystals, and it also furnishes information relating to the degree of crystal perfection. In certain cases it can be used for precision measurements of the dimensions of the crystallographic unit cell.

The aim of this investigation is mainly to suggest some general improvements of technique. It does not seem necessary to give a full description of the divergent-beam method, as Lonsdale (*6*) has presented an excellent study of it with many details, including several important applications.

Basic principles of the divergent-beam method

When a divergent beam of X-rays containing characteristic radiation traverses a single crystal, two kinds of diffraction effects can be observed. Each family of planes

[1] This investigation has been supported by grant D 700 from The National Institutes of Health and by Contract AF 61(052)-15 from the European Office of Air Research and Developmental Command, U.S. Air Force, Brussels, Belgium.

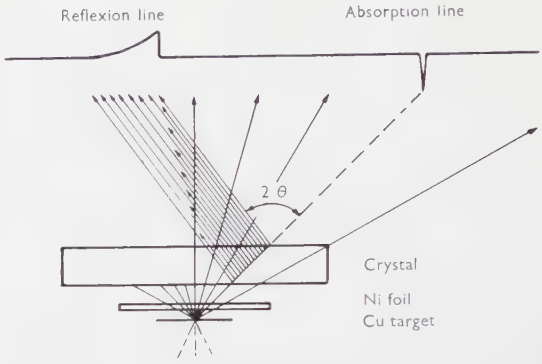

FIG. 1. Formation of absorption and reflection lines when a divergent beam of X-rays from a point source traverses a single crystal.

being in the position of Bragg reflection for the characteristic radiation causes reflection cones which give rise to curved reflection lines when intersecting the film. The intensity of the characteristic radiation is accordingly diminished in certain well-defined directions so that absorption (deficiency) lines are formed. The simple geometry is illustrated by Fig. 1, and the appearance of a divergent-beam diffraction pattern is shown in Fig. 2.

METHOD AND MATERIAL

In the present study the two lens point projection X-ray microscope constructed by Cosslett and Nixon (for references, see *3*) was used. The principle of the microscope is that two adjustable magnetic electron lenses are employed to throw an extremely reduced electron image of a pin-point cathode on the target. The target consists of an exchangeable thin metal foil, through which the divergent X-ray beam emerges into the atmosphere (Fig. 3). Under the experimental conditions used, the emitted X-rays gave an external beam with a divergence of 110°. This divergence was found to be satisfactory for most purposes, but by a slight elongation of the target holder and the introduction of a new pole-piece, the divergence of the beam could be increased to almost 180°. The size of the focal spot, which was in the order of 1 μ, could easily be obtained and was controlled visually or photographically from the shadow image of a silver grid (1500-mesh/in., 3 μ bars) at a direct magnification of about 300 times. The accelerating voltage most often used was 17 kV, and the target was a 3 μ thick copper foil. The Ni filters used (21 or 42 μ thick) were placed in direct contact with the target in order to prevent sharp image formation of inhomogeneities in the foil.

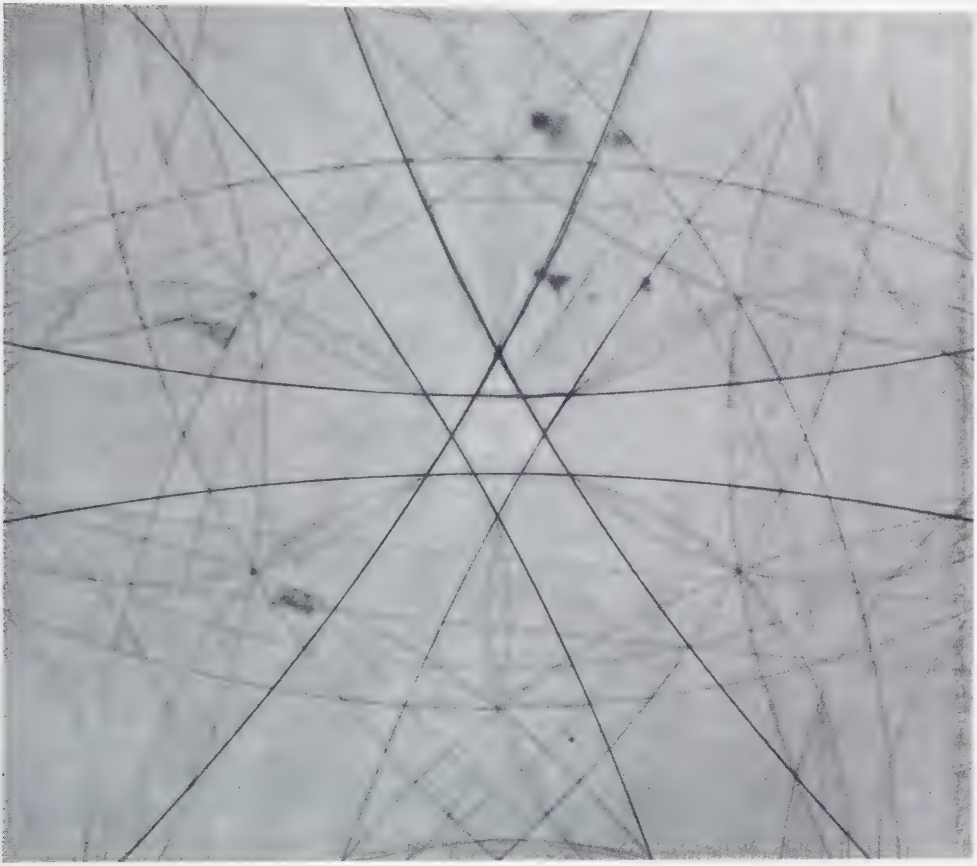

FIG. 2. Negative print of the central part of a divergent-beam diffraction pattern from a spinel twin diamond. Octahedral face parallel to target surface. Thickness of specimen 1.2 mm. Cu target, 21 μ Ni filter, 17 kV and 15 μA. Exposure time 30 min. Black dots are caused by minute inclusions in the specimen. Note the splitting of some lines in the upper part of the picture due to distortions in the crystal. $\times 13.5$.

In order to record the whole (110°) divergent beam, and at the same time to obtain photographs of highest resolution, an extremely fine-grained plate (Kodak Maximum Resolution), capable of resolving at least 1000 lines per mm, was placed 8.7 mm from the focus. The slow speed of this fine-grained film, as compared with ordinary X-ray emulsions or lantern slides, was compensated by the short focus-to-film distance. The exposure times were then usually in the order of 0.5 to 1.5 hours, but when using double coated X-ray film (Ilford Industrial G) and a focus-to-film

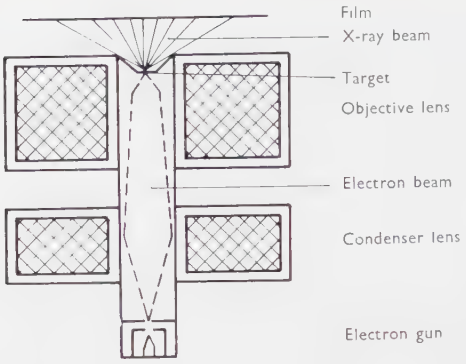

FIG. 3. Principal parts of the two lens projection X-ray microscope.

distance of 50 mm, diffraction patterns of relatively good quality were obtained with exposure times even as short as 10 seconds. In order to prevent fogging of the film caused by the strong fluorescence in visible light of some of the crystals, the film was wrapped in a 9 μ Al foil.

A number of readily obtainable single crystals of different symmetry and varying degree of perfection such as gypsum, apatite, calcite, rock-salt, mica and diamond were investigated. In the more highly absorbing crystals some care had to be taken with regard to the smoothness of the surfaces traversed by the beam, as otherwise an enlarged X-ray image was obtained of the irregularities. The crystals were mounted very close (<0.2 mm) to the target foil.

THE RESOLUTION OF THE DIFFRACTION PATTERNS

Whereas the widths of the absorption lines depend mainly upon the texture of the crystals and the size of the focal spot, the sharpness of the reflection lines, on the other hand, also depends upon the thickness of the specimen (see Fig. 1). Therefore the reflection lines usually form quite broad bands, but incidentally they might appear almost as sharp as the absorption lines. Under favourable conditions, i.e., when perfect or nearly perfect crystals are used, and the size of the focus is small, the widths of the absorption lines amount to only a few minutes of arc. In order to record these lines with the highest possible resolution, when using ordinary photographic material, earlier investigators had to keep relatively long focus-to-film distances (up to 100 cm), with the result that only parts of the entire diffraction

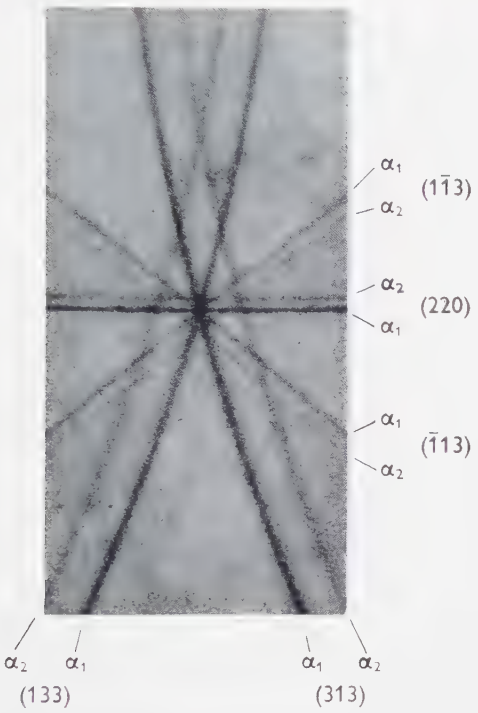

FIG. 4. Detail of a divergent-beam photograph of a 1.7 mm thick diamond showing the good resolution of the Cu $K\alpha_1$ and α_2 absorption lines. × 84.

pattern could be recorded. In the present investigation, this difficulty was solved by using extremely fine-grained emulsions at a very short focus-to-film distance. The small size of the focal spot of the projection X-ray microscope completely eliminated the geometrical blurring, and the high resolution obtained is illustrated by Fig. 4. Photometer measurements of the Cu $K\alpha_1$ and α_2 absorption lines of the (331) planes of diamond gave a half maximum width of $18\% \pm 2\%$ of the α_1–α_2 separation. This is very close to the natural spectral width (15%) given by Compton and Allison (*2*) and might be compared with the results reported by Kossel and Voges (*5*) and van Bergen (*1*), who used a quite different and much less versatile divergent-beam technique with the crystal itself serving as target inside the X-ray tube. With the resolution used in the present investigation it should be possible, according to the method given by Kossel (*4*) and Lonsdale (*6*), to determine the unit cell dimensions with a precision about 1 : 100,000.

THE CONTRAST OF THE ABSORPTION LINES

The contrast of the absorption lines against the uniform background depends upon the spectral distribution of the radiation and also upon the thickness and texture of the crystals.

Composition of radiation

Earlier works on divergent-beam diffraction with the transmission technique have been carried out with unfiltered X-rays containing an undefined amount of continuous radiation. It is evident, however, that a considerable gain in the contrast of the diffraction patterns should be possible by using monochromatic X-rays. The contrast of an absorption line can be expressed as $(I-I_{(hkl)})/I$, where I is the intensity of the background, and $I_{(hkl)}$ is the intensity of the absorption line. Since each absorption line is caused by the reduction of the intensity of a specific wave length at a given Bragg angle, all other wave lengths present tend to decrease the contrast. In this respect the harder portion of the continuous spectrum is especially harmful. When using Ni-filtered Cu radiation at 17 kV, a very good monochromatization could be obtained, for not only was the Cu $K\beta$ radiation negligible but this also applied to wave lengths shorter than 1.49 Å. The softer part of the continuous spectrum was of course less reduced, but being more readily adsorbed in the specimen as compared with the Cu $K\alpha$, it was of minor importance.

The monochromatization of the Cu radiation allowed good divergent-beam photographs to be taken, even of rather highly absorbing crystals such as apatite and calcite, which yielded poor patterns when using unfiltered radiation.

Thickness of specimen

The thickness of the specimen plays an important role with regard to the contrast of the diffraction patterns. It is clear that the specimen must be thick enough to build up an absorption line of sufficient negative intensity, but not so thick that the characteristic radiation is completely absorbed in the specimen. Lonsdale (6) calculated the optimum thickness for diamond and rock-salt, but as the values given by her refer to unfiltered radiation of unknown wave length distribution, her results seem to be very uncertain. Assuming that the reduction in the intensity of the characteristic radiation at the Bragg reflection angles follows the usual law of absorption (which can be presumed only for perfectly imperfect crystals), the contrast of a $K\alpha_1$ absorption line for pure $K\alpha$ radiation can be expressed as $\frac{2}{3}(1-e^{-\mu' t}/e^{-\mu t})$. In this expression t is the effective thickness of the crystal and μ' and μ are respectively the linear absorption coefficients of the $K\alpha$ radiation at and close to a given Bragg

angle. When using pure Cu $K\alpha$ radiation there will be a continuous increase in contrast with increasing thickness of the specimen, but if μ' is large compared to μ, the thickness will be of minor importance as can easily be seen when rewriting the ratio as $e^{-t(\mu'-\mu)}$. In practice, however, it is not possible to obtain absolutely pure Cu $K\alpha$ radiation nor is it convenient to use specimens much thicker than $1/\mu$ because of the resulting increase in the exposure time.

Crystal texture

The crystal texture is the most important factor, when considering the contrast of the absorption lines. As already mentioned, the expression given for pure $K\alpha$ radiation is only valid when ignoring multiple reflection. Since most crystals are not ideally mosaic it is clear that both primary and secondary extinction will modify the above equation. As these quantities are difficult to express in precise terms, only some general comments will be given. Lonsdale (*6*) found that perfect crystals gave very weak or no absorption lines at all, whereas partly imperfect crystals gave good diffraction patterns. On the whole this seems to be true, but by monochromatization of the radiation good patterns with extremely sharp absorption lines could be obtained even from perfect crystals. Because of the high primary extinction in such crystals, all reflection lines are absent. Since the Bragg reflections in perfect crystals only take place from a limited number of planes nearest the X-ray source, the optimum thickness for such specimens should be very much lower than that for ideally mosaic crystals. The best divergent-beam diffraction patterns showing the highest contrast were recorded from partly imperfect crystals. Undoubtedly, the secondary extinction here plays a predominant role, but it does not seem possible to get a direct measure of it from divergent-beam patterns. Nevertheless, valuable information about crystal texture can be obtained. Distortions localized to certain areas of the crystal are revealed by the broadening or splitting up of corresponding absorption lines, and the degree of crystal perfection can be roughly estimated from the intensity of the reflection and absorption lines.

CONCLUDING REMARKS

The characteristics of the projection X-ray microscope make it a suitable instrument for divergent-beam diffraction. The simplicity in changing the target material makes it possible to record good diffraction patterns of single crystals composed of heavier elements than those hitherto investigated. Since investigation on crystal orientation and crystal texture can be made in a rapid and accurate way, this instrument will certainly prove to be as useful for diffraction work as for pure microradiography.

ACKNOWLEDGEMENTS

We are greatly indebted to Mr. T. Ando, A.B. Industridiamanter, Stockholm, for his kindness in lending a representative collection of industrial diamonds, as well as to Mr. H. Bohlin, who offered us suitable diamonds of gem quality for this investigation.

REFERENCES

1. BERGEN, H. VAN, *Ann. Physik* **33**, 737 (1938).
2. COMPTON, A. H. and ALLISON, S. K., X-Rays in Theory and Experiment. D. van Nostrand, New York, 1957.
3. COSSLETT, W. E., ENGSTRÖM, A. and PATTEE, H. H. (Eds.), X-Ray Microscopy and Microradiography. Academic Press Inc., New York, 1958.
4. KOSSEL, W., *Ann. Physik* **26**, 533 (1936).
5. KOSSEL, W. and VOGES, H., *Ann. Physik* **23**, 677 (1935).
6. LONSDALE, K., *Phil. Trans. Roy. Soc. London Ser. A* **240**, 219 (1947).

CONTENTS

Printed in Sweden

Uppsala 1958. Almqvist & Wiksells Boktryckeri AB 583564